THERMOPHYSICAL CHARACTERISTICS OF MANTLED TERRESTRIAL VOLCANIC SURFACES: INFRARED ANALOGS TO ARSIA MONS.

by

Mark A. Price

Bachelor of Science, University of Mount Union, 2011

Submitted to the Graduate Faculty of the

Kenneth P. Dietrich School of Arts and Sciences in partial fulfillment

of the requirements for the degree of

Master of Science

University of Pittsburgh

2013

UNIVERSITY OF PITTSBURGH

KENNETH P. DIETRICH SCHOOL OF ARTS AND SCIENCES

This thesis was presented

by

Mark A. Price

It was defended on

May 13, 2013

and approved by

William Harbert, Professor, University of Pittsburgh

Mark Abbott, Professor, University of Pittsburgh

Thesis Director: Michael Ramsey, Professor, University of Pittsburgh

THERMOPHYSICAL CHARACTERISTICS OF MANTLED TERRESTRIAL VOLCANIC SURFACES: INFRARED ANALOGS TO ARSIA MONS.

Mark A. Price, M.S.

University of Pittsburgh, 2013

Sediment/regolith history and mantling of underlying bedrock are important processes to understand for Mars science. The movement of dust over time significantly modifies and covers many bedrock surfaces on Mars. A reliable remote sensing tool for martian geology is thermal inertia, which allows for a detailed analysis of surface properties based on their response to heating and cooling. The future goal of this project is to use thermal inertia to identify eolian- mantled lava flows on Mars and derive a process for separating the spectral signature of the mantling from that of the lava. However, this method must be tested on a terrestrial proxy in order to gauge its effectiveness using ground and laboratory validation. An example of mantled volcanic terrain on Earth is the Mono Crater chain in California, which will serve as an analog for this work. Unfortunately, thermal inertia cannot be calculated from satellite-based imaging, so a proxy called apparent thermal inertia (ATI) was used. Two temporally similar day/night images of the Mono Craters were collected from the Advanced Spaceborne Thermal Emission and Reflection Radiometer (ASTER) instrument in the thermal infrared (TIR) and visible near- infrared (VNIR). These data were used to create the ATI image. After comparing the ATI result to high-resolution aerial photos it was discovered that ATI appeared to correlate with block size and mantling material. Fieldwork was conducted in July of 2012 on and around North Coulee dome at the Mono Craters. Results The ATI result was found to be reliable, however shadowing on a sub- to super-pixel level was found to artificially increase ATI values in those regions.

Future studies should mitigate this by incorporating a digital elevation (DEM) model and possibly radar backscatter into the ATI analysis to better determine block size. The success of the proxy study on Earth provides a foundation from which future work can be conducted on the Arsia Mons and Syria Planum mantled lava flows. Space-based thermal inertia investigations of these sites would provide insight to the history and eolian patterns of both regions and a greater understanding of the volcanic history and composition in these regions.

TABLE OF CONTENTS

LIST OF TABLES

LIST OF FIGURES

PREFACE

I would like to thank Mike Ramsey and David Crown for input and guidance into the project. I am grateful for the contributions of Bill Harbert and Mark Abbott and for their presence on my thesis committee. I would also like to thank Rachel, Anna, Topher, Daniel, Janine, Sarah and Charlie for their contributions. Finally I will thank the Beach Boys and their masterpiece, *Pet Sounds*, for giving this thesis a soundtrack.

1.0 INTRODUCTION

Sediment/regolith history, mobility, and its mantling of underlying bedrock are important processes in order to understand Mars surface processes. The movement of sand/dust over time significantly modifies and covers many bedrock surfaces on Mars (Malin and Edgett, 2001). These deposits may be derived locally and retain the chemical and spectral signatures of the underlying rocks (Edgett and Lancaster, 1993; Fenton and Bandfield, 2003). However, in many cases this material is globally homogenized and obscures the surface below thereby hindering accurate identification from orbit (Johnson et al. 2002; Ruff and Christensen, 2002).

Although not as pervasive on Earth, surface mantling can arise from a variety of processes such as explosive volcanic eruptions and desertification. These locations can serve as analogs for testing both geologic and image processing hypotheses regarding martian eolian processes. An example of eolian mantled terrain on Earth are the Mono Craters and Domes, an arcuate chain of silicic lava flows in California that formed over the past 10,000 years. Newer domes in the chain commonly cover older domes with substantial pyroclastic airfall deposits. The region contains an assortment of heavily mantled pumice surfaces and unmantled obsidian volcanic flows, commonly within meters of each other. The volcanic terrain present in this area provides a fitting analog to mantled lava flows in the Arsia Mons and Syria Planum regions of Mars. Because space-based infrared spectroscopy also has the potential of approximating the thickness of mantling deposits overlying bedrock layers (e.g. Hardgrove et al., 2009; Scheidt et

al., 2010, 2011), the ability to ground-truth satellite data at the Mono Craters provides an opportunity to test the validity and accuracy of these methods.

Perfecting the identification and differentiation of mantled and rocky surfaces from space is paramount, as ground-based validation clearly cannot be conducted for most surfaces on Mars. Using a satellite imaging-derived substitute for thermal inertia, known as apparent thermal inertia or ATI, it is hypothesized that particle size and mantling thickness can be approximated from space-based imagery (Fenton and Bandfield, 2003; Hardgrove et al., 2009; Ramsey and Crown, 2010; Ramsey et al. 2012). The ultimate goal, however, would be to decouple the thermal infrared (TIR) spectral signature of the mantling material in order to map the compositional diversity of the underlying lava flows (Ramsey and Crown, 2010; Ramsey et al., 2012; Price et al., 2013). The Earth-based analog at the Mono Craters provides a great opportunity for field validation of study sites. The volcanic debris overlaying the Mono Craters provides a similar mantling environment to Arsia Mons and Syria Planum (Greeley, 1982; Ruff and Christensen, 2002; Plescia, 2004; Lang et al., 2009). It is imperative that precise data interpretation methods be established at proxy sites before application to martian terrain, considering the lack of ground-based study.

Presented here are the outcomes of field, laboratory, and satellite imaging investigations of the mantled deposits covering the Mono Craters Volcanic Chain, specifically the North Coulee dome/flow. A combination of TIR and visible-near infrared (VNIR) image processing, laboratory spectroscopy, and field geomorphic analysis were used in an attempt to authenticate this image modeling approach.

1.1 ASTER AND THERMAL INERTIA

The Advanced Spaceborne Thermal Emission and Reflection Radiometer (ASTER) instrument is one of five scientific instruments on the Terra satellite (http://terra.nasa.gov). Besides ASTER, other remote sensing instruments on Terra include the Clouds and Earth's Radiant Energy System (CERES), Measurements of Pollution in the Troposphere (MOPITT), Moderate Resolution Imaging Spectroradiometer (MODIS), and the Multi-angle Imaging Spectroradiometer (MISR). Terra was the flagship of the Earth Observing System (EOS) when it was launched. EOS is a series of spacecraft instruments intended to expand synergistic observations of the Earth's climate, solid earth, hydrological and biological cycles as well as the energy fluxes that impact each of them. Terra was launched into sun-synchronous Earth orbit on December 18, 1999, and started sending data back to earth in February 2000. Additional details on the Terra satellite can be found in Table 1.

Terra Specifications	
Launch date:	December, 1999
Orbit:	705 km altitude, sun-synchronous, so that at any given latitude it crosses directly overhead at the same time each day.
Orbit inclination:	98.3 degrees from the Equator
Orbit period:	98.88 minutes
Equator crossing:	10.30 a.m. (north to south)
Ground track repeat cycle:	16 days, i.e. every 16 days (or 233 orbits) the pattern of orbits repeats itself
Builder:	Lockheed Martin

Table 1: Specifications provided by the NASA Jet Propulsion Laboratory of the Terra satellite containing the ASTER instrument.

ASTER is a research instrument developed by Japan and the United States to improve understanding of the local- and regional-scale processes occurring on or near the Earth's surface and lower atmosphere, including surface-atmosphere interaction (Yamaguchi et al., 1998; Tanooka et al., 2003). The extensive spectral coverage and high spatial resolution allow ASTER to distinguish between varieties of surface materials and to better understand compositional mixing because of the smaller pixel size (Yamaguchi et al., 1998). ASTER has three spectral bands in the visible near-infrared (VNIR), six bands in the shortwave infrared (SWIR), and five bands in the thermal infrared (TIR) regions (Figure 1), with 15-, 30-, and 90-m ground resolution, respectively (Table 2) (Yamaguchi et al., 1998). Unfortunately, the SWIR detectors failed in April 2008 because of a non-functioning cryocooling system that produced anomalously high SWIR detector temperatures (http://asterweb.jpl.nasa.gov). SWIR images acquired since this date are saturated and therefore are no longer useable.

Subsystem: VNIR					
Band No.	Spectral Range (μm)	Radiometric Resolution	Absolute Accuracy (σ)	Spatial Resolution	Signal Quantization Levels
1	0.52–0.60	NEΔρ 0.5%	≤±4%	15 m	8 bits
2	0.63–0.69	NEΔρ 0.5%	≤±4%	15 m	8 bits
3N	0.78–0.86	NEΔρ 0.5%	≤±4%	15 m	8 bits
3B	0.78–0.86	NEΔρ 0.5%	≤±4%	15 m	8 bits
Subsystem: SWIR					
Band No.	Spectral Range (μm)	Radiometric Resolution	Absolute Accuracy (σ)	Spatial Resolution	Signal Quantization Levels
4	1.600–1.700	NEΔρ≤ 0.5%	≤±4%	30 m	8 bits
5	2.145–2.185	NEΔρ≤ 1.3%	≤±4%	30 m	8 bits
6	2.185–2.225	NEΔρ≤ 1.3%	≤±4%	30 m	8 bits
7	2.235–2.285	NEΔρ≤ 1.3%	≤±4%	30 m	8 bits
8	2.295–2.365	NEΔρ≤ 1.0%	≤±4%	30 m	8 bits
9	2.360–2.430	NEΔρ≤ 1.3%	≤±4%	30 m	8 bits
Subsystem: TIR					
Band No.	Spectral Range (μm)	Radiometric Resolution	Absolute Accuracy (σ)	Spatial Resolution	Signal Quantization Levels
10	8.125–8.475	NEΔT≤ 0.3%	--	90 m	12 bits
11	8.475–8.825	NEΔT≤ 0.3%	≤3K (200–240K)	90 m	12 bits
12	8.925–9.275	NEΔT≤ 0.3%	≤2K (240–270K)	90 m	12 bits
13	10.25–10.95	NEΔT≤ 0.3%	≤1K (270–340)	90 m	12 bits
14	10.95–11.65	NEΔT≤ 0.3%	≤2K (340–370)	90 m	12 bits

ASTER System Baseline Performance Requirements

Swath Width	60 Kms
Total Cross-Track Coverage	±116 to ±318 Kms
Stereo Base-to-Height Ratio	0.6 (along-track)
Modulation Transfer Frequency	0.25 (cross-track
	0.20 (along-track)
Band-to-Band Registration	0.2 pixels (intra-telescope)
	0.3 pixels (inter-telescope)
Duty Cycle	8% (VNIR & SWIR)
	16% (TIR)
Peak Data Rate	89.2 Mbps
Mass	406 Kgs
Peak Power	726 W

Table 2: ASTER baseline performance requirements, adapted from Yamaguchi et al. (1998).

The three ASTER VNIR bands have wavelengths similar to those of the Landsat Thematic Mapper (TM) and the Optical Sensor (OPS) of the Japanese Earth Resources Satellite (JERS-1). However, unlike Landsat TM, ASTER VNIR does not have a band in the visible blue region (0.4 – 0.5 microns). The VNIR bands are regularly used to analyze vegetation and iron-oxide minerals in surface soils and rocks (Hellman and Ramsey, 2004; Rowan et al., 2005, 2006) as

well as to produce digital elevation models (DEMs). The ASTER TIR subsystem also differs from past land imaging sensors such as Landsat in that it has five bands in the thermal infrared region. Emissivity spectra derived from the five TIR bands are used to estimate silica content (Ninomiya, 2002, 2003; Watanabe and Matsuo, 2003), which is important in characterizing silicate rocks; the most abundant rock type on the Earth's surface. According to Scheidt et al. (2011) ASTER has a substantial advantage in Earth-based remote sensing because of its relatively high spatial resolution (90m), enhanced multispectral capabilities is the thermal infrared, and global coverage.

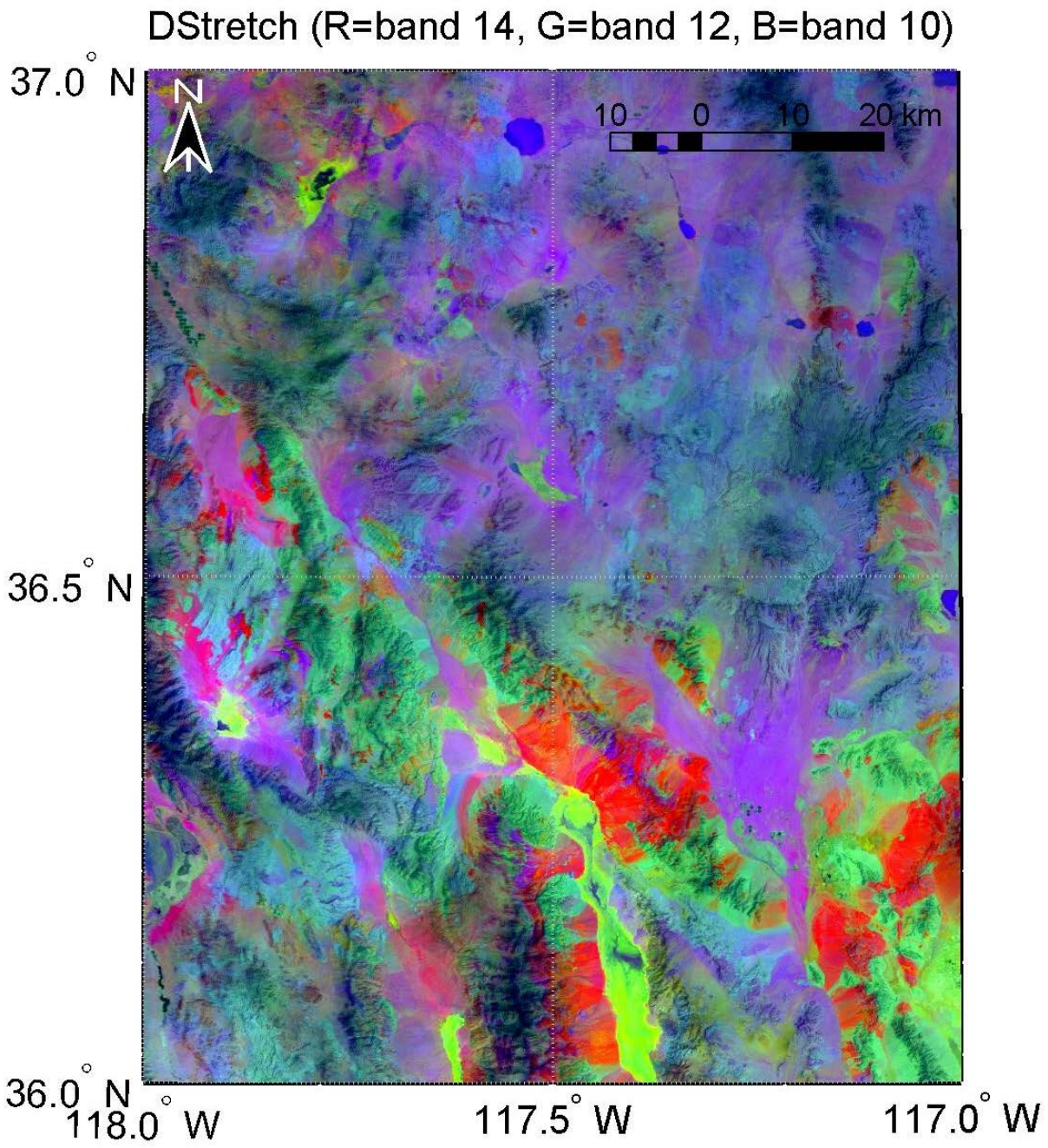

Figure 1: Decorrelation image constructed from an ASTER mosaic of TIR bands 14, 12 and 10 displayed in RGB, respectively for the area around Death Valley California. Quartz rich rocks are shown in red and magenta, quartz poor rocks are displayed in blue and purple and carbonate rocks are shown in green (from: http://emissivity.jpl.nasa.gov/examples/jpl-images).

This project used ASTER data to identify thermal inertia differences in surface features in order to identify zones of mantling deposits and bedrock outcrops. Thermal inertia measures the thermal response of a substance to a time-varying surface power input (Price, 1977). A sandy beach is an example of low thermal inertia surface, as it will gain and lose temperature very quickly over a diurnal period. Larger rocks and water bodies, however, take much longer to gain or lose temperature. These are examples of high thermal inertia. Thermal inertia differences are useful in identifying different surfaces within a remote sensing image. For example, mixing or layering of different thermal inertia units can be detected and used to derive particle/block sizes and layer thicknesses (Edgett and Malin, 2002; Bandfield and Feldman, 2008). However, thermal inertia studies on Earth can be problematic because of the planet's thick, heterogeneous atmosphere that absorbs and scatters energy as well complicating the transfer of radiant energy between the grains of a particulate surface. This is especially a problem for satellite imaging, as emitted energy must be corrected for the effects of the atmosphere using modeling approaches. But even with a perfect atmospheric correction, thermal inertia modeling remains a complex problem (Nasipuri et al., 2006; Sabol et al., 2006). Airborne data collection can improve the results by reducing the atmospheric pathlength, but surface-atmospheric interaction such as condensation and precipitation can still distort thermal inertia results. Thermal inertia investigations on Earth also have to take into account vegetation cover and the local climate. Extensive vegetation cover can render geologic thermal inertia useless, as the thermal inertia of the vegetation cover will mask results from local geology. Local climate is also an important factor in thermal inertia, as diurnal temperature values are sensitive to atmospheric humidity and precipitation (Van de Griend et al., 1985; Rosema and Fiselier, 1990; Cai et al., 2007;

Matsushima et al., 2012). Despite these factors thermal inertia has been used on Earth extensively (Van de Griend e. al., 1985; Rosema and Fiselier, 1990; Cai et al., 2007; Scheidt et al., 2010; Matsushima et al., 2012). Most of these thermal inertia studies thus far have focused on mapping moisture content of soils and geologic identification. Apparent Thermal Inertia studies have also been conducted on Earth with varying degrees of success. Cracknell and Xue (1996) used the space-based Advanced Very High Resolution Radiometer (AVHRR) sensor to create accurate ATI images after consulting local weather data. A study by Sobrino and El Kharraz (1999a) expands on that work by successfully applying a derived thermal inertia proxy to AVHRR images of a region of Niger. Additional thermal inertia proxy maps were created on the Iberian Peninsula and Morocco (Sobrino and El Kharraz, 1999b).

In contrast, thermal inertia studies are commonplace on Mars because of its thin, simple atmosphere and lack of weather. Examples of thermal inertia research conducted on Mars can be found in various works. The work of Kieffer et al. (1977) utilized thermal inertia and albedo to differentiate between two different types of martian surface material. Palluconi and Kieffer (1981) used data from the two Viking orbiters to create a thermal inertia map between the Martian latitudes of 60° North and South. Mellon et al. (2000) compared thermal inertia mapping to thermal emission spectrometer (TES) observations of the Martian surface. This thermal inertia study was used to determine particle size, rock abundance, and exposures of bedrock to determine small-scale variability on the planet's surface. The work of Putzig et al. (2005, 2007) also focused on using thermal inertia to explore the heterogeneity of the Martian surface, especially the polar regions.

1.2 GEOLOGIC HISTORY

1.2.1 Bishop Tuff

Volcanism in east-central California during the last 5 million years is associated with the Eastern California Shear Zone (ECSZ), a zone of active deformation along the western border of the Basin and Range Province (Hill, 2006). The tectonic and magmatic processes within the ECSZ and its extension to the north along the Walker Lane (WL) in western Nevada reflect the collective effect of dextral slip along the San Andreas Fault transform boundary (Hill, 2006). This boundary lies between the Pacific Plate and North American plates and is the westward extension of the crust across the Basin and Range Province (Hill, 2006). Dispersed dextral slip across this NNW-striking corridor accommodates between 15 to 25% of Pacific–North American plate motion (Hill, 2006; Dixon et al. 2000). Volcanism within this area is believed to be the result of an upwelling of magma into the crust from the asthenosphere; the result of crustal thinning and stretching from the shear zone (Hill, 2006).

The Mono and Inyo Craters, 25–30 km north of Mammoth Mountain (Figure 2), are some of the most recent activity in the Long Valley Caldera region (Hildreth, 2004). The current Long Valley Caldera formed around 0.7Ma during the eruption of the Bishop Tuff, a voluminous rhyolite ash flow sheet (Dalrymple et al. 1965; Bailey et al., 1976). Shortly before the caldera-forming eruption, the mantle-driven focus of crustal melting shifted ~20 km westward, vacating its established position under Glass Mountain and energizing instead the central Long Valley

system (Hildreth, 2004). From now-buried caldera vents the ash flow inundated 1,500 square kilometers of the surrounding countryside, reaching as far as the southwestern Mono Basin (Bailey, 1989b; Bailey et al., 1976). It is believed that the deposits in the Mono Basin are as thick as 200 meters (Bailey, 1989b). The total volume of Bishop ash flows is approximately 500 km^3, two-thirds of which accumulated within the subsiding caldera (Bailey et al., 1976). Exposures in the Owens River Gorge show evidence of multiple cooling units (Sheridan, 1967), suggesting the ash was deposited in two phases of eruption (Bailey, 1989b). Plinian ash clouds from this eruption have been identified as far east as Kansas and Nebraska (Bailey, 1989b). The Bishop Tuff is crystal-rich, porphyritic rhyolite and pumice that contains 5 to 25 percent phenocrysts of quartz, sanidine, plagioclase, augite, biotites, hypersthene, Fe-Ti oxides, and accessory minerals (Gilbert, 1938; Sheridan, 1965; Bailey et al. 1976; Bailey, 1989b). The tuff shows considerable variation in degree of welding and crystallization (Sheridan, 1965, 1970; Bailey, 1989b) depending on the location. The initial caldera-forming eruption was followed by later eruptions of Moat Rhyolites (Hildreth, 2004). These were deposited between 500 and 100 ka and are substantially less volume (Hildreth, 2004).

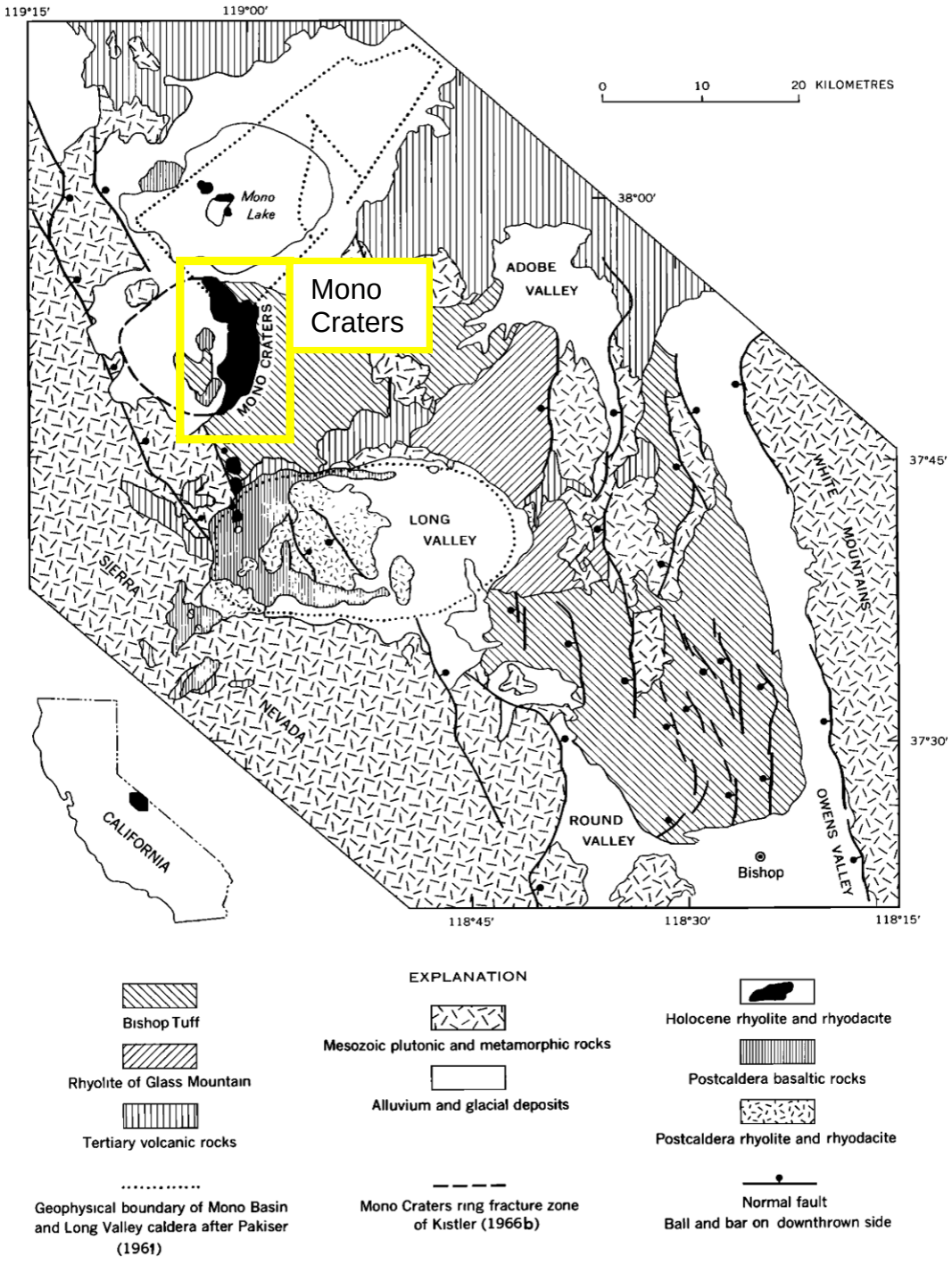

Figure 2: Index map and generalized geologic map of the Long Valley - Mono Basin area, adapted from Bailey et al. (1976). The Mono Craters are highlighted in the yellow box.

1.2.2 Long Valley Caldera

The Long Valley Caldera–Mono Craters volcanic field resides in a left-stepping offset in the eastern escarpment of the Sierra Nevada at the north end of the Owens Valley graben (Hill, 2006). The oval floor of the Long Valley Caldera ranges in elevation from 2,000 meters in the eastern portion, which is dominated by Lake Crowley and is covered mostly by grass and sage, to 2,600 meters in the western portion, which is hilly and forested (Bailey, 1989b). The volcanic field sits on large, east-dipping faults that form the western edge of the Basin and Range Province (Hill, 2006). The Caldera is an elliptical depression that formed 0.7 Ma during the eruption of the Bishop Tuff (Bailey et al. 1976). The eruption began as a Plinian outburst along or near the Hilton Creek fault in the south-central part of the soon-to-be-formed caldera (Hildreth and Mahood, 1986). The roof of the growing magma chamber, about 5 km deep at the time (Wallace et al., 1999), ultimately collapsed, releasing ~600 km^3 of gas-rich rhyolitic magma, compositionally and thermally zoned (Hildreth, 1979), in a continuous eruption about 6 days long (Wilson and Hildreth, 1997). The escaping magma allowed the chamber roof to subside 2–3 km, which created the Long Valley Caldera (Wilson and Hildreth, 1997). Subsequent eruptions have deposited smaller amounts of Moat Rhyolite and crystal-poor high-silica rhyolite in the caldera (Hildreth, 2004).

1.2.3 Mono-Inyo Craters

The Mono-Inyo Craters are an alignment of rhyolite vents in the north of the Long Valley Caldera that are about 610 m above the surrounding terrain to a maximum elevation of 2,800 m (Bailey, 1989b). This 17 km long arcuate ridge is one of the prominent physiological features in the caldera (Bailey, 1989b). The 11-km-long Inyo volcanic chain consists of 6 magmatic and more than 15 phreatic eruptive centers aligned along a north-trending fracture (Miller, 1985). About 0.8 km^3 of rhyolitic-rhyodacitic magma erupted along this chain in at least 3 eruptive episodes during the past several thousand years (Miller, 1985). The Mono Craters consist of approximately 28 domes and coulees, several-correlated explosion craters and ejecta rings, and an extensive apron of pumiceous fall, flow, and reworked deposits (Hildreth, 2004; Bailey, 1989b; Bursik and Sieh, 1989, 2012). The Mono-Inyo chain is theorized to be a united magmatic system considering the virtually contiguous Holocene rhyolite vents that make up the two chains (Hildreth, 2004).

The Mono Craters began formation northwest of the main Long Valley Caldera chain around 40ka and are still considered volcanically active (Hildreth, 2004; Bursik and Sieh, 2012). Single-crystal $^{40}Ar/^{39}Ar$ ages for sanidine from pre-Holocene rhyolitic ash layers intercalated with lacustrine silts of Mono Lake suggest that as many as 15 explosive eruptions took place before 20 ka (Chen et al., 1996; Kent et al., 2002; Hildreth, 2004). This indicates that most of the earliest Mono domes are buried and concealed by modern formations (Bursik and Sieh, 1989; Hildreth, 2004). Bursik and Sieh's 2012 paper states that only one exposed Mono Dome is older than 20 ka. This dome, just south of Crater Mountain (Dome 17, Figure 3), sits about where the original 40 ka eruption vents are believed to be (Bailey, 1989a). It is believed that only half of the Mono Craters' volume (8.5 km^3 of volcanic deposit) is currently visible at the surface

(Bursik and Sieh, 2012). The total volume of all of the volcanic deposits is estimated to be about 4 km^3, with the largest being ~ 0.5 km^3 each at North and South Coulee (Hildreth 2004).

Beginning in the Holocene the Mono system advanced single-file both north and south, producing dike-fed domes of crystal-poor high-silica rhyolite (Hildreth, 2004). Bursik and Sieh (1989) suggest that the "single-file" trend of the domes is the result of an extensional margin of a pull-apart basin between NNW-trending oblique-slip faults having a dextral component. Seismological studies by Achauer et al. (1986) suggest that the probable magmatic source is a subjacent north-south elongate chamber at a depth of 10 to 20 kilometers; there appears to be no evidence for a larger magma chamber deep within the crust (Bailey, 1989b). A volumetric eruption rate of about 0.2 km^3/ka in the early Holocene increased to about 0.8 km^3/ka during the last 3,000 years, a fourfold increase (Wood, 1983). This volumetric surge coincided with a switch from crystal-poor to virtually aphyric rhyolite (Wood, 1983). This aphyric rhyolite might have been responsible for the formation of the youngest Mono domes. The four southernmost Mono domes (around Punchbowl Crater) are younger than 5 ka, and South Coulee is part of the 1.3-ka South Mono eruptive episode (Bursik and Sieh, 1989; Hildreth, 2004). Radiocarbon dating of South Coulee reveals that at least part of the dome was formed approximately 1,300 years ago (Bailey, 1989a).

The most recent eruption at the Mono Craters dates approximately to the 14th century (Sieh and Bursik, 1986; Hill, 2002; Hildreth, 2004). Evidence for this event includes 0.2 km^3 of pyroclastic fall, flow, and surge deposits and 0.4 to 1 km^3 of lava domes and flows (Sieh and Bursik, 1986; Bailey, 1989a). These rhyolitic deposits originated from five aligned vents at the northwestern portion of the Mono chain (Sieh and Bursik, 1986). The eruptive event appears to have developed because of a rising rhyolite dike that broke the surface (Bailey, 1989a).

According to Bailey (1989a) the modern exposures at Northwestern Coulee, Panum Crater, Upper Dome, Crater Dome and North Coulee were directly formed during this eruption (Figure 3). Panum Crater in particular is thought to have produced the youngest pyroclastic material of the Mono Craters (Bailey 1989a). It is believed that the most recent eruption consisted of three phases (Seih and Bursik, 1986). Initial deposits were explosive Plinian to sub-Plinian events that formed thick deposits of airfall tephra on domes within a few kilometers from the vent (Seih and Bursik, 1986; Bailey, 1989a). The second phase was comprised predominantly of pyroclastic flows and surges, whereas the final phase extruded viscous, block-encrusted lava domes and flows (Seih and Bursik, 1986). This last event created the modern domes in the northwest of the Mono Chain (Bailey, 1989a) (Figure 3). The North Mono eruption is contemporaneous with the latest eruption of the Inyo volcanic chain, about 20 km to the south (Seih and Bursik, 1986). However, they state Inyo tephra blanket clearly overlies, and thus postdates, all North Mono tephra. However, the chronological proximity of these eruptive events indicates the likelihood of a causal relationship (Bursik et al., 2003).

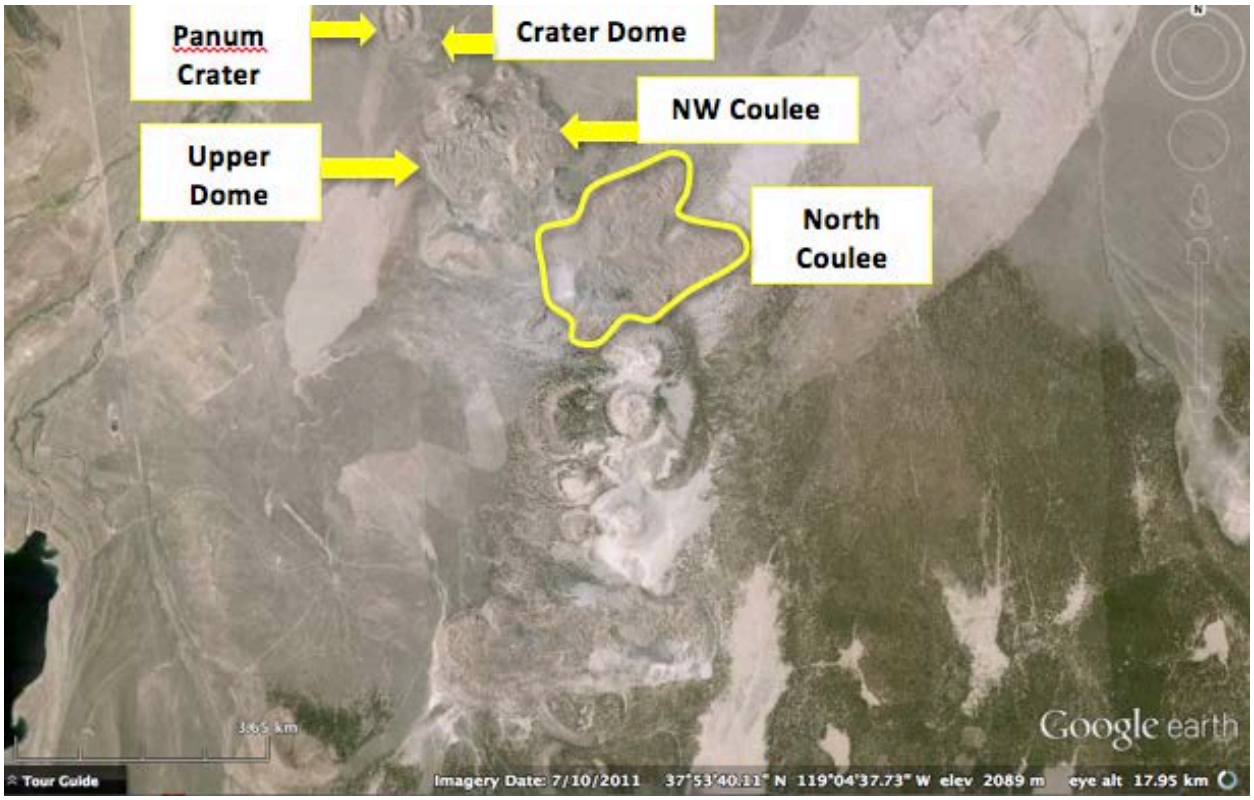

Figure 3: A high-resolution visible satellite image provided by Google Earth. This image was obtained on the same day as the ASTER day overpass (7/10/2011). Note the varying terrain. North Coulee is shown by the yellow outline.

North Coulee was the chosen field site for this study, and is the southernmost and largest of the most recent five aphyric rhyolite lava flows (Figure 4) (Russell, 1889; Seih and Bursik, 1986). The volume of the dome is 0.4 km^3, over half the total volume of the 14^{th} century eruption. North Coulee is a composite flow that originated from a northwest-trending fissure or alignment of vents. A solitary northwest-striking ridge, also composed of ashy to blocky gray glassy tephra, lies on the western edge of Northern Coulee (Seih and Bursik, 1986). Thick deposits of ashy to blocky tephra cover the dome (Figure 5). The site was specifically chosen because of the varied block size of tephra deposits and sporadic mantling on portions of the coulee. The mantling deposits have a similar composition as the dome/flows and likely came

from airfall deposition of pyroclastic material originating from the four other vents during the last eruptive phase.

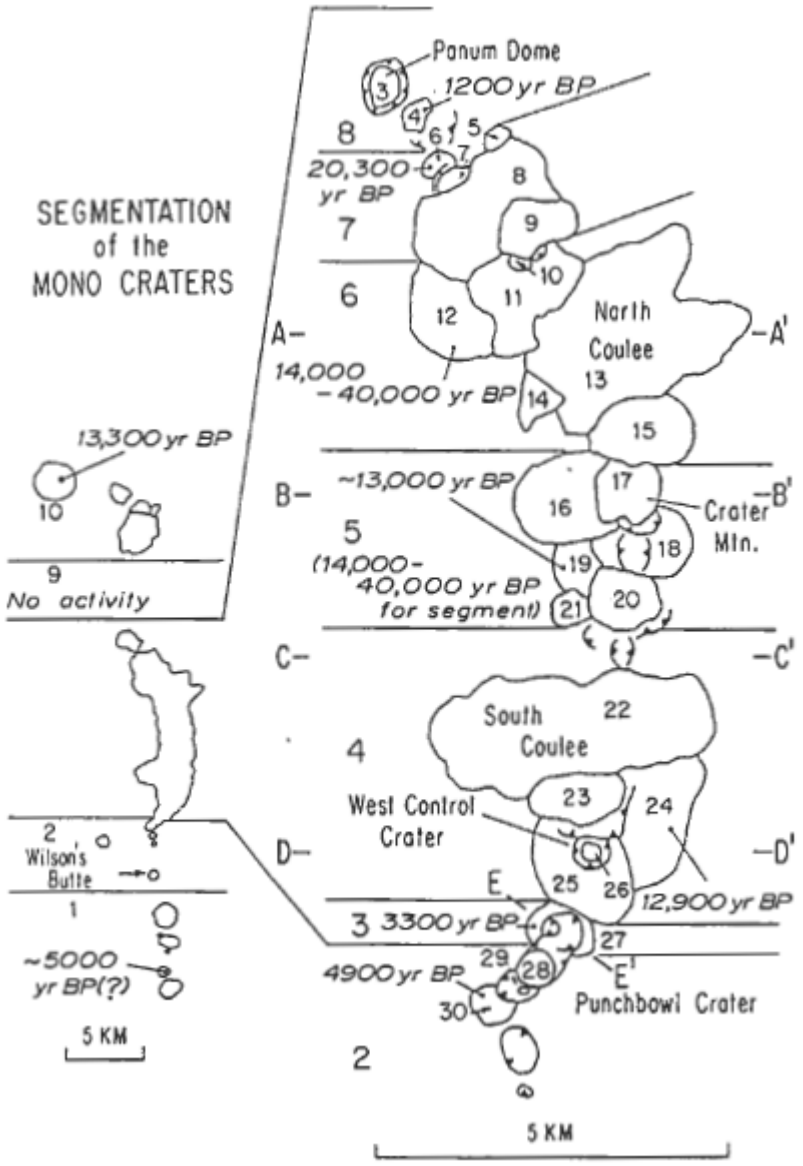

Figure 4: Map of the various coulees and domes of the Mono Craters from Bursik and Sieh (2012). Cross-sections are shown in Figure 5. Years date to the original formation of the dome, not the modern, exposed formation. The five sources of the 14th century eruption include Panum Dome (3), Crater Dome (4), Upper Dome (8), Northwest Coulee (11), and North Coulee (13). North Coulee was the focus of field research.

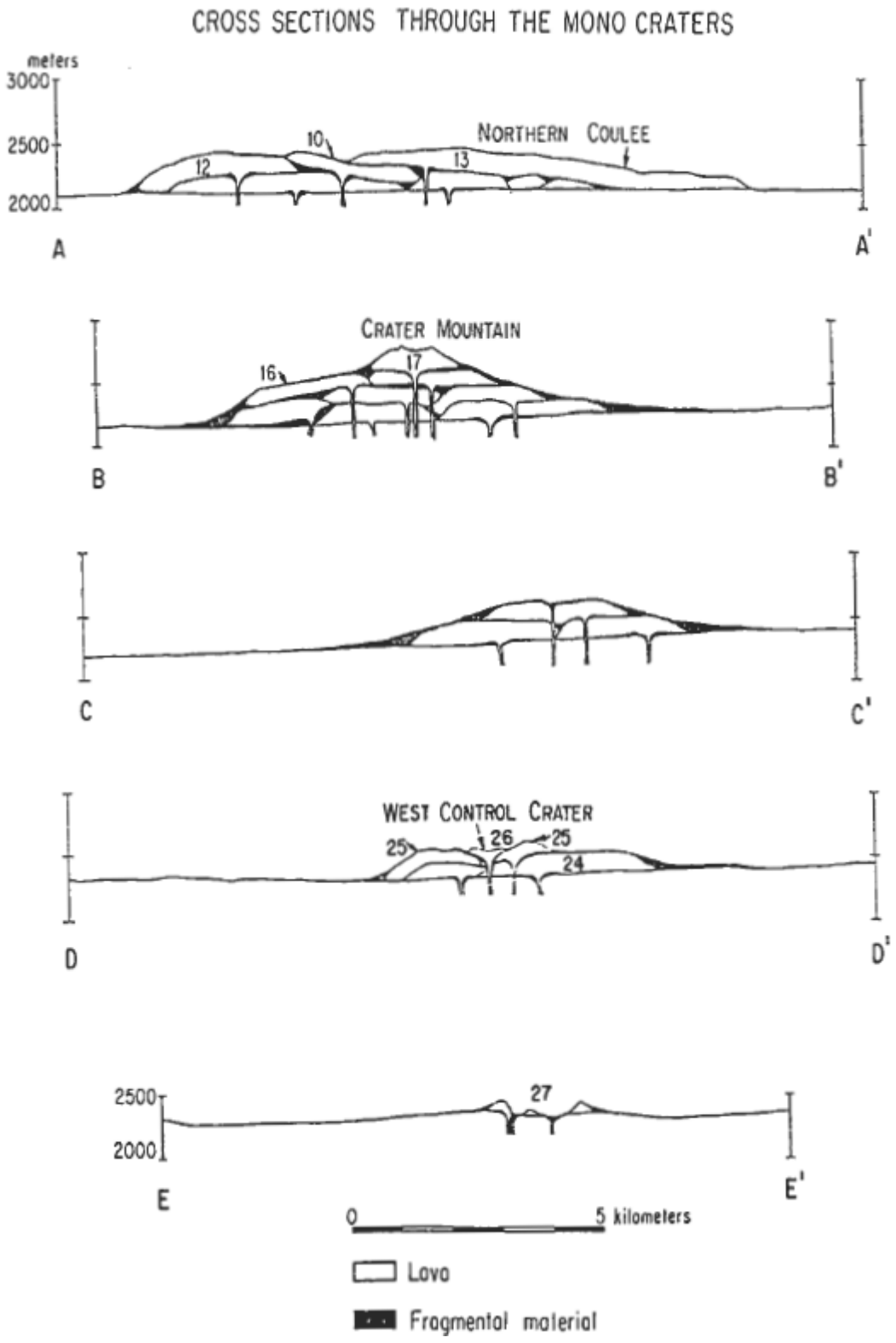

Figure 5: Cross-section through the Mono Craters from Bursik and Sieh (2012). Lines of section are shown in Figure 4.

Petrographic composition of the Mono Craters is typical for effusive deposits in the Mammoth area. All lavas but one at the Mono Craters are high-silica rhyolite (75.4–77 wt. % SiO_2) (Hildreth, 2004) (Figure 6). Major element (and most trace-element) contents are quite similar to those of Glass Mountain and the early Bishop Tuff (Hildreth, 2004). The lava at the Mono Craters is predominantly homogenous, but they show subtle differences in trace element and accessory mineral content. This insinuates that the deposits did not originate from a single chamber (Kelleher and Cameron, 1988; Bailey, 1989a). The principal compositional feature distinguishing the Mono Crater chain is a slightly higher FeO content (1.0–1.3 wt.%) (Hildreth, 2004). All but four of the 27 rhyolite lavas are dated from the Holocene; three are dated to about 13 ka and one at about 20 ka (Wood, 1983; Bursik and Sieh, 1989). The older extrusions (35 to 3 ka) tend to be moderately to lightly porphyritic, where the younger deposits are virtually aphyric (Bailey, 1989a). The appearance of aphyric deposits coincides chronologically with an increase in volumetric eruption rate (Wood, 1977; Bailey, 1989a).

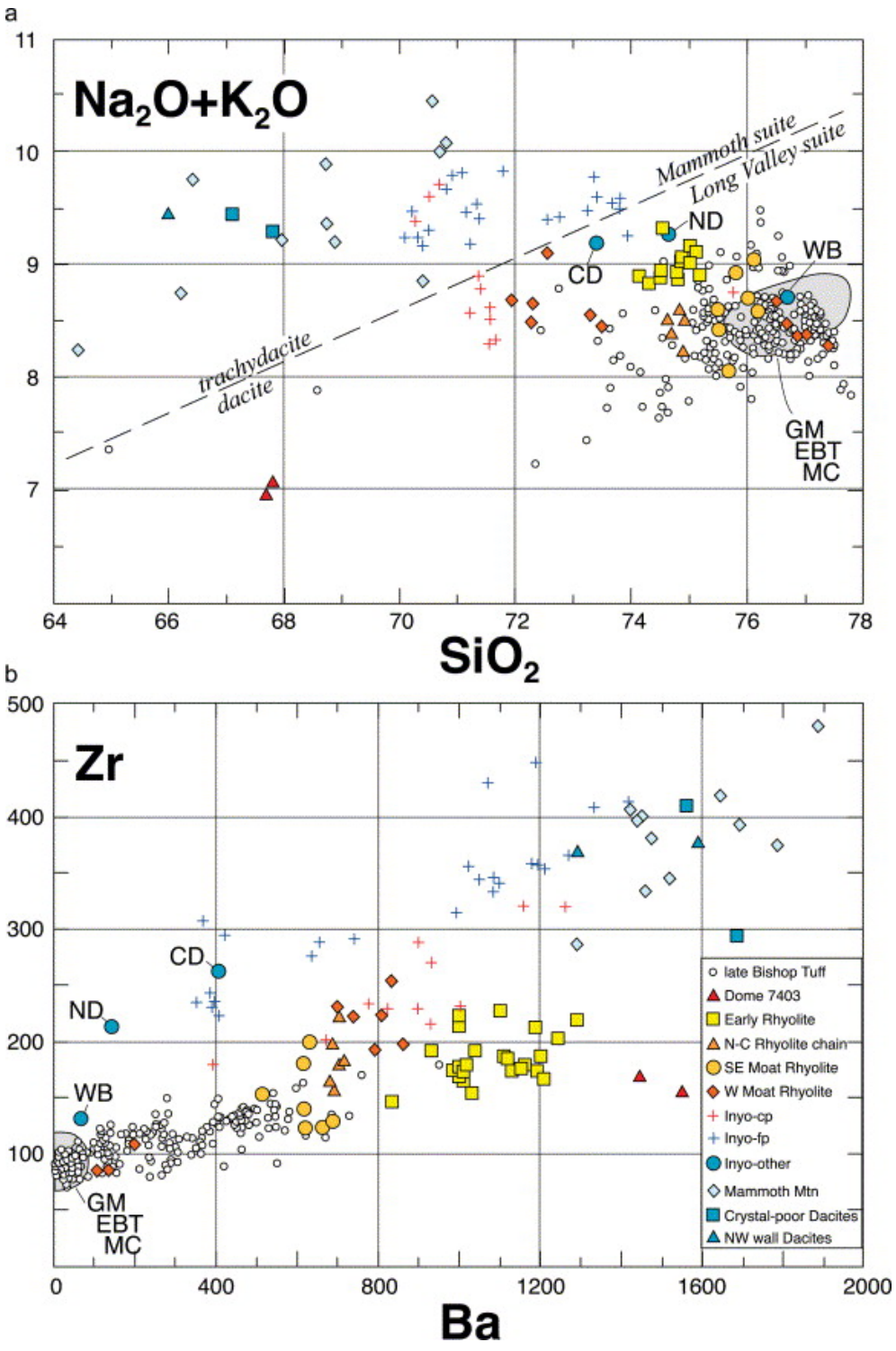

Figure 6: Composition of the Mono Craters from Hildreth, (2004).

2.0 METHODS

Thermal inertia (P) is a physical quantity describing the resistance of a material to change in temperature and is defined as $P=\sqrt{K\rho c}$, where K is the thermal conductivity, ρ is the density and c is the specific heat. Unfortunately, these values cannot be calculated directly via satellite measurements and must be obtained via other means. Apparent thermal inertia (ATI) is an approximation of thermal inertia using units that are measureable with satellite data. It is defined as $ATI=(1-a)/(\Delta T)$, with a representing the broadband VNIR/SWIR albedo and ΔT representing the temperature difference between a day and night pair of coregistered TIR images. Therefore, ATI is a relative measure of the reflected solar albedo to the difference in emitted brightness temperature over the diurnal cycle (Figure 7) (Price, 1977, 1985; Kahle, 1987; Scheidt et al., 2009). ATI was determined on multiple ASTER image pairs of the Mono Craters. It was hypothesized that during the arid conditions of the summer season, the ATI image could provide a proxy for the mantling thickness on the domes (Ramsey and Crown, 2011).

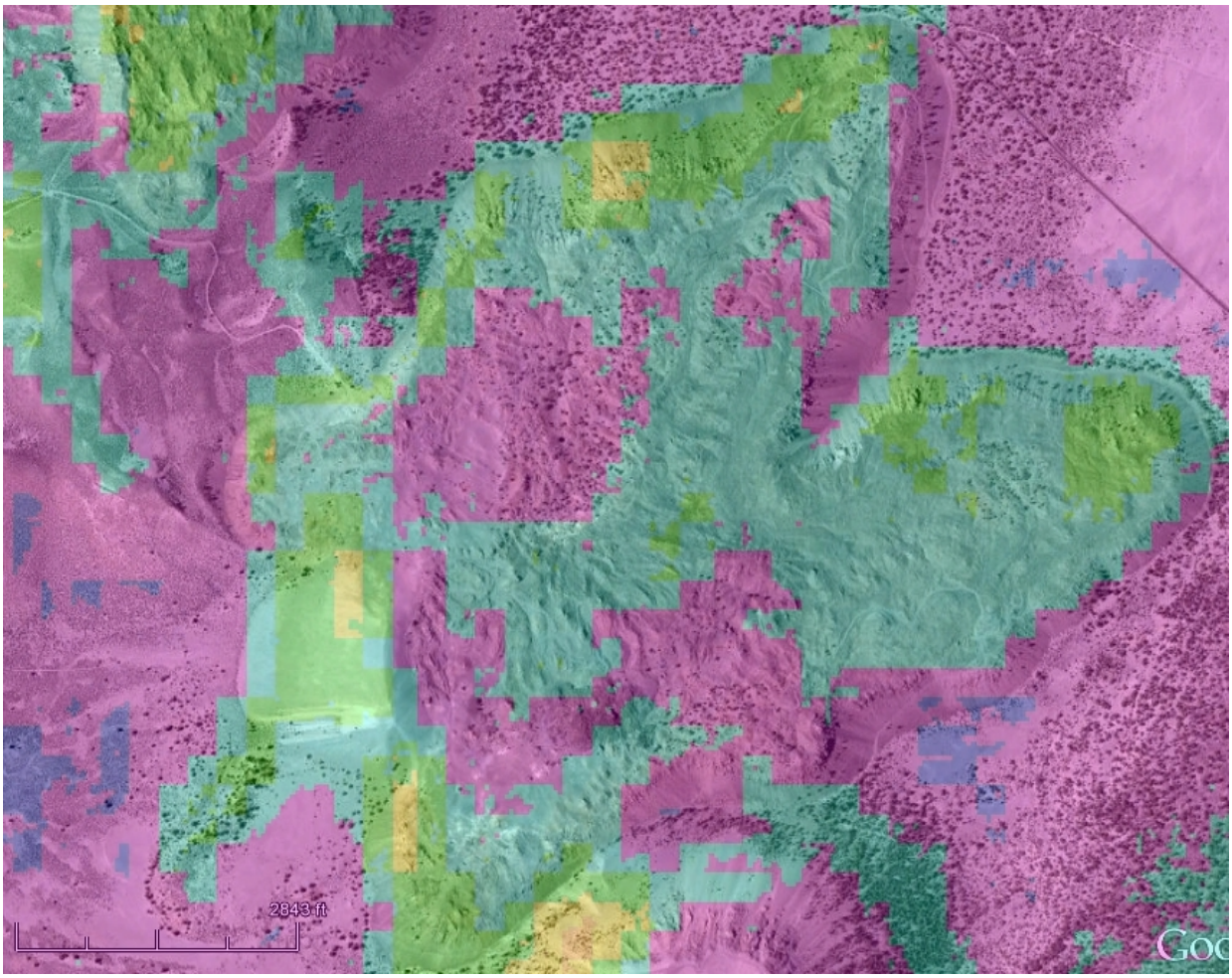

Figure 7: ATI map of North Coulee dome using ASTER images (from Ramsey and Crown, 2010). Purple represents low ATI, while teal, green, and yellow represent progressively higher values of ATI.

Perceived drawbacks of Earth-based thermal inertia proxies to accurate ATI modeling are the effects of soil moisture, especially if there is a change between the day and night data collection. Diurnal temperature values are sensitive to atmospheric humidity and soil moisture due to precipitation (Van de Griend et al., 1985; Rosema and Fiselier, 1990; Cai et al., 2007; Matsushima et al., 2012). Another issue is that the Earth's atmosphere produces efficient heat transfer between grains and the gas conductivity makes it much harder to create a true thermal inertia model like those created for Mars (another reason why ATI is used as a substitute to true

thermal inertia). The addition of condensation, fog, and dew to soil moisture creates a daunting problem for thermal inertia mapping. However in this study humidity and precipitation can be considered negligible in their influence. The arid conditions present during the summer months at the Mono Craters make humidity and issues with soil moisture an insignificant concern. Average relative humidity on July 10, 2011 (day of the ASTER overpass) was 33% (Weather Underground, 2013). Further, the Mono Craters are located in a semi-arid, high elevation area of California. Precipitation usually comes as snow during the winter months. The summer months (June – August) are usually dry with few clouds and precipitation events, which is optimal for remote sensing observations. However, rainfall near the ASTER overpass times/days could impact accurate ATI mapping. Therefore it was important to select datasets that had limited precipitation prior to collection. Rainfall data from the two nearest weather stations (Sonora Junction and Bridgeport Ranger Station) were obtained. Records from these stations (Figure 8) indicated a lack of precipitation in the month prior to the ASTER overpass (NOAA, 2013). Considering the low humidity and an average temperature at the Mono Craters in July of ~ 29 degrees Celsius (84 degrees Fahrenheit) (NOAA, 2013) it is expected that any surface moisture would have evaporated in the 10 days between last rainfall and the ASTER overpass.

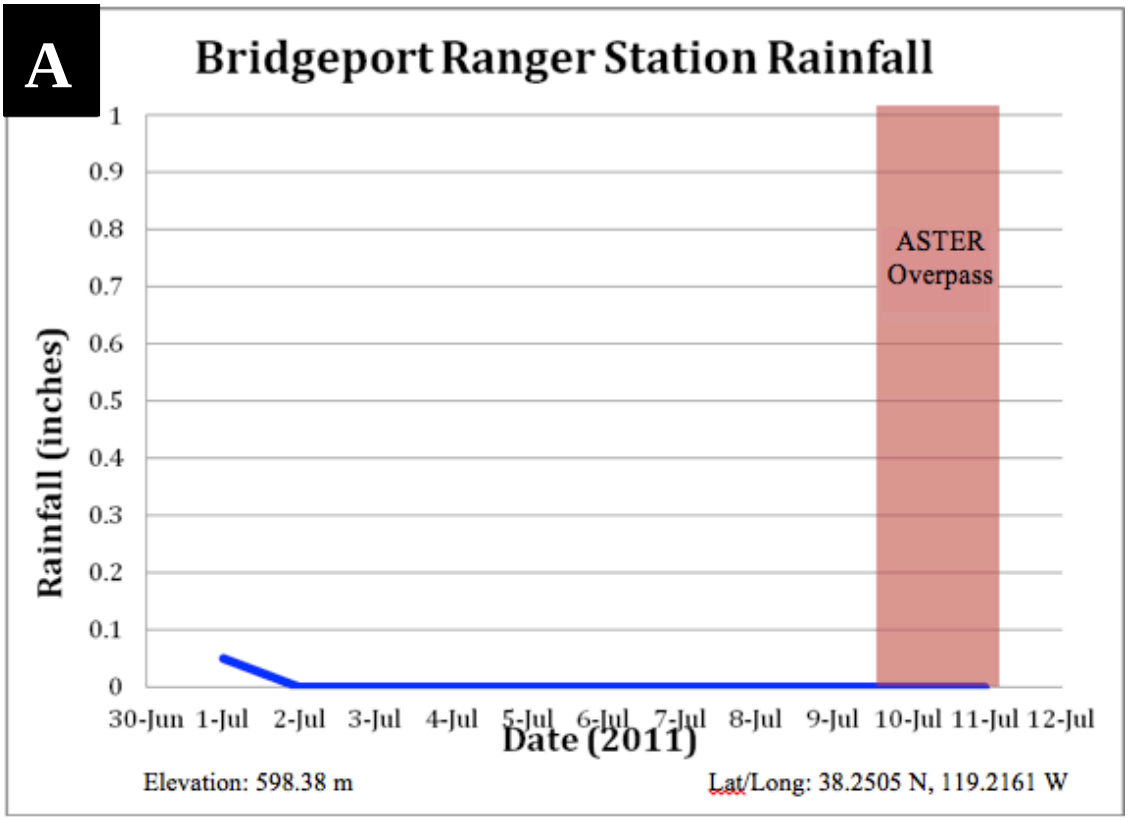
A
Bridgeport Ranger Station Rainfall
Rainfall (inches)
1
0.9
0.8
0.7
0.6
0.5
0.4
0.3
0.2
0.1
0
ASTER Overpass
30-Jun 1-Jul 2-Jul 3-Jul 4-Jul 5-Jul 6-Jul 7-Jul 8-Jul 9-Jul 10-Jul 11-Jul 12-Jul
Date (2011)
Elevation: 598.38 m
Lat/Long: 38.2505 N, 119.2161 W

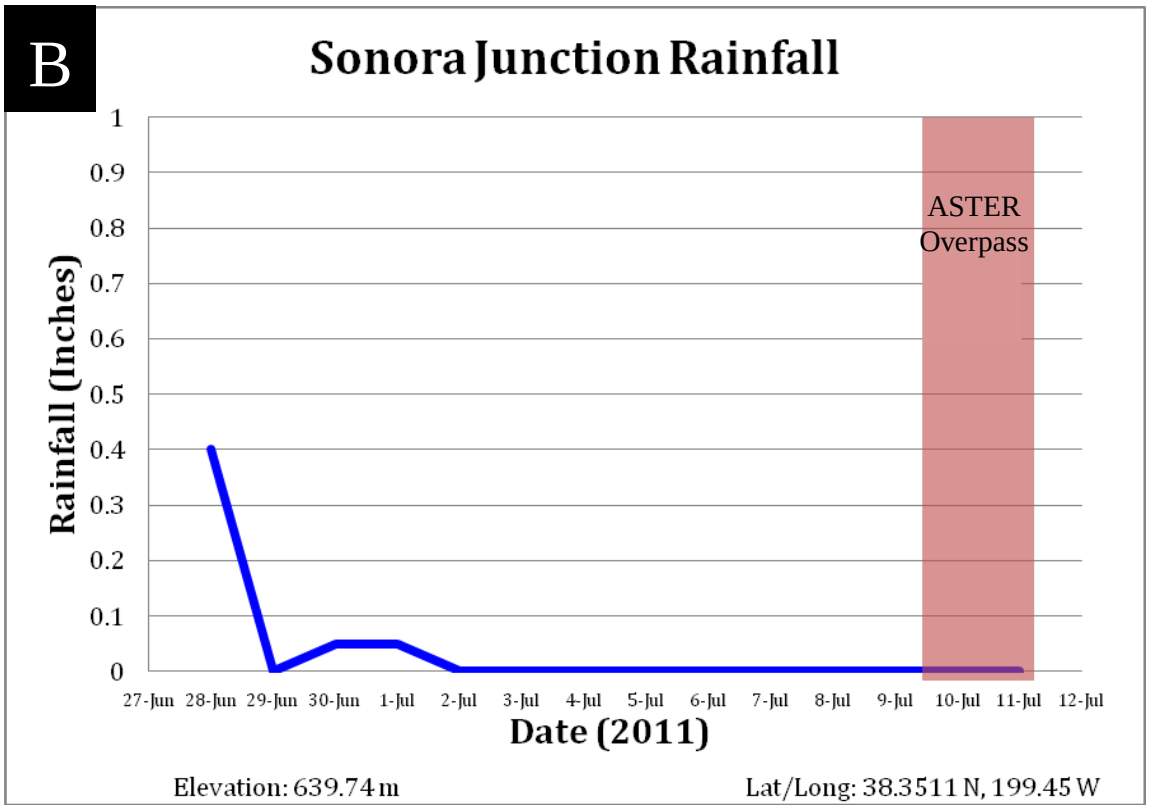
B
Sonora Junction Rainfall
Rainfall (Inches)
1
0.9
0.8
0.7
0.6
0.5
0.4
0.3
0.2
0.1
0
ASTER Overpass
27-Jun 28-Jun 29-Jun 30-Jun 1-Jul 2-Jul 3-Jul 4-Jul 5-Jul 6-Jul 7-Jul 8-Jul 9-Jul 10-Jul 11-Jul 12-Jul
Date (2011)
Elevation: 639.74 m
Lat/Long: 38.3511 N, 199.45 W

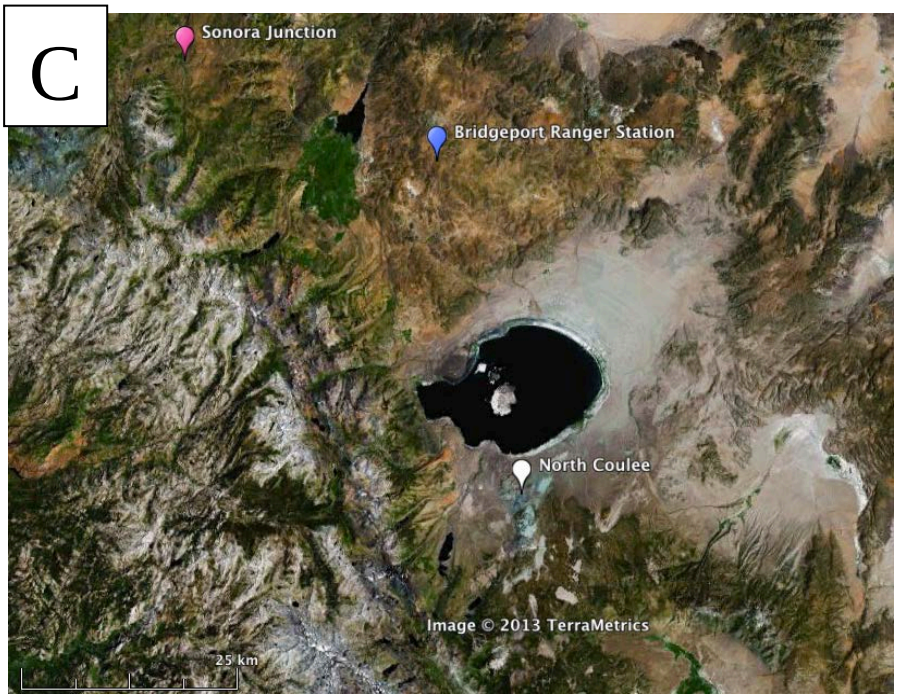

Figure 8: Precipitation records at weather stations nearest to the Mono Craters. Note the lack of rain before the ASTER overflight (July 10, 11) from which the ATI image is based. Rainfall is recorded in inches by the US Park Service. (A) Bridgeport Ranger Station. (B) Sonora Junction. (C) Map showing the locations of the two weather stations. North Coulee (white pin) is also shown as reference.

Chronologically similar (~ 30 hours apart) day/night level 1B ASTER images were selected using the USGS Global Visualization Viewer (GLOVIS) website (http://glovis.usgs.gov/). These images were fundamentally cloud-free, summertime images, with the day and night images being as close temporally as possible considering acquisition and geometry limitations. The high elevation of the Mono Craters can result in snowfall possibly being present at least nine months of the year, which would hinder ATI accuracy. Cloud cover (a norm for satellite-based imaging of the land surface) is also a hindrance to finding image data for ATI calculation. Summertime images are therefore optimal in this region considering the lack of snow on the domes and cloud-cover in the semi-arid region. It was also optimal to find images that were recently obtained to reflect the current surface as accurately as possible. The area is prone to wildfires that can leave surface signatures detectable to satellite imaging. Luckily a comparatively recent cloudless ASTER diurnal pair, dated from July 10 and 11, 2011, was

obtained to create the ATI product. The July 10 (day) image was collected at 18:50:47 GMT (12:50:47 local time) with a solar azimuth angle of 131.06° and a solar elevation angle of 68.11° (Scene ID: AST_09T_00307102011185047). The July 11 (night) image was obtained at 5:54:33 GMT (21:54:33 local time) (Scene ID: AST_09T_00307112011055433). Using the Environment for Visualizing Images (ENVI) software, the image pair was geographically aligned by rotating the images to north and cropping the images to identical UTM coordinates. It is imperative to align the two images as precisely as possible in order to compare the same areas (pixels) on the ground. Day and night temperature images were obtained from the ASTER L2 TIR radiance data product, which is corrected for atmospheric scattering and emission (Figure 9). An assumed emissivity value of 0.96 was used to separate temperature and emissivity from ASTER thermal infrared radiance images. This value was chosen after consulting past work on emissivity normalization techniques by Realmuto (1990) and Ramsey and Fink (1996). Using band math in ENVI, the pixel values of the nighttime temperature image were subtracted from those of the daytime temperature image to create a temperature difference product. This image highlights the change in temperature over a diurnal period and was needed for the denominator of the ATI equation. Next, Level 2 VNIR reflectance data were acquired from Reverb/ECHO (http://reverb.echo.nasa.gov). The GLOVIS website (glovis.usgs.gov) was used to search for and identify the image granule IDs. Albedo was calculated from the VNIR reflectance data by averaging the pixel values from all three VNIR images using band math in the ENVI software. Including SWIR images in the albedo calculation would have been optimal, but the SWIR data were unavailable for this research (detailed on page 27). To create the numerator in the ATI equation, the average albedo value must be subtracted from 1 using band math to create the numerator of the ATI equation. The final step combines both processed images into an ATI map

by dividing the 1-albedo image by the ΔT image. Again, the numerator and denominator image must be precisely aligned for accurate data collection. Figure 10 shows the finished ATI image after band math.

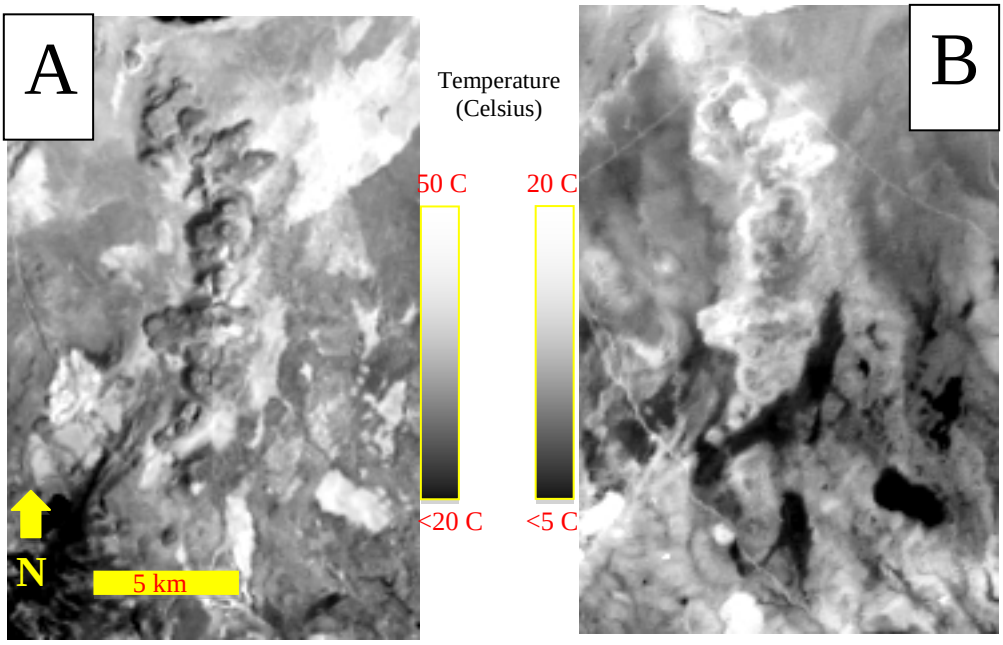

Figure 9: A day (A) and night (B) temperature image of the Mono Craters.

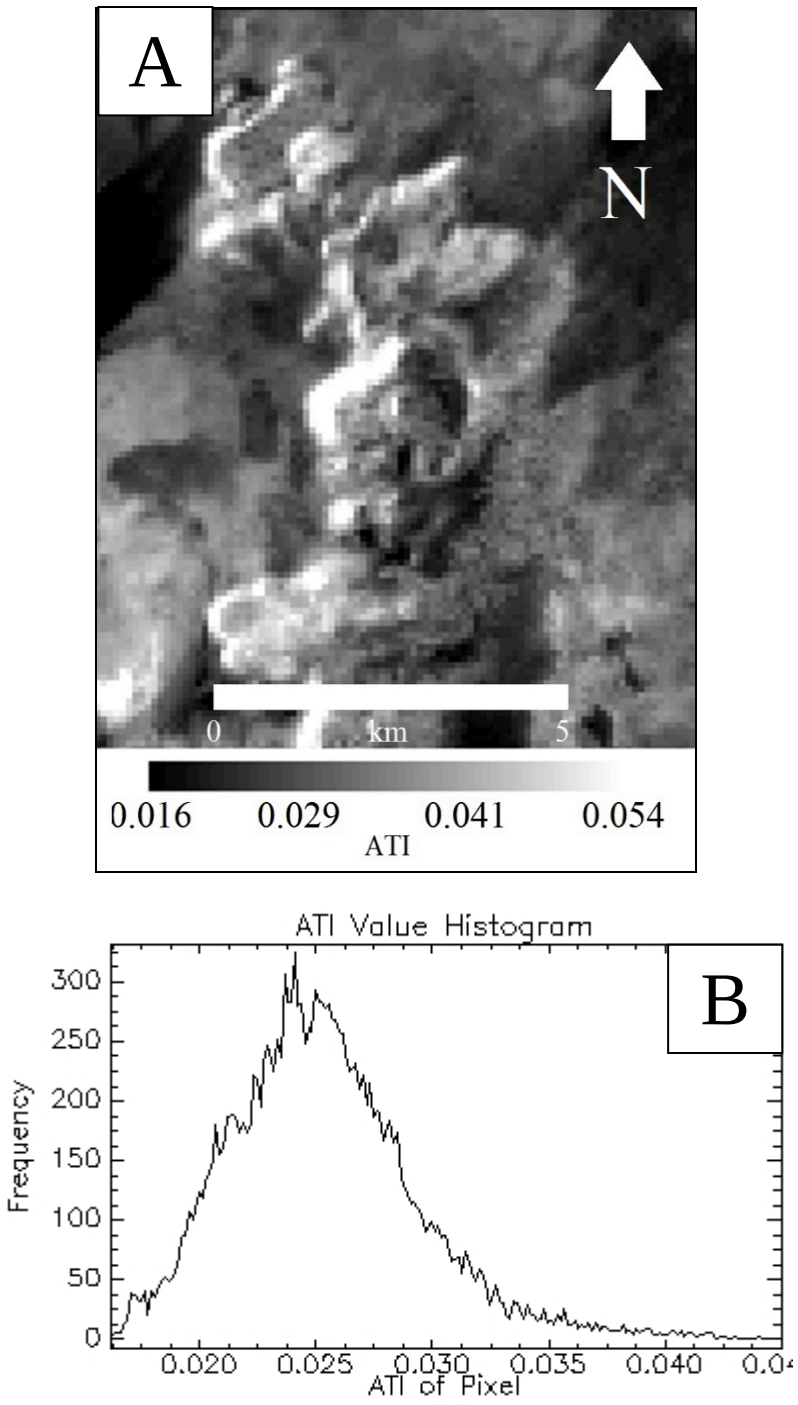

Figure 10: Apparent Thermal Inertia (ATI) map of the northern Mono Craters (A) and a histogram of ATI pixel values (B).

Optimally, it would have been best to use ASTER SWIR reflectance in addition to VNIR to obtain a more accurate estimate of broadband albedo. However, as mentioned - the ASTER SWIR bands have been unusable since 2008. Considering that the images acquired for this project dated from 2011, SWIR data were not utilized. Not using SWIR in a broadband albedo estimation can produce some level of error. However, this error is minimized here as the Mono Crater chain has an exclusively rhyolitic composition and the reflectance values of rhyolite in the SWIR would behave similarly (Mars and Rowan, 2010) and therefore including the SWIR reflectance would have lowered the (1-a) term uniformly on the domes. The lack of SWIR reflectance in a compositionally homogenous zone therefore is of minimal concern. However, if this area contained a wider variety of different materials with different SWIR reflectance values, the mixture of different spectra and lack of SWIR data could result in higher errors for the ATI calculation.

The ATI image was influential in selecting targets for field validation. It was imperative to select a variety of sites with diverse ATI values to determine potential surface roughness, grain/block size, and mantling thicknesses. Sites on the western portion of the craters were selected to establish whether the high ATI values present there were real or the product of solar heating/shadowing. ASTER TIR emissivity images were also instrumental in selecting areas of interest. Anomalies in the emissivity data were considered in potential field validation sites. The emissivity maps were then cross-referenced with the ATI image to select areas with varying surface roughness, ATI value, and composition.

2.1 FIELD

Figure 11: The upper flow surface of the North Coulee dome.

Fieldwork was conducted at the Mono Craters from July 13 to July 17, 2012. Only the North Coulee was the focus during because of the large size and limited accessibility of the domes. Roads created decades ago by US Pumice Corporation have been largely abandoned (Figure 11), and are now generally impassable even to 4-wheel drive vehicles. Considering these difficulties areas of interest had to be limited and reasonably accessible on foot. Nonetheless a variety of samples were collected from various regions of North Coulee. The eastern portion of the coulee was sampled a multitude of times because of the easier accessibility from the road (Figure 12). Other major sample sites included a large pumice deposit on the western face of North Coulee, an outlying dome on the southwest edge of the crater, and plains of fine-grained pumice

deposited near the western edge of the volcanic dome. The large pumice deposit was examined specifically because the ATI map indicated high thermal inertia at this site, which could have been the result of solar shadowing interference.

Figure 12: A Google Earth image of North Coulee. Stars represent sampled areas.

At the designated sites a variety of data were taken for later laboratory analysis and image validation (see Appendix B). If a layer of mantling covered a site, samples of the mantling deposit and underlying sediments were obtained. The depth of the mantled layer was also measured. Temperature was attained at four depths of the sediment (surface, 2 inches, 6 inches, and 10 inches, if applicable). If the site had no mantling, surface samples were taken for later laboratory analysis. Reference photos were acquired and a comprehensive description was gathered at each site. Contiguous rock-mantle contacts were geolocated using a Trimble XRS real-time differential global position system (GPS) unit. The spatial accuracy of the GPS was within 30-50 cm. One zone had a pixel survey conducted over a 90 by 90 meter square (the size of an ASTER TIR pixel). Observations were taken at a meter interval to get a thorough understanding of the sub-pixel compositional diversity of this specific ASTER pixel. In two particular areas a thermal infrared (FLIR) camera was set up to acquire an image approximately every 10 seconds for a 24-hour period (Figure 13). The first IR camera site imaged a large area with the camera focused on an entire flow front to highlight the differences in thermal inertia between the large blocks and mantling deposits. The second site was smaller (about half the size) and entirely mantled. This was done to validate thermal inertia change in mantled layers.

Figure 13: FLIR camera set up at a sample site.

2.2 LABORATORY

Upon return to the University of Pittsburgh, thermal emission spectra of all samples were measured at the Image Visualization and Infrared Spectroscopy (IVIS) facility. The instrument used was a Nicolet Nexus 670 at a $2cm^{-1}$ spectral resolution between 2000 and 400 wavenumber (~5-25 μm wavelength region). A thorough account of the measurement technique similar to IVIS is found in Ruff et al. (1997). Sediment samples were put in painted copper cups and heated to 80 degrees Celsius in a temperature-controlled oven for a 24-hour period. Each copper cup

containing a sediment sample was placed on a controlled heating stage within a sealed chamber, which was purged with compresses air scrubbed of water vapor and carbon dioxide to minimize their spectral effects during the measurement. The temperature of the cup was stabilized at 80 degrees Celsius during the spectral acquisition. The field of view of the apparatus was ~2 cm at the sediment surface. The surface was scanned over a period of ~5 minutes per sample. These scans were subsequently averaged to reduce instrument measurement noise. Raw emitted radiance data were then processed to emissivity spectra following the procedure of Ruff et al. (1997). The resulting emissivity spectra of the samples allow composition to be determined using approaches such linear spectral deconvolution (e.g., Ramsey and Christensen, 1998). The spectra were plotted against corresponding five-point TIR emissivity spectra obtained from the ASTER instrument using Microsoft Excel. The ASTER and IVIS data were then spectrally deconvolved in ENVI to ascertain vesicularity (e.g., Ramsey and Fink, 1999).

In addition to the spectral analysis, sediment samples were viewed under a petrographic microscope to examine various details of the samples. Point counting was conducted on a five by five centimeter grid to further confirm composition and grain size. Written notes were condensed and organized in digital format (See Appendix). The FLIR 24-hour thermal data were imported using the FLIR ThermaCam software. Various areas of the thermal image were examined specifically for their temperature change over time. These expanses were selected based on composition and mantling thickness. It was important to document a variety of textures, so a broad selection of zones with various levels of mantling (if any) was plotted. The temperature change of the vegetation present within the thermal image was also included for reference. These plots were then compared for changes in thermal inertia.

3.0 RESULTS

Apparent thermal inertia images derived from ASTER data contained measureable variances between portions of the dome (Figure 14). These differences correlate with levels of mantling on the surface. Figure 7 (Results section) is a preliminary ATI map previously created by Ramsey and Crown (2010) that was used as the theoretical basis for this work. Figure 14 is an ATI image created for this work using ASTER images from July 10 and 11, 2011. The results are nearly identical between both images and show statistically significant differences between mantled and unmantled pixel values. Unmantled pixels commonly had an order of magnitude higher ATI value than that of mantled pixels. Similar results were found throughout the domes and are suggestive of a larger trend.

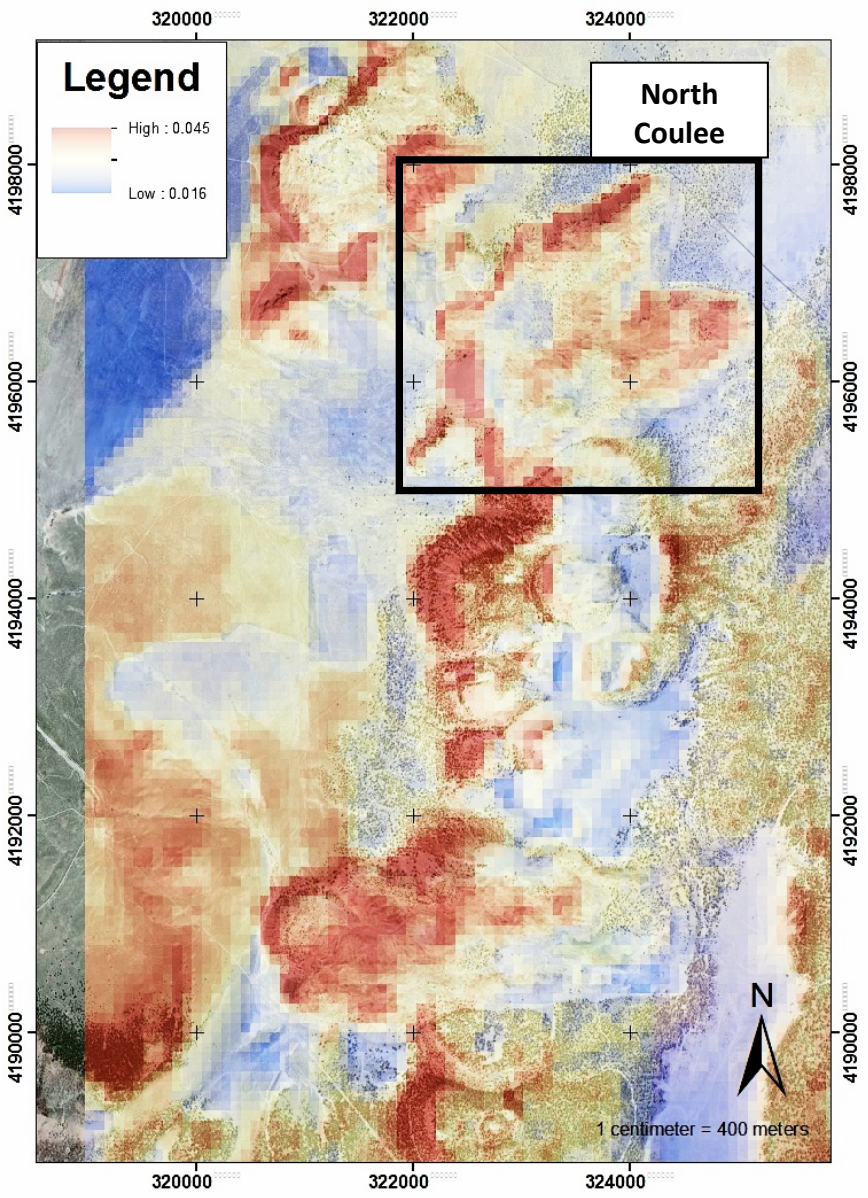

Figure 14: ATI map of the Mono Crater chain. The ATI image overlies an aerial map provided by Bing.

Considering the difference in size between eolian deposits and lava boulders, ATI also seemed to correlate well with relative block size. The theory was that lower ATI values associated with small-grained deposits, whereas a larger ATI was indicative of larger boulder-sized grains. Considering the volcanic environment, the majority of small-grained deposits on the Mono

Domes would be airfall mantling. From ATI image analysis areas associated with mantling had ATI values lower than 0.025 (Figure 15). Pixels with an ATI above 0.025 were associated with larger volcanic debris, and not zones of ashy mantling (Figure 16). High-resolution aerial images of the domes supported this hypothesis (Figure 16B and 17B).

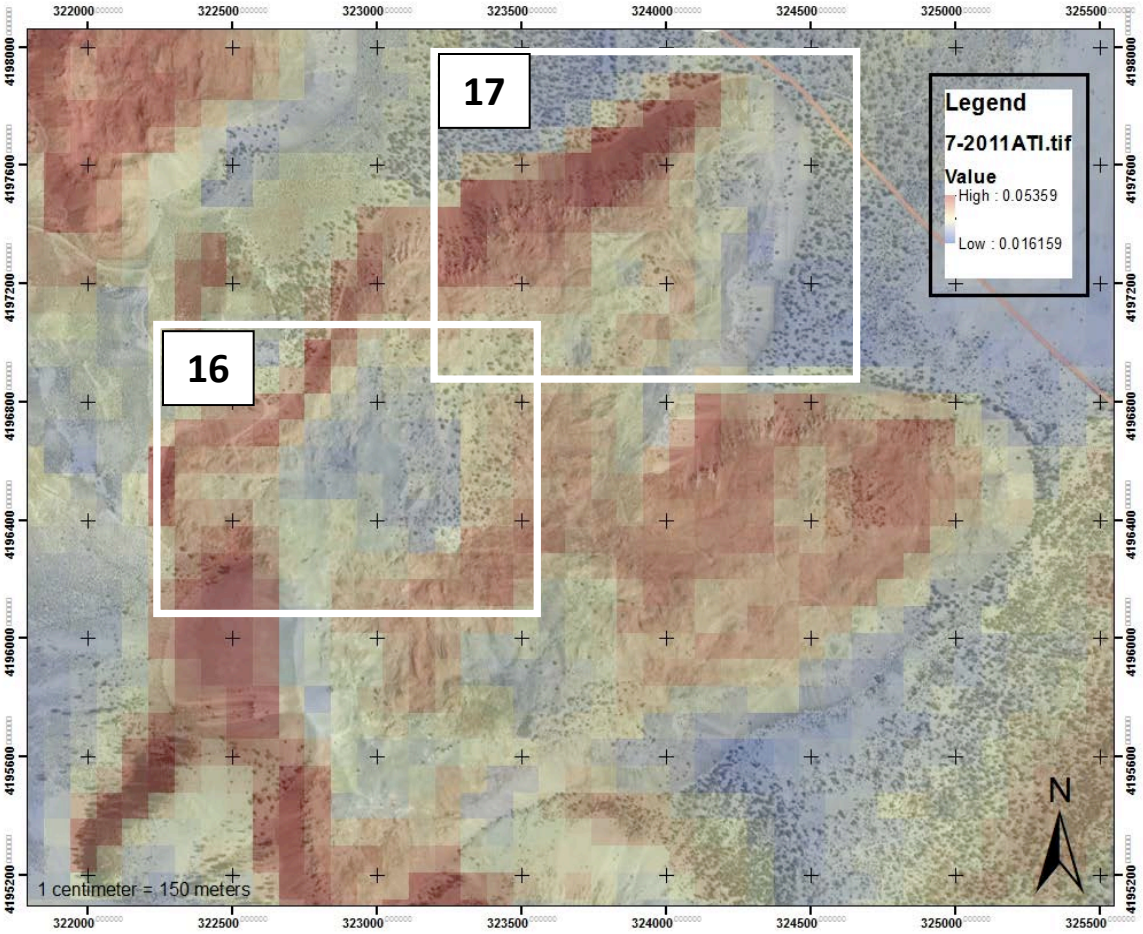

Figure 15: ATI map draped over an aerial image of the domes. White squares indicate the areas shown in figures 16 and 17.

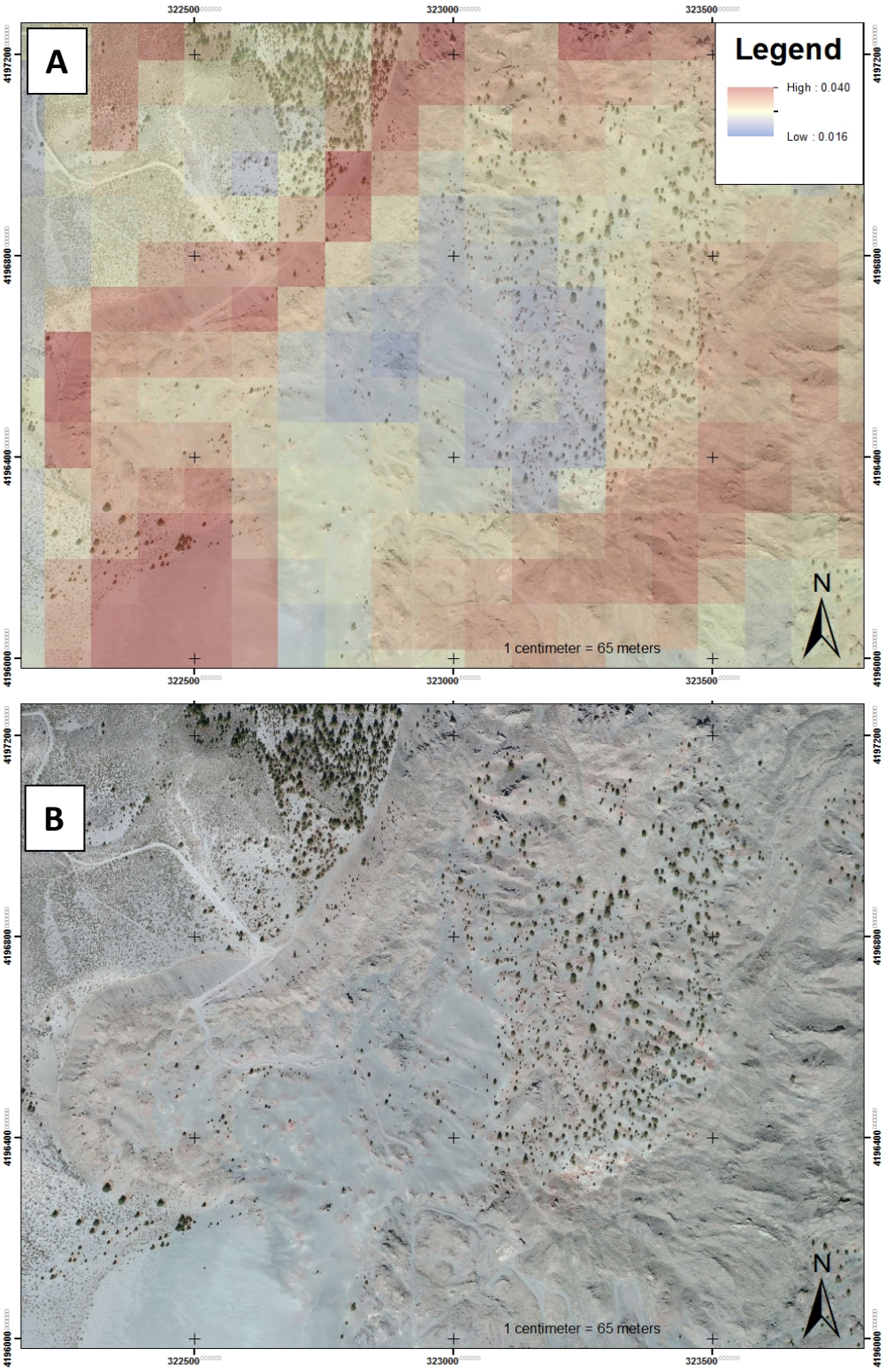

Figure 16: A comparison of an ATI map of western North Coulee (A) and high-resolution aerial view of the same area provided by Bing (B). Note the heavy deposits of volcanic pyroclasts visible in the low ATI zone in the center of the map, whereas rocky outcrops nearby display higher ATI.

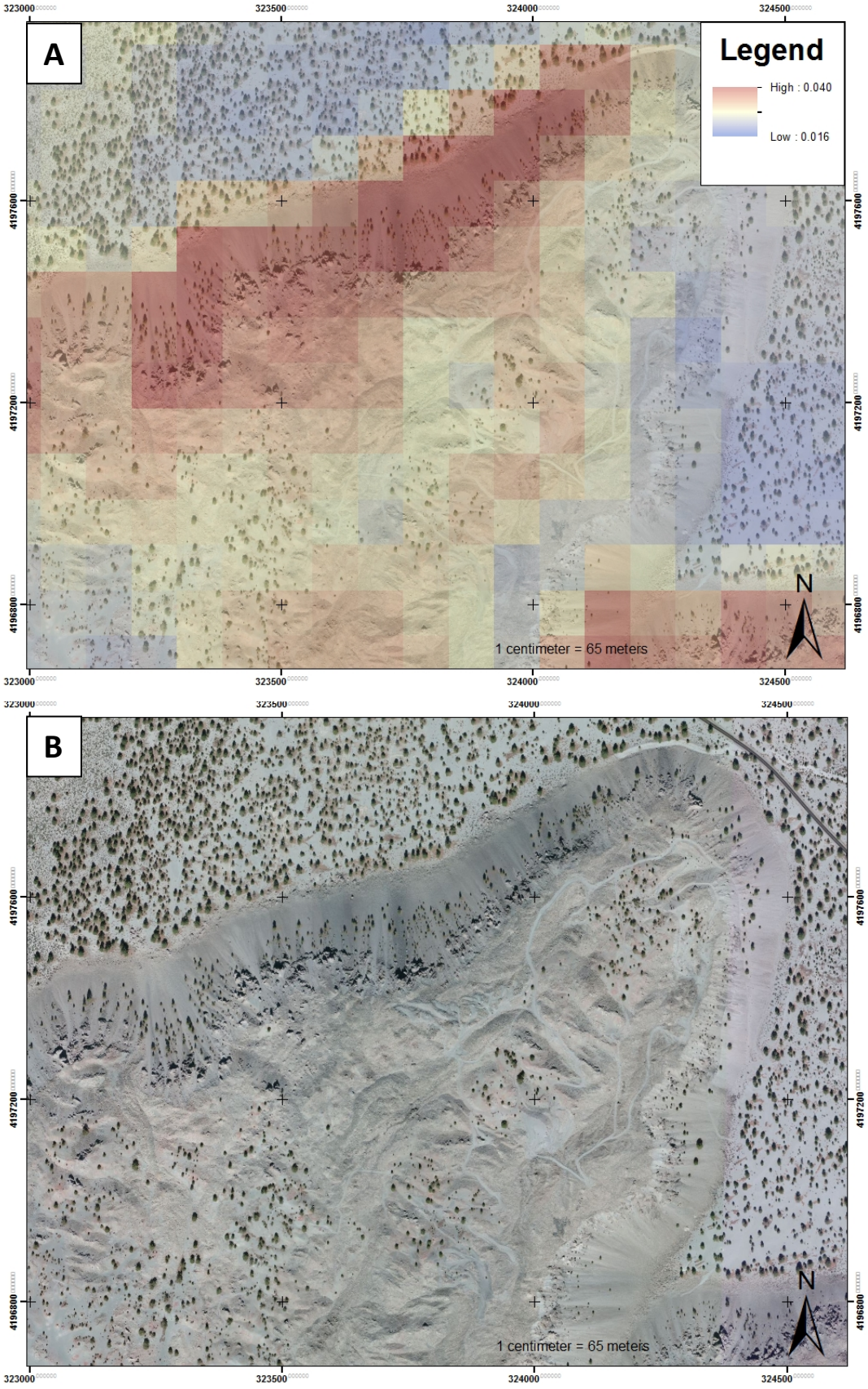

Figure 17: A comparison of the ATI map of northern North Coulee (A) and an aerial view of the same area provided by Bing (B). Note the rocky crags visible at the northern flow front of the dome, which exhibit very high ATI values.

Apparent thermal inertia does not correlate with ASTER emissivity spectra, however. The emissivity spectra show the silicate glass absorption feature near 9.1 microns, which is prominent in all the samples considering the recent volcanic origins of the Mono Craters (Figure 18). All spectra have a positive trend between 8.2 and 8.7 microns except the emissivity spectrum of the pixel with an ATI of 0.0239. This spectrum begins with a negative trend that is dissimilar to the other emissivity plots. The variance at this point can likely be attributed to an overcorrection of atmospheric water vapor in the ASTER data in this location (Gillespie et al., 1998). It is of note that this spectrum contains the lowest ATI of all graphed pixels in Figure 18. The band 12 (8.8 micron) emissivity value was plotted against the ATI value extracted for the same pixel and no correlation was noted (Figure 19).

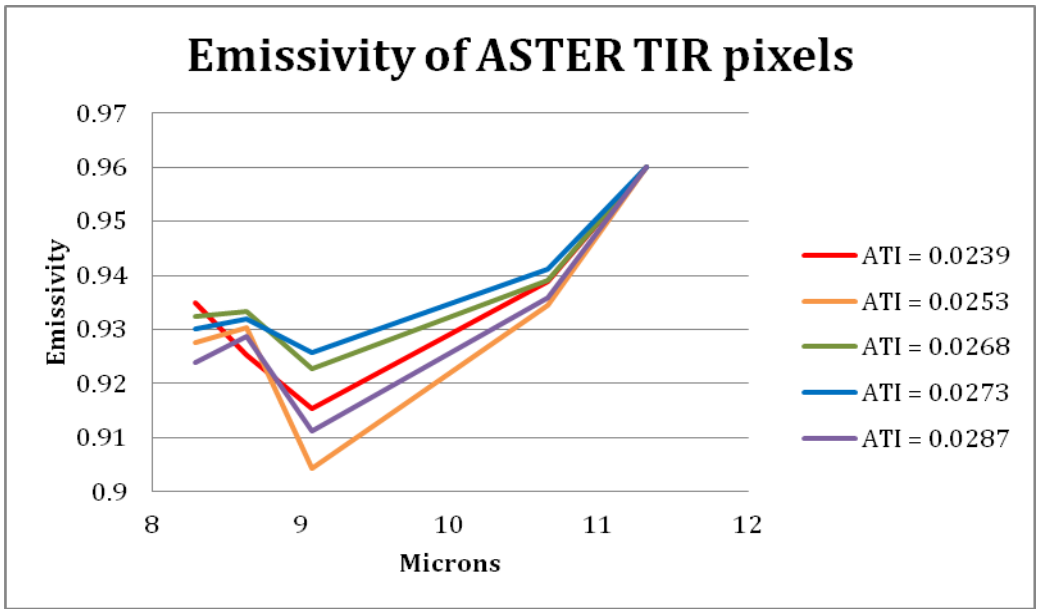

Figure 18: ASTER emissivity spectra of several field validation sites having different ATI values. Note the lack of correlation between band depth and ATI.

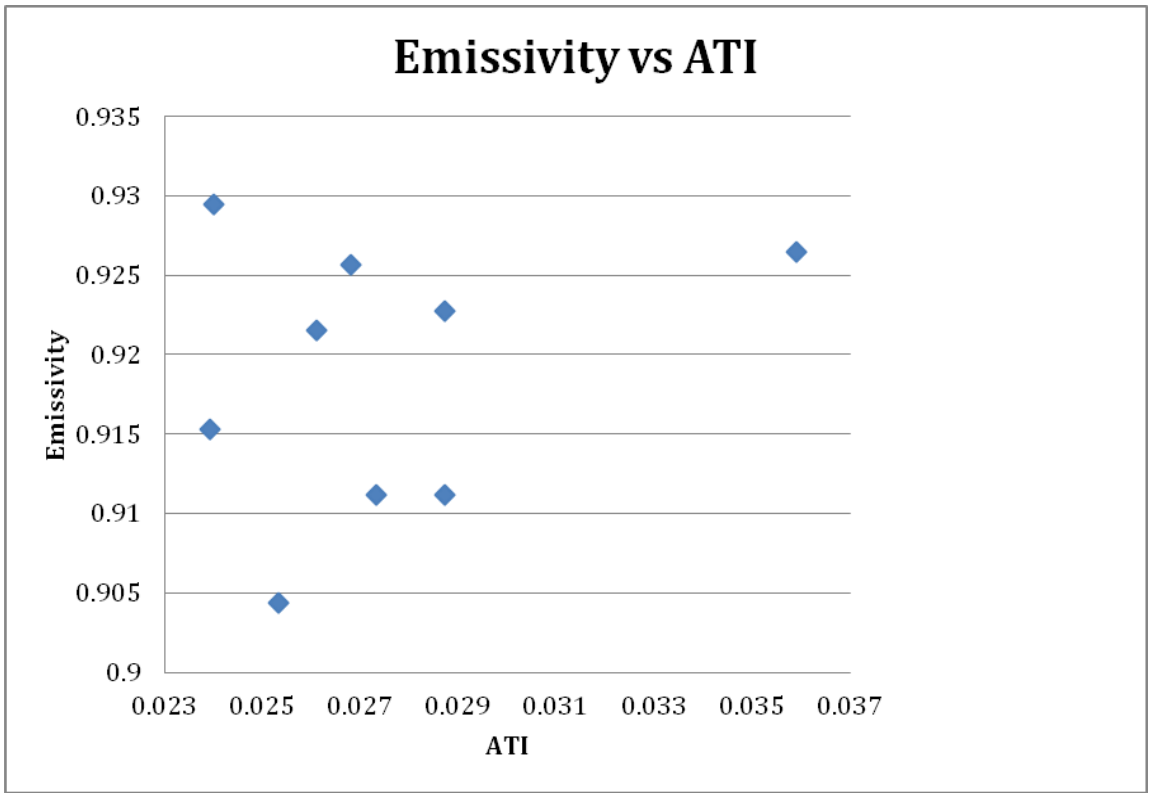

Figure 19: Band 12 (8.8 μm) emissivity plotted against ATI. Note the lack of correlation.

The results of field validation at North Coulee correlated well with our original image analysis (Figures 20 – 23). Areas of low thermal inertia predominantly consisted of volcanic pyroclastic airfall deposits (Figure 20); zones of high thermal inertia were exclusively large boulders (Figure 23). Zones with intermediate ATI values were harder to categorize. Some consisted of homogenous larger grains (Figure 21), and other sites contained a variety of different-sized sediment grains that mixed together into one intermediate ATI value. Pixel mixing provided a challenge to ATI grain size identification as a 90-meter ATI pixel could consist of various grain/block sizes within the same area.

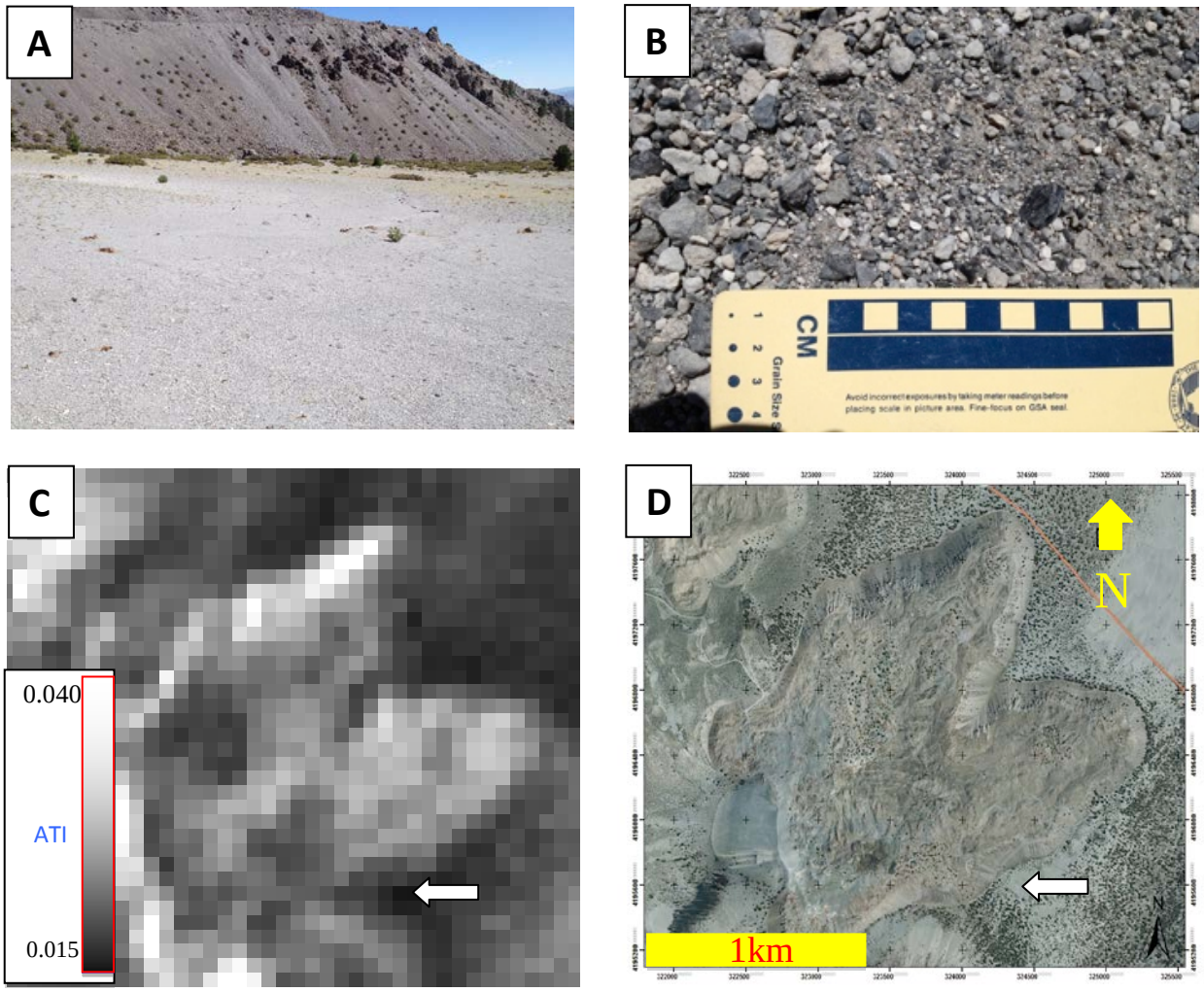

Figure 20: Ground validation of a low ATI pixel off of the dome (eastern edge of flow field). (A) Photo of site. (B) Close-up view of grains. (C) Location on ATI map (white arrow). ATI value of this pixel = 0.0195. (D) Aerial photo showing location of field site. Field validation of average grain size = 0.5 – 1cm.

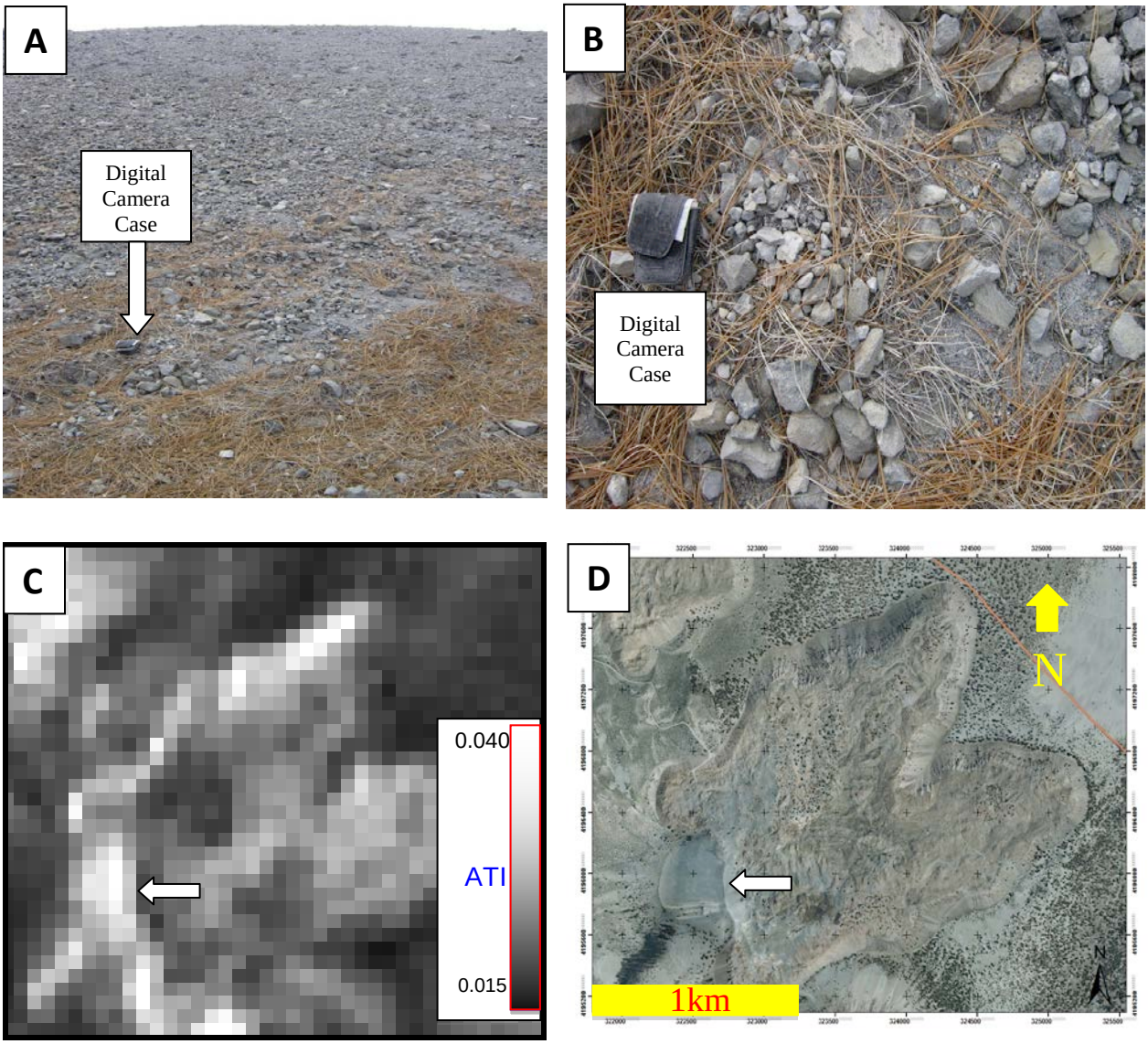

Figure 21: Ground validation of a homogenous ATI pixel with a moderate value. Note the lack of mixing. (A) Photo of site, note the larger grains compared to Figure 20. (B) Close-up view of grains. (C) Location of site on ATI map (white arrow). (D) Aerial photo showing location of field site. ATI value of this pixel = 0.0232.

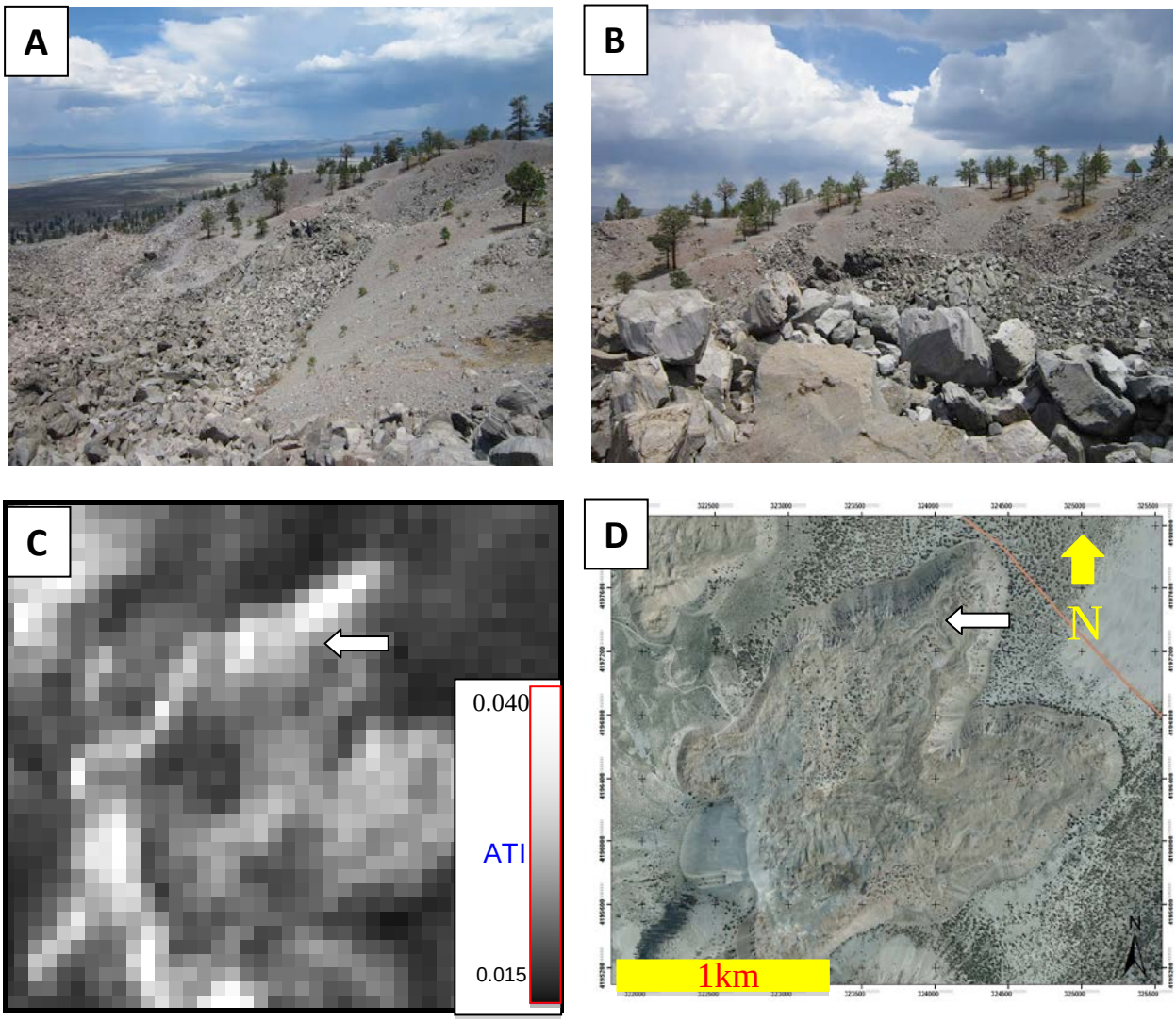

Figure 22: Ground validation of a heterogeneous ATI pixel with a moderate value. (A) Photo of site, note the mix of boulders and mantling grains. (B) A closer image of the area. (C) Location of site on ATI map (white arrow). (D) Aerial photo showing location of field site. ATI value of this pixel = 0.0258.

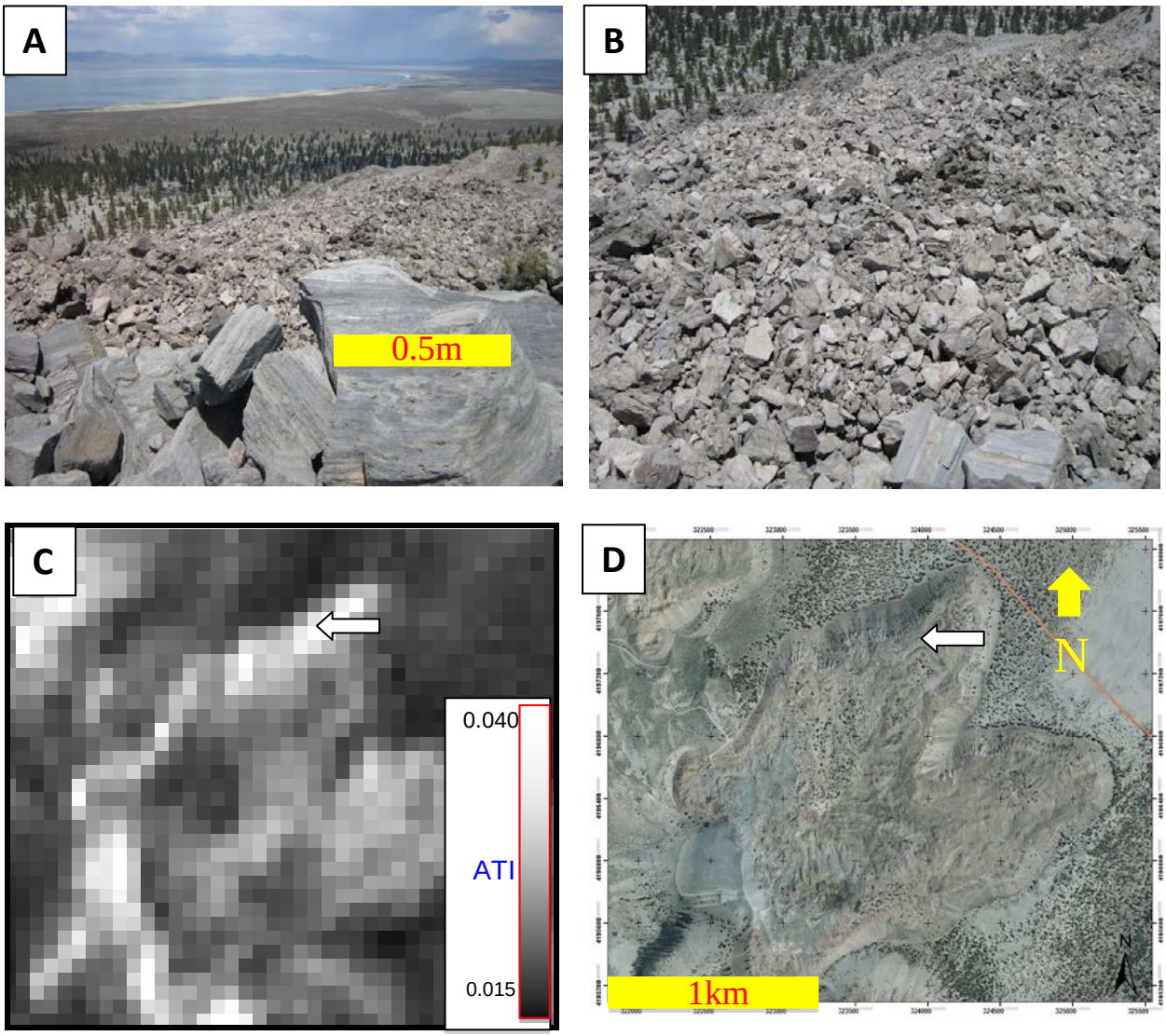

Figure 23: Ground validation of an ATI pixel with a high value. (A) Photo of site, note the large boulder-sized blocks. (B) A closer image of the area. (C) Location of site on ATI map (white arrow). (D) Aerial photo showing location of field site. ATI value of this pixel = 0.0287. Field measurement of average block size at site: 0.4m.

The area seen in Figure 20 (which will be referred to as Site 1) was located at the base of a flow front on southeastern North Coulee. This site was also the location to a 90m-pixel survey to validate the ATI imaging (Figure 24). The pixel being surveyed had an ATI value of 0.0195, a relatively low value compared to other pixels in the image. Considering that this pixel had an

ATI value under the theorized mantling limit of 0.025, it should be associated with fine-grained volcanic pyroclasts. The approximate mantling depth was measured to be 16 cm and corroborated the ATI results. These sediments had an average grain size of 0.5 to 1cm, with grains as small as 13 mm. The pixel was relatively homogenous in regards to deposition, and larger rocks were nonexistent. Minor amounts of vegetation was present in certain areas but was stunted and sparse (See Mono Crater Field Notes, Appendix).

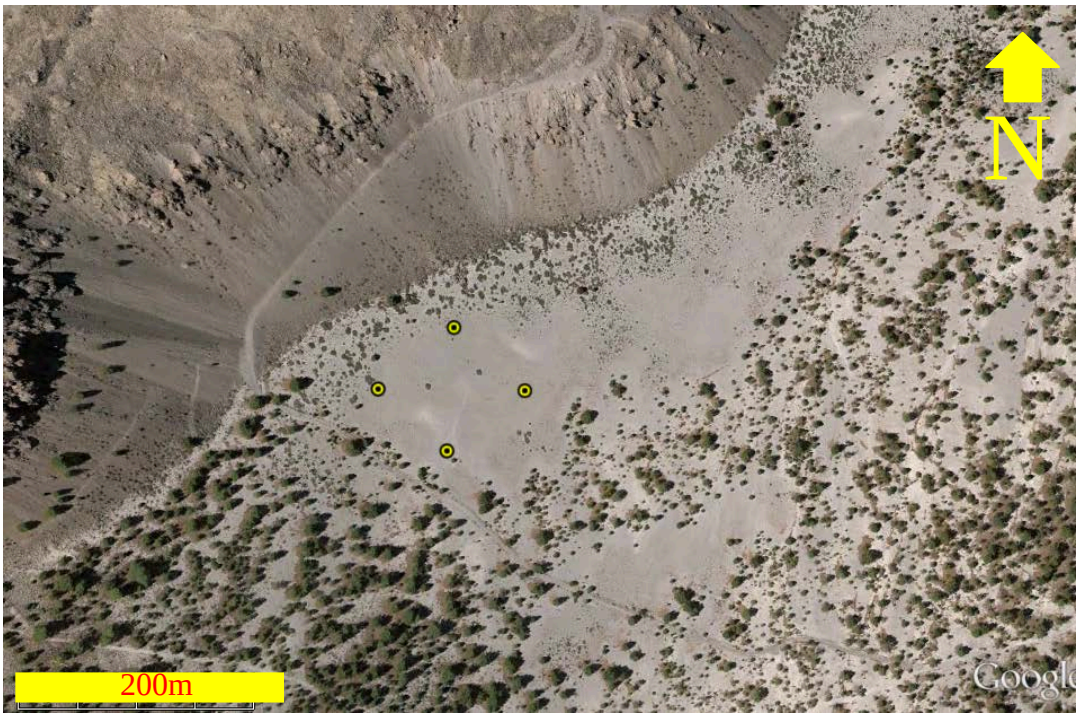

Figure 24: The approximate borders of the 90-meter pixel survey (yellow dots). This site is located near the southeastern flow front of North Coulee.

The location in Figure 21 (Site 2) was on the eastern slope of a large pumice deposit rising off of the western cliff of North Coulee dome. The ATI of this site was 0.0232, within the range of potential eolian ash deposition. The average grain size here (Figure 25) was larger than Site 1, and was measured to be around 1-2 cm, with grains as small as about 2 mm. This site also was fairly homogenous, but near to large mounds of boulders. There was no vegetation in this area.

Figure 25: A photo of Site 2 (Figure 21). The digital camera case is included for scale.

The area seen in Figure 22 (Site 3) was located in the northeastern section of North Coulee dome. Site 3 is a prime example of pixel mixing resulting in a moderate ATI value (0.0258). In the left side of the image large half-meter sized boulders dominate the landscape. Volcanic pyroclasts cover the right side of the image in Figure 22. A few trees and shrubs are growing in the fine-grained material, but the area is mostly barren. Average grain size for this area was not determined because of the great discrepancy between the two sections.

Site 4 (Figure 23) was located in northeastern North Coulee, about 100 m north of Site 3. The area was near the edge of the northern flow front of the dome. This section of the dome had the highest ATI values of all on North Coulee. The ATI value for Site 4 was 0.0287, which puts it beyond the threshold for eolian sediments. The blocks in this area were very large so a survey was conducted of boulder size over a distance of 50 m (see Figure 27, original data in appendix). Average block size determined from this analysis was 0.4 m. The largest block found was 720 cm, and the smallest was 170 cm.

Lab investigations of the field data reinforced the findings from fieldwork and satellite image analysis. It was determined through point counting on a 5 by 5 cm grid and consulting past research (Bailey 1989b; Hildreth, 2004) that sediment samples from the Mono Craters generally consisted of 75 percent rhyolitic pumice and 25 percent rhyolite-obsidian pyroclasts. The majority of sample sites contained well-sorted sand-sized particles. The average grain size in these areas was 25 mm or smaller. Several sites contained well-sorted gravel grains, but these were less common. Average grain size for these sites was approximately 150 mm. Four sites were considered poorly sorted, with grain sizes ranging from 6 millimeters to as large as 30 centimeters. Vesicles visible to the naked eye were present in two-thirds of the samples. It can be

hypothesized that vesicles are present in most if not all of the rhyolitic pumice samples, but not always visible.

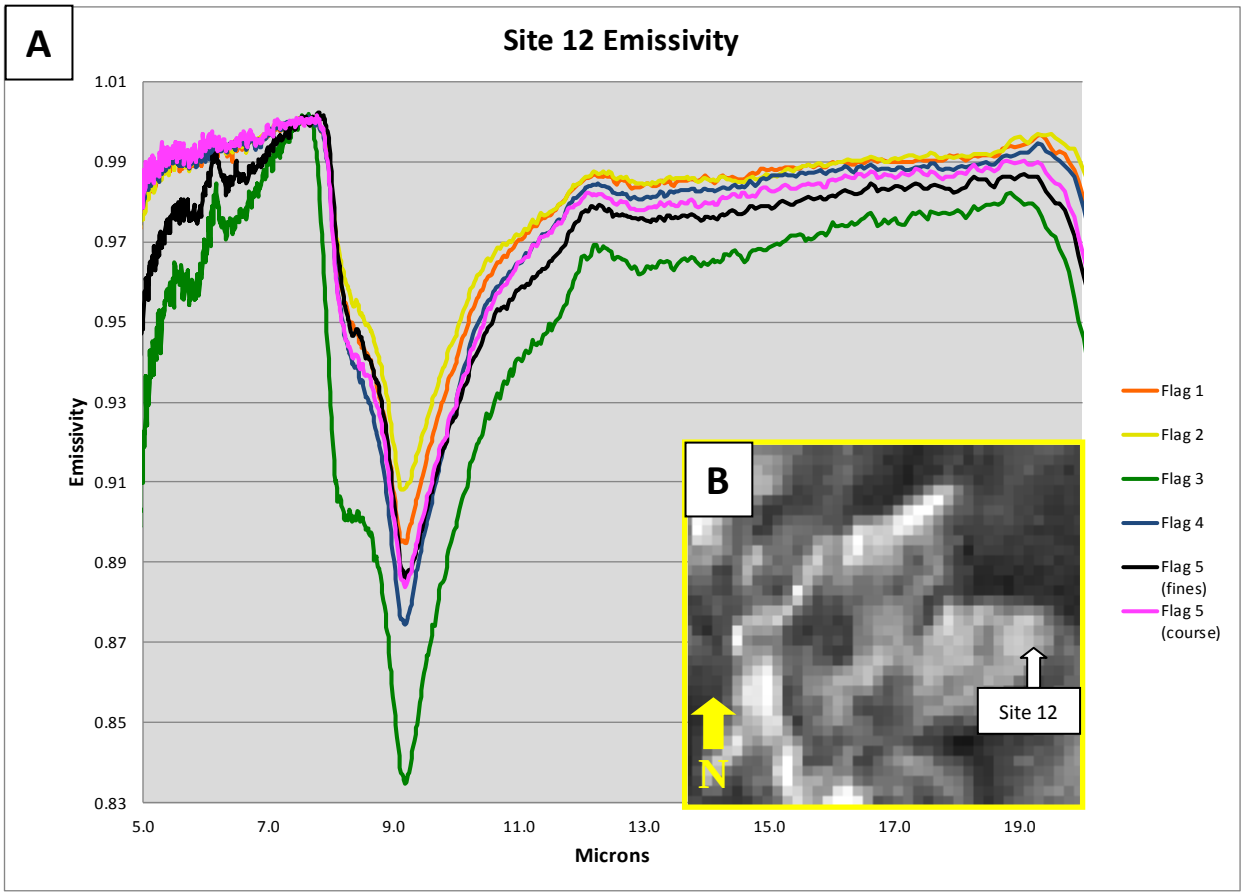

Figure 26: (A) Laboratory TIR emissivity of samples brought back from North Coulee site 12. (B) Location of Site 12 on North Coulee. The large absorption band at 9.25 µm is diagnostic of glass and is caused by the stretching vibrations of silica tetrahedra. Other lab spectra are available in the appendix.

Figure 27: A photo of the sample site analyzed in Figure 26.

Figure 26 shows the laboratory emissivity spectra of a few samples taken from a field site on top of North Coulee (Figure 27). Six samples were taken in this area to gain a representative model of the site. Nearly all of the samples contain identical spectra highlighting silicate glass (for greater detail on silicate glass spectra, see Lee, 2010). Flag 3 is the only spectrum that deviates from the normal values by trending lower in emissivity. This can be accredited to the sample containing less vesicles and/or small fragments and hence, more glass. This would result in a deeper emissivity feature. Another possibility is that the larger size of this sample (average grain size of 3-5 cm) makes it less prone to scattering effects seen in finer-grained samples. The feature at 9.1 microns is common to silicate glass absorption, characteristic

of the volcanic sediments at the dome. The abundance of silicate glass in the samples indicates the dominant occurrence of CVP and obsidian at the domes.

Data collected from the thermal inertia camera over a 24-hour period followed predicted trends (Figure 28, 29, 20). Figure 29 shows an example of temperature difference between different surfaces in a daytime and nighttime image. The obsidian boulders and vegetation near the top of the image do not display a major variation in temperature from day to night, whereas the small eolian mantling deposits exhibit a larger discrepancy. Thermal inertia therefore is much higher for the obsidian boulders than for the mantled sediments. A closer analysis of the images shows that thermal inertia is not equal in all of the mantling deposits. Some sediment retains higher thermal inertia than other areas. The variance in thermal inertia indicates a slight grain size difference. It is worth noting that this sample site could be constrained within one ASTER 90 m pixel and is potentially a site of pixel mixing.

Figure 28: A photo of the site analyzed with the FLIR infrared camera in Figure 29.

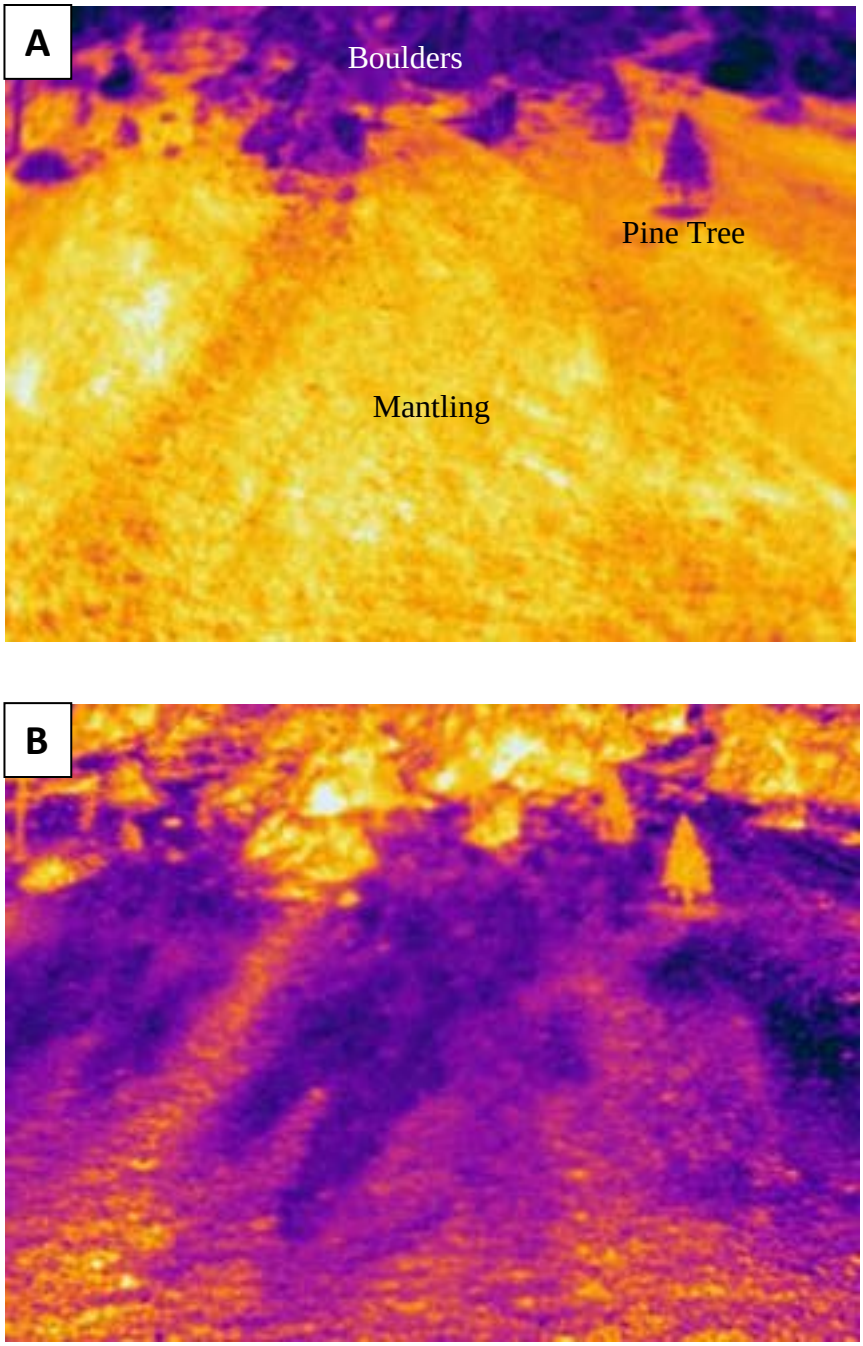

Figure 29: A daytime (A) and nighttime (B) thermal infrared image showing temperature change. Note the difference in thermal inertia between the boulders, mantling and vegetation.

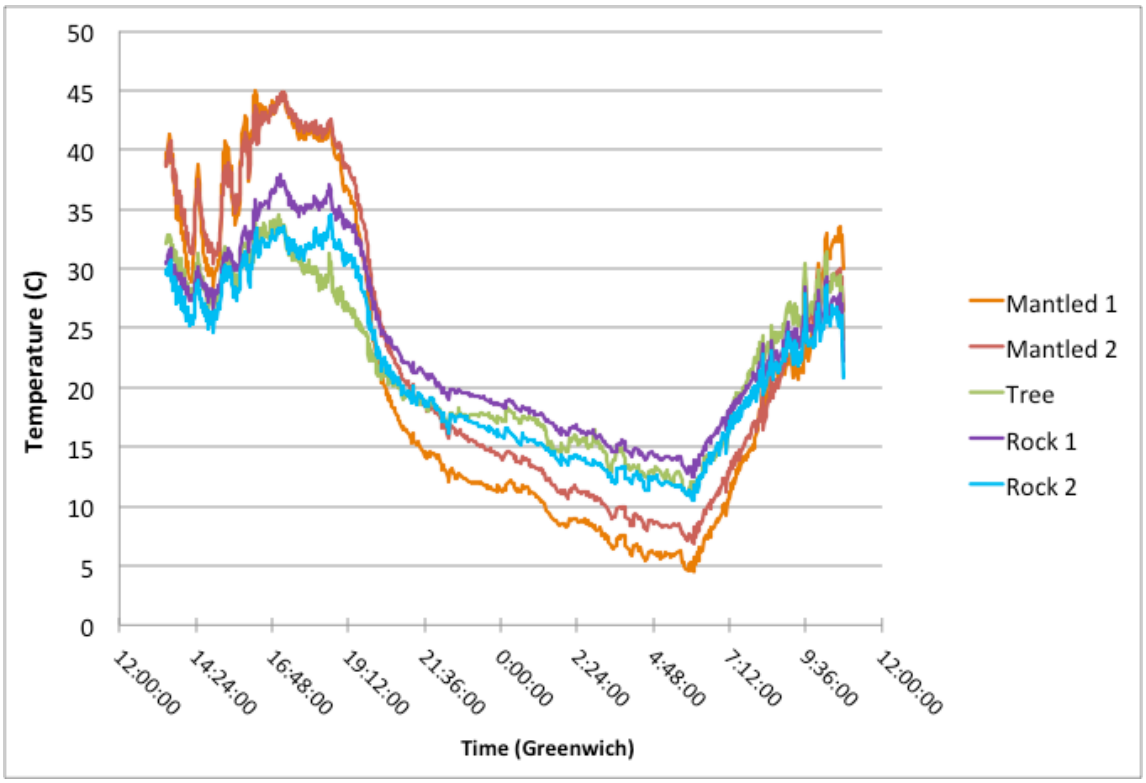

Figure 30: Data obtained from a FLIR camera graphing temperature over a nearly 24-hour period. An additional graph can be found in the appendix (Figure 38).

Figure 30 shows the results of the 24-hour infrared camera temperature study. The reason that temperature was measured in the field is that temperature change can be used as a first-order approximation of ATI (Xue and Cracknell, 1995). The two sample sites with significant mantling had a 40-degree temperature shift from day to night. The mantled zones reached a maximum temperature of 45 degrees Celsius during the day, and a minimum temperature of 5 degrees Celsius during the night. It is worth noting that the mantled sites had the highest peak-to-peak amplitude difference of all the samples. The two rock samples in comparison exhibited relatively constant amplitude. The temperature shift of these samples was approximately 25 degrees Celsius. The rocks reached a maximum temperature of about 37 degrees during the heat of the day and a minimum temperature of about 13 degrees during the night. A local Ponderosa Pine

Tree was also sampled for reference, and displayed thermal inertia properties similar to the rock samples. The tree actually had the lowest peak-to-peak amplitude of all the other samples. This is due to the low heat flux and high evaporation that characterize vegetation (Carlton et al., 1981). It must be noted however that only one site of vegetation was used, compared to two sites for particular sediment sizes. The tree reached a maximum temperature of 34 degrees and a minimum temperature of 12 degrees Celsius.

4.0 DISCUSSION

The ATI results (Figure 14, 20-23) indicate a correlation between the ATI value for a pixel and the average particle size. For the Mono Craters a pixel with a high ATI (> 0.030) consists of mainly of obsidian and rhyolitic boulders. Conversely, lower ATI (< 0.023) values identify areas of smaller grain size, such as volcanic pyroclastic airfall deposits. Considering the volcanic history of the area, most of the zones of smaller average grain size are areas of mantling. Pixels with an intermediate ATI (0.023 to 0.027) can be divided into two categories. The first encompasses pixels with homogenous, moderately-sized grains. Within this first group, pixels with ATI values between 0.023 and 0.025 generally consist of grains from 1 to 4cm, whereas larger ATI values (0.26 to 0.27) correspond to grain in the range of 5 to 250 cm. None of the particles in this moderate range were emplaced by eolian processes directly. While still considering mantling deposits for this study, these proximal airfall deposits were likely emplaced following parabolic trajectories onto the nearby North Coulee. The second group consists of pixels with a heterogeneous nature; the pixels have a mix of mantling deposits and unmantled larger blocks. Bearing in mind the history of volcanism at the Mono Craters, most 90 meter pixels are heterogeneous and contain mixing to different degrees.

Figures 20-23 show examples of pixels with varying ATI values and corresponding grain size. The ATI results allowed for a creation derived particle size map was created that approximated grain/block size over a 90-meter ASTER TIR pixel (Figure 31). Pixels with ATI

values near 0.020 indicate a very small average grain size (Figure 20). The pixel represented in Figure 20 has an ATI value of 0.0195. Ground validation revealed that average grain size for that area was 5 to 10 millimeters. The sampling zone consisted of mantling deposits that were identified to be about 16 cm deep (see Appendix for detailed notes). Areas of deposition tend to have grain size at or below 1 cm, with average grain size being as low as 2 mm. Because sand-sized (and smaller) grain size produces lower thermal inertia, pixels with low ATI values (around 0.020) seem to correlate with areas of these fine-grained deposits. The ATI of eolian sediments can range from < 0.020 to about 0.025 for deposits with larger grains. Sub-0.025 grains at North Coulee are universally associated with pyroclastic airfall deposits following eruption from Holocene activity. Ground validation supports the earlier theory that pixels with ATI above 0.025 are not associated completely with mantling (Figure 23). These large-ATI pixels are either heterogeneous, in which they would have small areas of mantling dominated by larger volcanic boulders (Figure 22), or they are homogeneous and are composed of grains too large to be modified by wind. Anderson et al. (2008) explains that block size distributions at the active Mount St. Helens (United States) and Mount Unzen (Japan) lava domes reflect stress conditions during flow. Vent regions generally contain the largest average block sizes and largest range of average blocks, whereas ridged areas tend to have the smallest average blocks. North Coulee seems to follow similar patterns to the Mount St. Helens and Mount Unzen flows. Figures 20 and 21 are situated near southern ridges, and contain homogenous, smaller fragment sizes. Figures 22 and 23, however, are further north on the dome, closer towards the 14th century eruption vents (Sieh and Bursik, 1986). Figure 22 is very heterogeneous, while Figure 23, the northernmost site, contains the largest blocks seen on North Coulee.

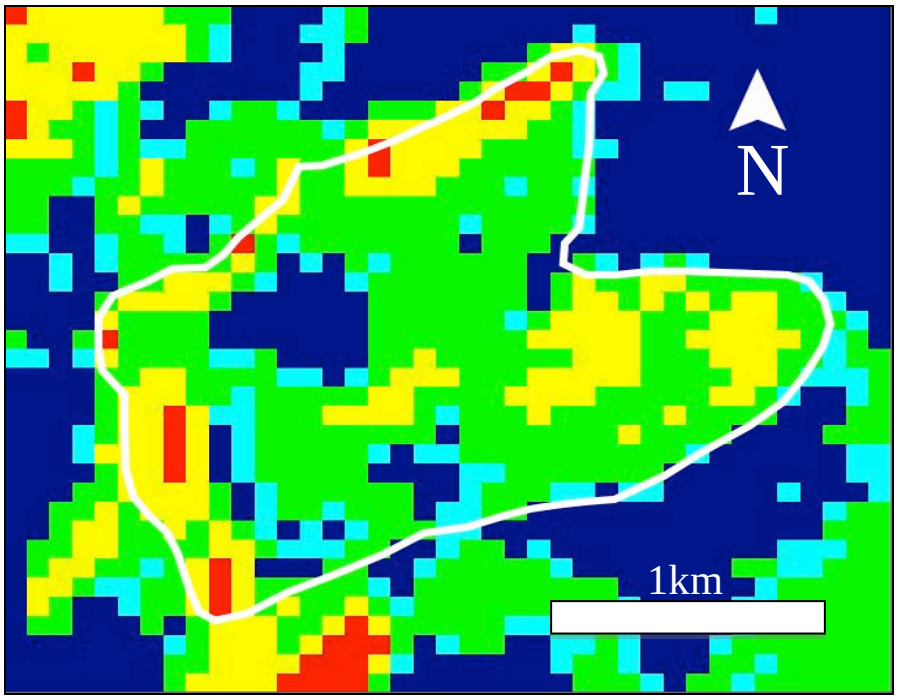

Figure 31: Derived particle size map of the North Coulee flow created from ATI data. The flow extent is shown by the white outline. Color of pixel indicates average grain size. < 1cm (blue), 1-3cm (cyan); 3cm – 0.5m (green); 0.5 – 1m (yellow); and > 1m (red).

Average grain size dramatically increases with ATI values above 0.025. Pixels with values beyond this threshold start to be associated with much larger pyroclastic airfall, lava flows, blocks, and other large volcanic debris. The higher the ATI value, the less chance that the pixel has significant mantling deposits present. Ground validation of an ATI value of 0.0287 (Figure 23) resulted in an average block size of 40 cm and a range from 17 cm to as large as 76 cm. Pixels with much larger ATI values were rare, as average grain size exceeding 1 meter over a 90-meter pixel was uncommon. Many boulder-sized blocks were identified in various locations on the surfaces of the Mono Domes, however a large multitude of these samples in a single pixel was not a usual occurrence. Flow movement of high-viscosity lava flows and general weathering tend to break up boulder-sized blocks into smaller, sub-meter sized fragments with distance from

the vent (Anderson et al., 1998). This correlated with the ATI map as pixels with values above 0.030 were generally found at the northern boundary of North Coulee: the closest location on the dome to the 14th century eruption vents. The largest ATI value found on the North Coulee was 0.0368, ~ 500 meters northeast of the location shown in Figure 23. This pixel bordered the north flow edge of the North Coulee dome, and was too dangerous to be able to sample directly. Figure 32 shows a histogram displaying block sizes of boulders at the Figure 23 site. Based on that histogram and the ATI values of nearby pixels, it is hypothesized that average block size of this pixel would be near or above 1 meter. Considering its close vicinity to a flow front, it is likely that a future landslide could lower the pixel's ATI value. ATI values above 0.040 were not found on North Coulee. A few pixels with values approaching this value were identified on other flows in the area (Northwest Coulee and west of Crater Mountain). Potential future fieldwork could determine the grain size and attributes of these outlying pixels to gain a better understanding of pixels with very high ATI values and try to separate the effects of topography/shadowing from actual ATI behavior.

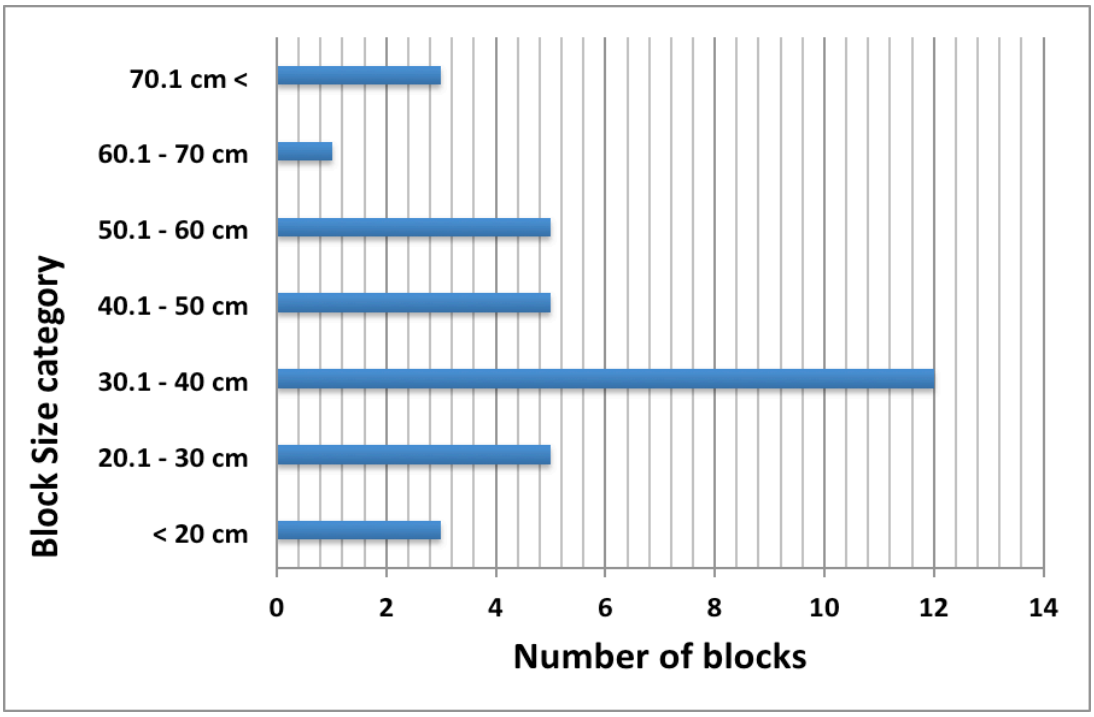

Figure 32: Histogram of block size of one ASTER pixel (Figure 23). ATI of pixel = 0.0287, Mean = 0.42 m, Median = 0.38 m, Mode = 0.20 m. See Appendix for original data collection and more histograms.

The ATI values are derived from the pixel-integrated temperature and albedo and therefore are a representation of the *average* block/grain size of that pixel. A 90-meter pixel of a lava flow can be composed of a variety of block sizes and mantling percentages, which are averaged in a single ATI value. For example, a very fine-grained airfall deposit would have a low ATI value (<0.020), but if this deposit does not cover an entire 90-meter pixel, then the ATI value will be skewed higher (e.g., Figure 22). However, this ATI average derived from remote sensing data is still of substantial interest. A low ATI value generally indicates a location with finer-grained material and potential eolian deposition, whereas pixel with a high ATI value implies the opposite. However, an intermediate ATI value could either indicate a pixel covered by a homogeneous deposit of slightly larger fragments or a linear mixture of fine grain mantling and larger blocks.

Christensen (1982) modeled the global thermal inertia on Mars using four spectral bands and the diurnal temperature measurements from the Viking Infrared Thermal Mapper (IRTM) instrument. With a proper thermal model and multiple measurements, it is possible to separate inter-pixel mixing and homogeneous cover of coarser grained particles. This level of analysis was beyond the scope of this study, however with TIR spectral resolution and ground based FLIR data, it should be possible to refine the block size map (Figure 28). Another approach would be to create smaller radiometrically-accurate pixels using a process called "super-resolution," which is an image processing and analysis technique used to improve the original (or native) spatial resolution of data (Hughes and Ramsey, 2013). This procedure creates 15 m ASTER TIR pixels, vastly improving the spatial clarity of the data. It has not been applied to nighttime TIR data as of yet and therefore is not available for ATI calculations. However, it would benefit ATI modeling by creating 36 new TIR pixels for every original 90 m pixel, which would allow for better discrimination between homogeneous and heterogeneous pixels within a certain area.

Bearing in mind the correlation between ATI and grain size obtained in the field and the detail seen in the high-resolution satellite images, the derived particle size map seen in Figure 31 can be considered a reasonable approximation for the grain/block size on North Coulee. Utilizing ATI to determine the block size on other silicic lava domes in Long Valley or elsewhere in the world could be easily implemented with the appropriate caution. ATI relies on diurnal temperature values, which can be skewed by climate conditions such as humidity, volcanic degassing plumes, and rainfall. Therefore, accurate atmospheric correction is critical. Furthermore, active domes could have temperatures well above the average background and internal heat would mitigate the normal diurnal heating/cooling process, thereby making ATI

unreliable as an indicator of block size and mantling deposits. Finally, vegetation cover also can be an issue on older domes. This process should be conducted on younger (no longer active) domes or in areas of arid conditions where vegetation has not developed on the flow. In addition, an accurate knowledge of the recent climate conditions prior to the data collection is essential.

One visible flaw detected in the Mono Crater ATI images is the effect of shadowing on derived ATI values. This is the result of the sun angle on the ASTER daytime image casting some areas of the western flow front in shadow. This changes ATI values as it lowers the albedo and daytime temperature, resulting in a higher ATI value than it should have based purely on the block size. One can see the effects of these shadows in Figures 14-17 as the western edges of most of the Mono Crater flow fronts have higher ATI values than the other slopes. However, because the main focus of this study is the flow surfaces and not the flow fronts, this error is less of a concern.

A possible correction for this effect would be to include a digital elevation models (DEM) into future ATI analyses. ASTER has the ability to generate along-track DEM's for every daytime scene in addition to the much higher accuracy global DEM (GDEM) product (Yamaguchi et al., 1998; Abrams et al., 2010). The hillshade product created from the DEM using the sun angle and elevation at the time/latitude of the daytime ASTER image could be incorporated to correct the albedo and temperature images. Another possibly more serious shadowing problem would be that of sub-pixel shadowing caused by larger blocks, which could also artificially increase the ATI values. This effect would be far more subtle than larger scale topography, but also much harder to correct. Synthetic aperture radar (SAR) could possibly be used to estimate the block size within the pixel and compared to those derived from the ATI. A discrepancy could indicate a subpixel shadowing effect. These corrections would allow for an

estimation of surface roughness and at least remove part of the error that sub-pixel shadowing can cause on ATI.

Finally, another correction could be the inclusion of scaling factors to the ATI equation. Scheidt et al. (2010) included two correcting variables (N and C_1) in the calculation of ATI using: $ATI = NC_1(1-a)/\Delta T$. N is a scaling factor, and C_1 is a correction factor that varies by latitude and solar declination (Vaughn, 1987). The equation to calculate C_1 is $C_1 = \sin\theta \sin\varphi (1 - \tan 2\theta \tan 2\varphi) + \cos\theta \cos\varphi \arccos(-\tan\theta \tan\varphi)$, where θ is the latitude, φ the solar declination (Nasipuri et al. 2006). The effects of N and C on the final ATI value are very small and would not correct for larger scale topographic effects. Therefore, N and C were not deemed necessary in this ATI study, which was attempting to find a general approximation of fragment size difference over a large area. Now that the initial ATI images have proven accurate in their estimations of block/grain size, N and C should be applied in future research in order to assess any improvements to the accuracy of the ATI results.

The correlation between apparent thermal inertia and emissivity of the ASTER pixels and field sample spectra was very poor, but not surprising. Considering the positive correlation of ATI to grain size, it was prudent to examine whether ATI was also correlated with surface emissivity. Results of this study can be seen in Figures 18 and 19 in the results section. This lack of correlation can be explained simply by the composition and texture of the rocks present at North Coulee and the Mono Craters in general. The Mono Craters and airfall mantling deposits all consist of high silica rhyolite (Hildreth, 2004). Therefore, we would expect the emissivity of all the surfaces to be similar, whereas the variation in ATI is caused solely by the differences in particle size. Another minor contributor to the non-correlation between emissivity and ATI is the vesicularity of CVP present at the Mono craters. The vesicularity of a lava's surface will change

the emissivity spectrum (Figure 33) (Ramsey and Fink, 1999). Vesicles present on a surface will move the emissivity absorption more toward that of a blackbody thus making the spectrum more featureless (Figure 33). This would have a minor effect on observed emissivity spectra of these vesicle-rich surfaces which would likely not be correlated with the ATI results.

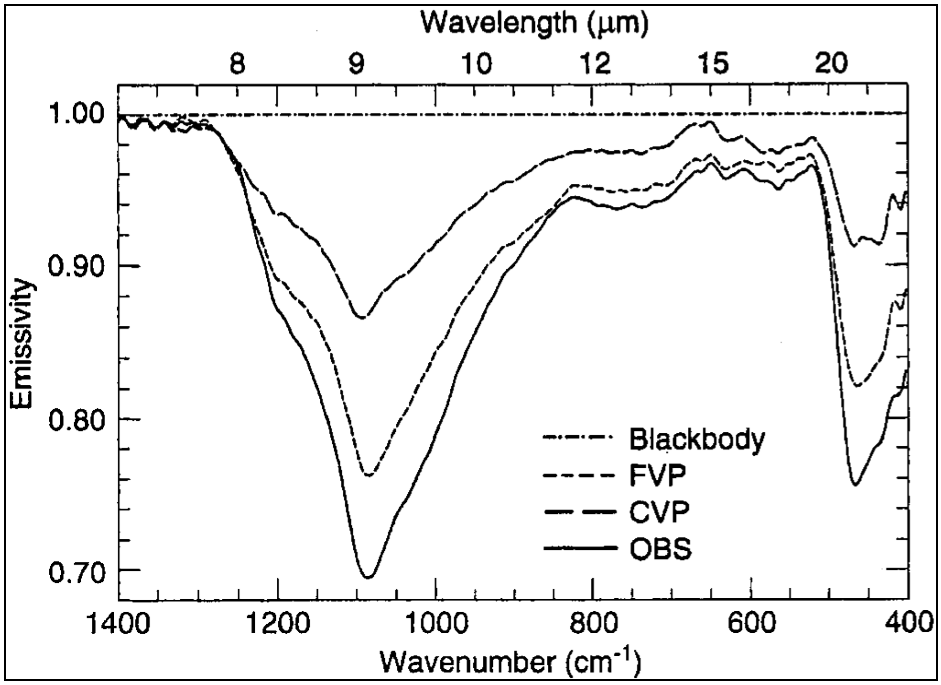

Figure 33: Emissivity spectra from Ramsey and Fink (1999). The spectra listed are fine vesicular pumice (FVP), course vesicular pumice (CVP) and obsidian (OBS) obtained from Medicine Lake, CA. Spectra shown are averages of at least ten samples to account for orientation and weathered surface effects.

The 24-hour temperature analysis provides on-site verification of thermal inertia changes correlating with grain size (Figure 30). Mantled pixels in the FLIR data had 40-degree temperature change over 24 hours, indicating low thermal inertia. The temperature change for large obsidian boulders was much more consistent, having only a 25-degree change over 24

hours, which signifies higher thermal inertia. Mantled areas showed variation in temperature shifting in a day to night cycle. Some mantled sections cooled faster than others upon nightfall, a significant factor (Figure 34). This is noteworthy as it is grain size that is facilitating this differentiation in cooling. This indicates that diurnal temperature measurements can help distinguish zones of different grain size and also be used to validate the grain sizes extracted from the image-based ATI values. This fact helps validate using ATI for grain-size discrimination considering that diurnal temperature images are present in the denominator of the ATI equation. The inclusion of albedo in the numerator of the ATI equations makes grain size demarcation even more precise since ATI accounts for reflectance, which can hinder accuracy of temperature image results.

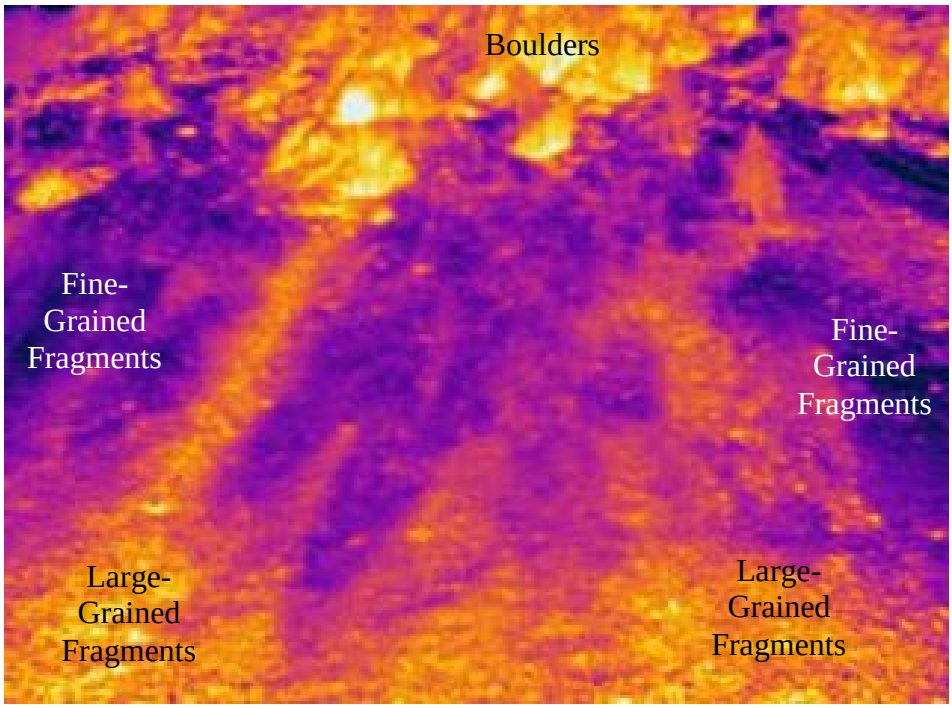

Figure 34: An evening temperature image of an eastern flow front of North Coulee. Smaller particles have already cooled off, whereas larger grains are warmer, indicating a thermal inertia change. More images of this site can be found in Figure 29.

4.1 APPLICATION TO MARS

The image processing techniques applied to the Mono Craters could be applied to similar mantled volcanic surfaces on Mars. Like the Mono Craters, these regions have been imaged by high-resolution VNIR and TIR datasets and contain areally extensive lava flow fields and variable dust and sand cover. Accurate characterization of the lava flow composition and decoupling from the overlying mantling material is important for understanding martian volcanism in these two regions. Proposed future research will focus on two similar but distinct sites: the lava flows on the SW apron of Arsia Mons and into the plains (Daedalia Planum) surrounding Arsia Mons to the south, and a volcanic plateau crossing Syria Planum also stretching into Solis and Sinai Planum.

Arsia Mons, the southernmost of the three prominent Tharsis shield volcanoes (Figure 35), has a well-developed summit caldera and well-developed lava flow fields (Crumpler and Aubele, 1978; Crumpler et al., 1996; Head et al., 1998a,b; Mouginis- Mark, 2002). There are two large flow aprons with a multitude of individual flows and flow lobes that extend from alcoves on the lower NE and SW flanks of the volcano that postdate its main shield (Plescia, 2004; Scott and Zimbelman, 1995; Lang et al., 2009; Ramsey and Crown, 2011). The SW flank flows are found in an area roughly between 10° and 30°S and 110° and 140°W. This zone includes the relatively flat-lying terrain south of the steeper flanks slopes of Arsia Mons (Figure 31). Previous imaging work in the area includes series of 1:2M scale lava flow maps of the Tharsis region by

Scott (1981) and Scott et al. (1981a,b) using Viking Orbiter images. More recent studies have utilized Mars Express High Resolution Stereo Camera (HRSC) images to examine evolutionary stages in effusive volcanism in the Tharsis region, including the Arsia Mons shield (Bleacher et al., 2007). Lang et al. (2009) examined this flow field further south where the dust mantling is lower. The spectrally derived composition was found to be basaltic with a possible affinity to the basaltic shergottites. These flows have a moderate Thermal Emission Spectrometer (TES) derived albedo (0.22 – 0.24) and dust cover index (0.95 – 0.97) (Ruff and Christensen, 2002; Ramsey and Crown, 2011). The second potential location is a flat-lying plateau located at Syria Planum (along with Solis Planum and Sinai Planum). This area is bordered by Noctis Labyrinthus to the north and the Thaumasia highlands to the west and south. New high-resolution datasets from the High Resolution Imaging Science Instrument (HiRISE) reveal a diversity of volcanic landforms and a multitude of tectonic features that vary in scale and are suggestive of the region's geologic complexity (Ramsey and Crown, 2011). Previous mapping of the Syria Planum Formation by Dohm and Tanaka (1999) and Dohm (et al., 2001) interpreted the plateau be Late Hesperian in age. The northern part of Syria Planum is highly mantled but there is a steady decrease in dust mantling to the south and large areas of low dust cover on the plateau. There are numerous images of the lava flow surfaces that reveal a mix of lava outcrops and fine-grained mantling materials from HiRISE and the Context Camera (CTX) on Mars Reconnaissance Orbiter (Figure 36) as well as the High/Super Resolution Stereo Color Imager (HRSC) on the Mars Express Orbiter. The variation in this region provides a fitting test site for martian eolian mantling approximation utilizing the thermal inertia procedures developed at the Mono Craters. This second site at Syria Planum presents a valuable comparison to southern Arsia Mons given their adjacent locations but different volcanic styles (shield

volcano/surrounding plains vs. plains), variability in dust cover, and the apparent relatively young age of the flows. Testing thermal inertia methods on a variety of martian mantled volcanic surfaces is critical for determining the regional volcanic history and composition. Success of these processes on Mars should be possible considering its success at North Coulee, and could allow for approximate identification of underlying rock properties.

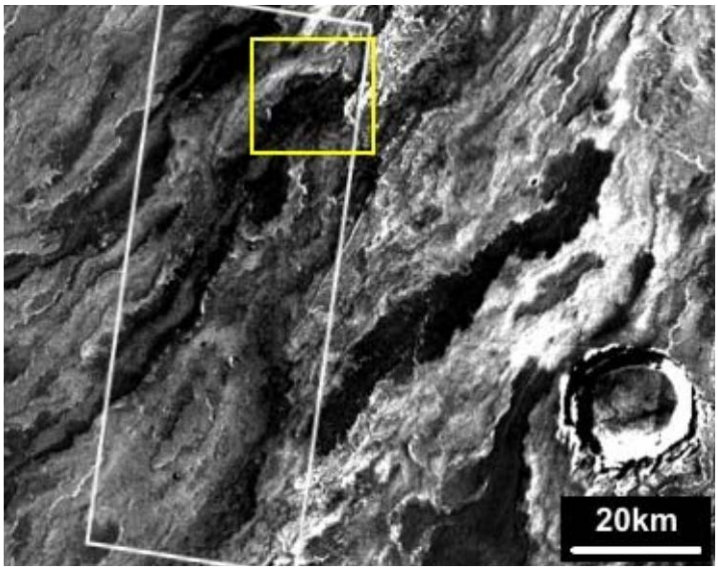

Figure 35: THEMIS (Thermal Emission Imaging System) daytime infrared mosaic of the southern Arsia Mons flow field (centered at 121.65° W, 22.2° S) from Ramsey and Crown (2011). The yellow box denotes the area shown in Figure 32 (CTX) and the white box is the area shown in Figure 36.

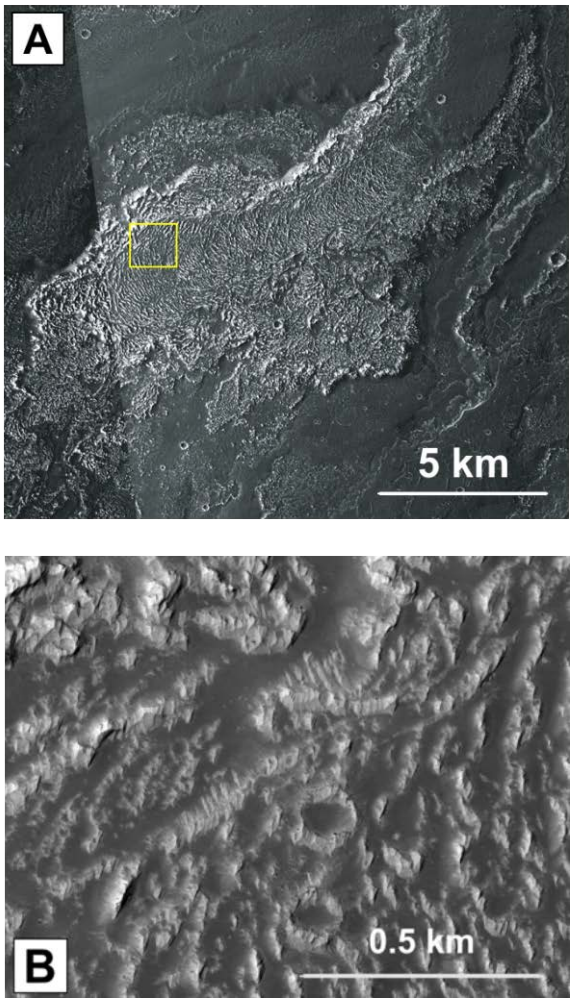

Figure 36: High-resolution images of the Arsia Mons flows (centered at 121.5° W, 22.0° S) from Ramsey and Crown (2011). (A) CTX image mosaic. The yellow box denotes the area shown in (B). (B) HiRISE image (PSP006614_1580), note the levels of mantling. Grain size could be determined after computing ATI.

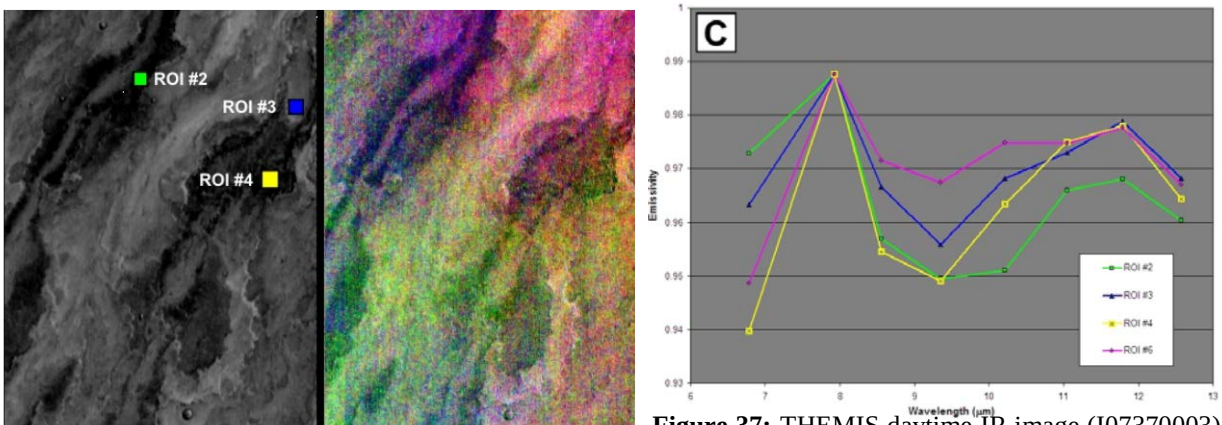

Figure 37: THEMIS daytime IR image (I07370003) of the Arsia Mons flows (121.7° W, 22.3° S) obtained from Ramsey and Crown (2011). **(A)** Brightness temperature image with spectral regions of interest (ROI) shown using the same color codes as the spectra in (C). **(B)** DCS image of IR bands 9,6,4 in R,G,B. Despite being a region of moderate dust cover, spectral variations of the flows are still detected. **(C)** Atmospherically-corrected IR spectra of the ROI's. Note that ROI #2 shows a more basaltic spectral shape, whereas ROI #3 is more similar to the dusty plains flows. ROI #4 is potentially more silicic.

The THEMIS instrument on the Mars Odyssey Orbiter will be used for creation of the thermal inertia data similar to what was done with the ASTER data (Figure 37). THEMIS has ten TIR bands (although only 8 are generally used for surface studies) and five VNIR bands (Christensen et al., 2004). THEMIS band resolution is very similar to ASTER, which would make the ATI images of Mars nearly identical to their Earth-based counterparts. Visible bands on THEMIS provide resolution of 18 meters, while infrared bands have 100-meter resolution. The lack of precipitation, water vapor, and the thin atmosphere could provide even greater accuracy and availability of data compared to Earth-based sites. The lack of precipitation means that the surfaces do not change much over the course of a martian year. Therefore, more accurate data analysis could be possible by averaging several ATI maps together to reduce error and improve overall quality.

5.0 CONCLUSIONS

Initial results utilizing Apparent Thermal Inertia (ATI) to analyze Earth-based particle size appear to be favorable. ATI provides an accurate approximation of particle size in an area, which is useful in identifying areas of fine-grained deposits. Mantled zones appeared to be present in pixels with an ATI value below 0.025. Values above 0.025 at the Mono Craters were associated with larger volcanic blocks. More specific analysis can provide the estimated average grain size of a pixel using the related ATI value. ATI evaluations at North Coulee were able to distinguish average grain size of mantling deposits with only about a centimeter of error. Once extrapolated for size difference ATI assessment of boulder-sized deposits provided similar margins of error. ATI imaging consequently allows for differentiation between different topography by correlating grain/block size with their associated ATI value. This allows for the identification of areas of small-grained accumulations hindering bedrock analysis. This procedure can be valuable in areas of highly variable terrain but similar composition such as the Mono Craters and other volcanic topography. ATI can also prove an asset in hazardous or inaccessible terrain where ground validation is impossible or dangerous. However, pixel mixing can hinder results depending on image resolution, so care should be taken in image analysis. This is especially true with moderate ATI values between 0.023 and 0.027, as heterogeneous terrain can lead to pixel mixing that cannot be ascertained without more detailed ground validation, the use of high-resolution aerial images, or more complex modeling of the emissivity spectra and spatial resolution. Extreme ATI

values proved to be more homogenous and the effect of pixel mixing on these zones is minor. Shadows in the daytime ASTER image also resulted in anomalously high ATI values what would usually be found in an area. However these shadows were concentrated on the western edges of the flow fronts and were not detrimental to this goals of this specific study. Sub-pixel shadowing however can be a concern by artificially raising ATI values. In future ATI studies a digital elevation model (DEM) and possibly radar data could be used during the ATI analysis to reduce these errors. Scaling factors should also be included in the ATI equation to account for variations in solar flux with latitude and solar declination.

Lab evaluation of field samples clarified the composition of the Mono Craters, specifically North Coulee. While all high silica rhyolite, point count measurements supported field-based findings that North Coulee consisted of approximately 75% course vesicular pumice and 25% obsidian. The vast amount of CVP present specified that the vesicularity in the area was very high, which would slightly affect emissivity readings. As a result of this compositional homogeneity, ATI and emissivity spectra did not correlate because of the uniformity of composition and the high vesicularity of the Mono Craters. This makes the interpretation of ATI simpler since compositional/spectral effects did not have to be considered. This was one of the primary reasons this field site was selected.

Evaluation of 24-hour results from the thermal inertia camera helped to clarify the relation between thermal inertia and grain size. While the large thermal inertia difference between larger boulders and mantling deposits is accepted, the 24-hour study revealed minor thermal inertia differences between mantling layers of different grain size. These differences in the ground-based temperature data prove that grain size variations can be detected using this approach, which will allow specific ATI-derived block sizes to be validated in the future. For

example, ground-based ATI datasets could be created from the FLIR images and coregistered daytime camera images. These high resolution ATI images could be analyzed for block size distributions and compared to the ATI value for the corresponding pixel in order to further constrain the satellite-based measurements. The addition of albedo along with temperature differentiation in ATI images provides even greater precision in identifying differences between grain size layers by accounting for reflectance and areas of shadow.

The next phase of research will be to use thermal inertia to apply these research techniques to mantled volcanic flows on the martian surface similar to the Mono Crater chain. Two areas have already been chosen: Arsia Mons along with plains to the south and a volcanic plateau crossing Syria Planum. Like the Mono Craters these zones have variable mantling cover over young volcanic deposits. The two areas are similar but provide different volcanic depositional styles (shield volcano versus volcanic plains) and thermal inertia will be used to decouple the effects of the mantling deposits and the underlying lava flows in order to derive the composition and texture of those flows. Thermal inertia on Mars will be more accurate considering the thin martian atmosphere and the lack of cloud cover, atmospheric water vapor, and precipitation. Using space-based imaging for martian bedrock identification, and to a lesser extent grain size approximation, is useful for a variety of reasons. The unavailability of ground validation on Mars (excluding rover sites) requires accurate satellite reconnaissance to allow for a thorough understanding of surface properties. The identification of eolian deposits, derivation of their grain size, and separation from the underlying rocks provides greater insight to the volcanic history and weathering of these regions. The success of future research at Arsia Mons and Syria Planum would provide a useful addition to martian remote sensing and a greater understanding of the planet’s surface properties.

APPENDIX A

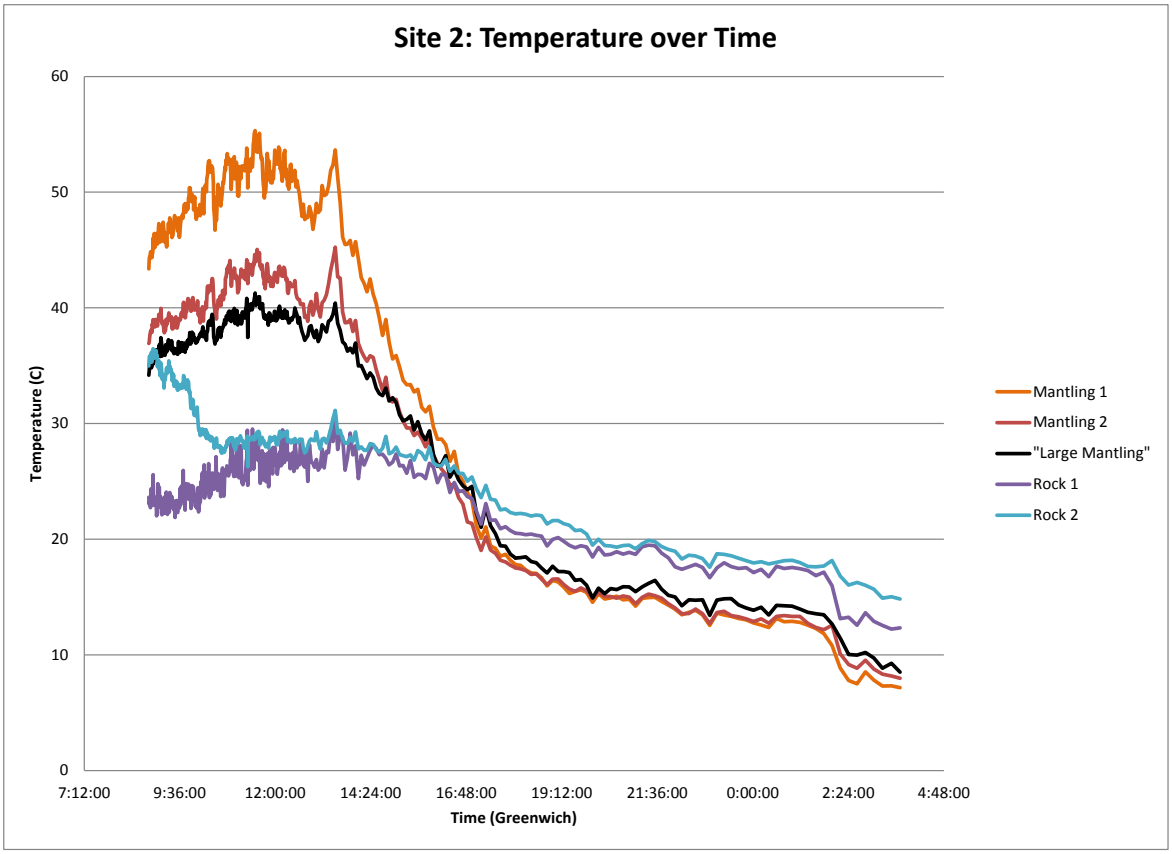

Figure 38: Data obtained from the FLIR camera showing temperature over a 17-hour period. The camera malfunctioned during the night, so the morning temperatures were not recorded.

Figure 39: A photo of the site analyzed with an infrared camera, Data shown in Figure 38.

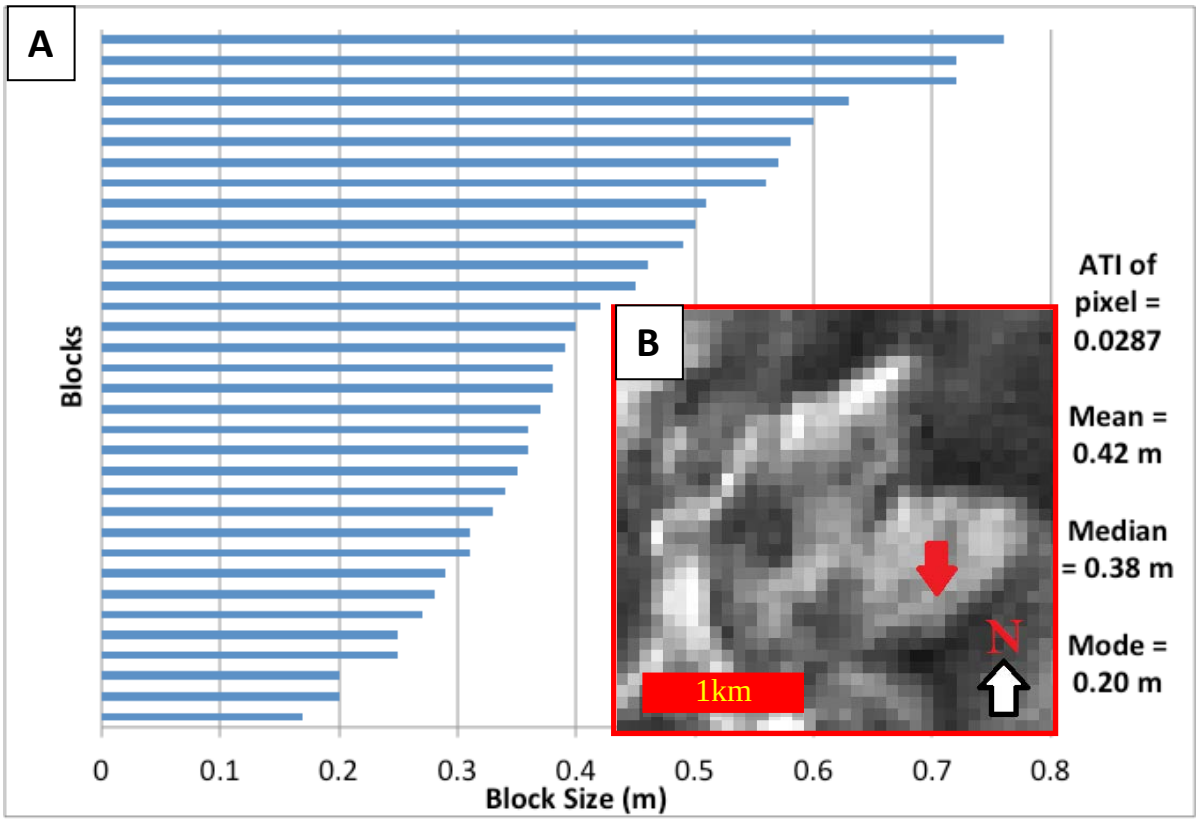

Figure 40: A) Histogram of fragment size of one ASTER pixel. B) Location of pixel on North Coulee (red arrow).

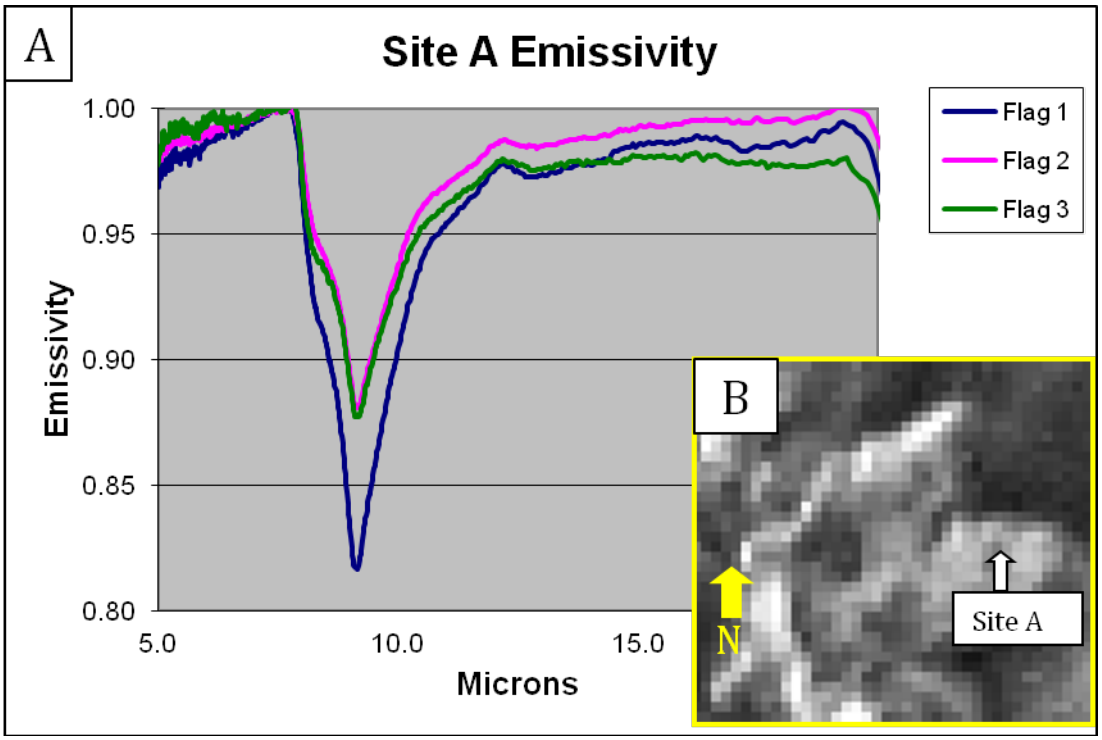

Figure 41: Laboratory TIR emissivity spectra of three samples taken from "Site A" on top of North Coulee (A). The location of the site is listed in "B".

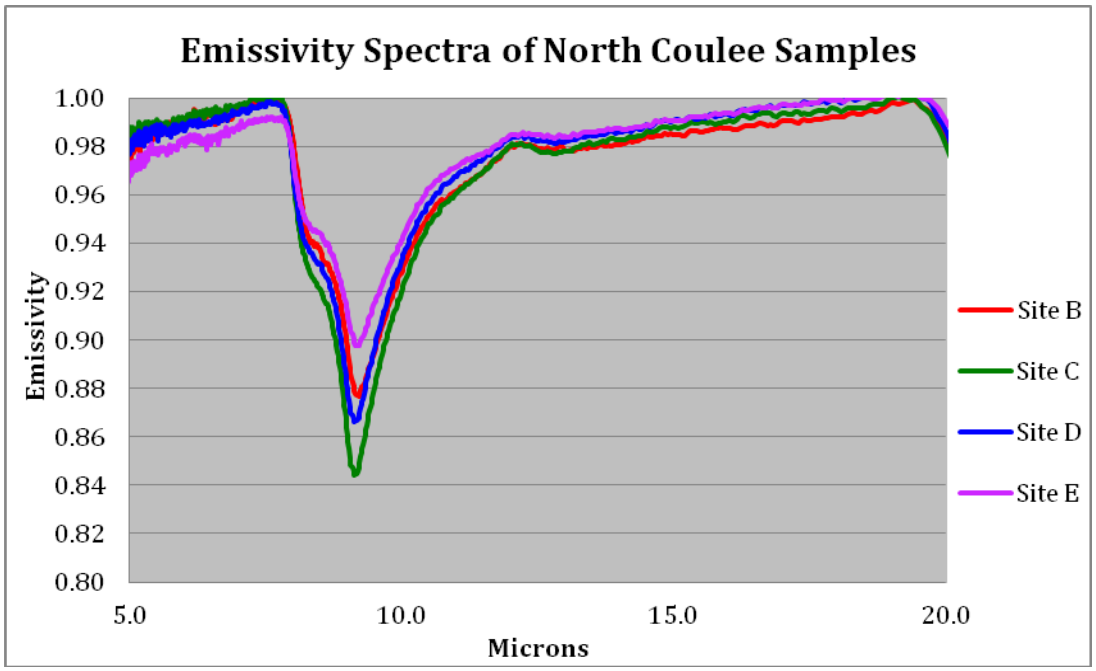

Figure 42: Laboratory TIR emissivity spectra of samples taken at multiple North Coulee sites.

APPENDIX B

Mono Crater Field Work Notes

July 13th – July 17th 2012
Mark A. Price & Anna Downey

Site 12

- Friday 11:15am
- The side of a hill
- About a dozen Ponderosa pine trees surround site
- ASTER photos show low thermal inertia in area
    - 70% mantling, 30% boulders
        - Mantling appears to be sand-sized grains mixed with gravel-sized grains
        - Trace amounts of Obsidian
        - Boulders = rhyolitic pumice
        - Average boulder size = 1/3 m
        - Largest boulder at site = 1m by .5m by .6m (Length by Width by Height)
        - Abnormally large boulders:
            - 1m, .95m, .8m, .8m, .7m, .7m, .7m, .6m, .6m
            - AVG abnormal = .76m
- Dead pine needles cover the surface in many areas

5 sample sites:

Site 12 Flag 1 11:20am

- Mantling depth: about 6-8 cm (measured in 5 different spots)
- Grain Size: ranges from about 1-2mm at finest to 14-20cm at coarsest
- Cobbles randomly assorted, angular, fragmented
- Vesicular pumice, rhyolitic, light rocks
- Distribution: about 20-30% coarse to 70-80% fines

Site 12 Flag 2

- Mantling depth: about 10-17 cm
- Grain Size: smallest fines about 1-5mm, largest around 60mm
- More mantled here, larger cobbles found mostly above/around fines
- Rocks have layers of pumice/obsidian. Vesicles in pumice have been flattened.
- Dominant colors are gray/orange. Pine needles scattered, but not abundant. Moss growing on several larger rocks (dark brown to green moss)
- Distribution: about 40% fines, 60% rocks (coarse)

Site 12 Flag 3

- Mantling depth: none (100% rock, very little fines found only in rock spaces)
- Grain Size: 3-40cm, average closer to 15cm
- Rhyolitic, slight obsidian, traces of obsidian ribbon in rock. Angular clasts with minimal weathering.
- Scattered needles, 5-6 pinecones in area
- Grain size decreases as you look up the site.

Site 12 Flag 4 (wet after rainstorm)

- Mantling depth: 32 parts of a meter + 10 cm (42cm)
- Grain Size: smallest fines about 2-4mm, largest rocks about 10-14mm
- Rhyolitic pumice, some vesicular, light tan/gray/pink in color, angular, randomly assorted. Area heavily mantled.
- Distribution: about 75% fine, 25% coarser rocks

Site 12 Flag 5 (wet after rainstorm)

- Mantling depth: about 1/3 meter (loose hillslope made accurate measurements undeterminable)
- Grain Size: small pebble to sand size
- Angular clasts, randomly assorted. Large boulders found stuck further up the hillslope. Chunks of obsidian found in area, although sparse. Rocks are rhyolitic, various colors. Rocks not stable, apparent landslide area.
- Pine needles scattered with small (1-4m) trees growing on slope.
- Distribution: 50% pebbles to 50% sand. Not well mixed. Mostly found in their own separate areas on slope

First boulder measurement area – NE North Coulee (Figure 27)
Boulder sizes (in meters):

- 0.36
- 0.37
- 0.29
- 0.27
- 0.39
- 0.20
- 0.35
- 0.45
- 0.51
- 0.72
- 0.36
- 0.58
- 0.63
- 0.38
- 0.33
- 0.60

- 0.34
- 0.57
- 0.31
- 0.56
- 0.31
- 0.40
- 0.50
- 0.20
- 0.72
- 0.46
- 0.25
- 0.28
- 0.38
- 0.17
- 0.25
- 0.49
- 0.76
- 0.42

Site A

- Friday 2:45pm
- Half a dozen Ponderosa pine trees in part of the site
    - Pinecones and needles also common
- ASTER photos show low thermal inertia in area
    - Average grain size at site = 1cm
        - Gravelly texture
    - Rhyolitic pumice mostly, with trace obsidian
    - Some larger rocks present
    - Abnormally large boulders:
        - 1.05m, .82m, .64m, .58m, .45m, .40m, .36m, .34m, .33m, .32m, .28m, .28m, .27m, .27m, .25m, .25m
        - AVG abnormal = .43m

3 sample sites:

Site A Flag 1 2:45pm

- Mantling depth: about 14cm
- Grain Size: 1-5mm at finest (coarse to medium sand), 6-20cm at largest (pebbles and cobbles).
- Red tinted rhyolitic pumice, vesicles very flattened. Some gray/white/pink and ribbon obsidian found in rocks. Not well sorted, randomly arranged.
- Small shrubs (about 3-5in tall) growing sporadically in area.

Site A Flag 2

- Mantling depth: 25-28cm
- Grain Size: medium sand matrix mixed with pebbles (about 3 cm)
- Almost all gray/white rock. Mostly pumice with more vesicles apparent here. Traces of obsidian mixed in rock. Angular particles, not well sorted. No rust here unlike at flag 1 (about 20m away).
- Pine needles around but not on area of interest.

Site A Flag 3

- Mantling depth: about ½ meter
- Grain Size: anywhere between 2mm-2cm, larger particles range from 15-20cm.

- Southeast part of dome, North Coulee
  - Cliffs and pumice plane bordering southeast dome also
- Saturday, July 14

Site B

- 10:15am
- Southeast of dome on pumice plane, near path up to dome top
- Some patches of grass, few trees on edge of site
  - Some areas of moss
- Very fine sand grains, some 1cm gravel grains
- Half a dozen small boulders (rhyolitic pumice)
- Site could have formed from remnants of crater formation, or erosion of dome

Trenching Site/Analysis

- Mantling depth: about 16cm
- GS: average between 1-3cm, coarse sand to pebble sized grains
- Mixture of light and dark rocks, divided about 20% Dark/80% light. Mixture of pumice, obsidian, and other dome rocks (darker). This was an area of coarser material, the walk from the car to here went coarse to fine and then back to coarse here.

PIXEL SURVEY – Near Site B

UTM for each corner:
NW: 324384, 4195636
SW: 324384, 4195546
NE: 324474, 4195636
SE: 324474, 4195546

Thermocouple	Elevation	Surface T	Subsurface T	Depth
NE	2146 m	37.7 °C	21.4 °C	8 cm
SE	2154	38.1	17.7	8
SW	2163	39.2	17.4	8
NW	2156	39.0	16.8	8

Pixel Survey (Price)

- All sites observed vegetation

1) Very fine grains, sand-sized. Mostly rhyolitic pumice, some obsidian
2) ¼ cm large sand grains, trace darker rocks (probably obsidian), mostly pumice
3) ¼ cm large sand grains, 100% pumice.
4) ¼ cm large sand grains, pumice, trace (5%) dark rock (obsidian) that's ½ cm
5) 25% 1 cm gravel, rest ½ cm course sand, 100% pumice
6) <.25 cm fine grain sand, 90% light pumice, 10% dark rock (obsidian)
7) ½ cm sand, 80% light pumice, 20% dark rock (obsidian)
8) ½ cm sand, 90% light pumice, 10% obsidian
9) ½ cm sand, 90% light pumice, 10% obsidian
10) Poorly sorted course and fine sand. Course = 1cm, fine = ¼ cm. 80% light pumice, 20% dark obsidian
11) Fine grained ≤.25 cm sand, 90% light pumice, 10% dark rock obsidian
12) ½ cm sand, 75% pumice 25% obsidian
13) Fine grained ≤.25 cm sand, 90% pumice, 10% obsidian
14) Poorly sorted course and fine sand. Course = .5 cm, fine = ≤¼ cm. 80% pumice, 20% obsidian
15) Fine grained ≤.25 cm sand, 90% pumice, 10% obsidian.
16) Poorly sorted course and fine sand. Course = .5 cm, fine = ≤¼ cm. 90% pumice 10% obsidian.
17) Poorly sorted course and fine sand. Course = .5 cm, fine = ≤¼ cm. 90% pumice 10% obsidian.
18) Poorly sorted course and fine sand. Course = .5 cm, fine = ≤¼ cm. 90% pumice 10% obsidian.
19) Fine grained ≤.25 cm sand. 95% pumice, 5% obsidian.
20) Fine grained ≤.25 cm sand. 100% pumice.
21) 75% course sand 25% fine sand. Course = .5 cm, fine = ≤¼ cm. 90% pumice 10% obsidian.
22) Poorly sorted course and fine sand. Course = .5 cm, fine = ≤¼ cm. 90% pumice 10% obsidian.

23) Course grained ½ cm sand. 70% pumice 30% obsidian.
24) Poorly sorted course and fine sand. Course = .5 cm, fine = ≤¼ cm. 95% pumice 5% obsidian.
25) Fine grained ≤.25 cm sand. 90% pumice, 10% obsidian.
26) Course grained ½ cm sand. 90% pumice 10% obsidian.
27) Course grained ½ cm sand. 70% pumice 30% obsidian.
28) Poorly sorted course and fine sand. Course = .5 cm, fine = ≤¼ cm. 80% pumice 20% obsidian.
29) Course grained ½ cm sand. 80% pumice 20% obsidian.
30) Poorly sorted course and fine sand. Course = .5 cm, fine = ≤¼ cm. 75% pumice 25% obsidian.
31) Poorly sorted course and fine sand. Course = .5 cm, fine = ≤¼ cm. 70% pumice 30% obsidian.
32) Course grained ½ cm sand. 75% pumice 25% obsidian.
33) Poorly sorted course and fine sand. Course = .5 cm, fine = ≤¼ cm. 70% pumice 30% obsidian.
34) Course grained ½ cm sand. 75% pumice 25% obsidian.
35) Poorly sorted course and fine sand. Course = 1 cm, fine = ≤¼ cm. 90% pumice 10% obsidian.
36) Poorly sorted course and fine sand. Course = 1 cm, fine = ≤¼ cm. 90% pumice 10% obsidian.
37) Poorly sorted course and fine sand. Course = 1 cm, fine = ≤¼ cm. 90% pumice 10% obsidian.
38) Poorly sorted course and fine sand. Course = .5 cm, fine = ≤¼ cm. 90% pumice 10% obsidian.
39) Poorly sorted course and fine sand. Course = .5 cm, fine = ≤¼ cm. 90% pumice 10% obsidian.
40) Poorly sorted course and fine sand. Course = .5 cm, fine = ≤¼ cm. 90% pumice 10% obsidian.
41) Mostly fine (75%) sand, 25% course sand. Course = .5 cm, fine = ≤¼ cm. 85% pumice 15% obsidian.
42) Course grained ½ cm sand. 90% pumice 10% obsidian.
43) Course grained ½ cm sand. 90% pumice 10% obsidian.
44) Poorly sorted course and fine sand. Course = .5 cm, fine = ≤¼ cm. 90% pumice 10% obsidian.
45) Poorly sorted course and fine sand. Course = .5 cm, fine = ≤¼ cm. 85% pumice 5% obsidian.
46) Course grained ½ cm sand. 75% pumice 25% obsidian.
47) Poorly sorted course and fine sand. Course = .5 cm, fine = ≤¼ cm. 75% pumice 25% obsidian.
48) Course grained ½ cm sand. 70% pumice 30% obsidian.
49) Poorly sorted course and fine sand. Course = .5 cm, fine = ≤¼ cm. 70% pumice 30% obsidian.
50) Course grained 1 cm sand (75%), 25% 2 cm gravel. 70% pumice 30% obsidian.
51) Course grained 1 cm sand. 70% pumice 30% obsidian.
52) Course grained ½-1 cm sand mix. 70% pumice 30% obsidian.

53) Poorly sorted course and fine sand. Course = .5 cm, fine = ≤¼ cm. 75% pumice 25% obsidian.
54) Poorly sorted course and fine sand. Course = .5 cm, fine = ≤¼ cm. 70% pumice 30% obsidian.
55) Poorly sorted course and fine sand. Course = .5 cm, fine = ≤¼ cm. 90% pumice 10% obsidian.
56) Poorly sorted course and fine sand. Course = 1 cm, fine = ≤¼ cm. 90% pumice 10% obsidian.
57) Fine grained ≤¼ cm sand. 90% pumice, 10% obsidian.
58) 75% 1cm course sand, 25% ≤¼ cm sand, 90% pumice, 10% obsidian.
59) Poorly sorted course and fine sand. Course = 1-½ cm, fine = ≤¼ cm. 90% pumice 10% obsidian.
60) Poorly sorted course and fine sand. Course = .5 cm, fine = ≤¼ cm. 80% pumice 20% obsidian.
61) Poorly sorted course and fine sand. Course = .5 cm, fine = ≤¼ cm. 90% pumice 10% obsidian.
62) Fine grained ≤¼ cm sand. 95% pumice, 5% obsidian.
63) Fine grained ≤¼ cm sand. 95% pumice, 5% obsidian.
64) Fine grained ≤¼ cm sand (75%), and 25% ½ cm sand. 95% pumice, 5% obsidian.
65) Poorly sorted course and fine sand. Course = .5 cm, fine = ≤¼ cm. 85% pumice 15% obsidian.
66) Poorly sorted course and fine sand. Course = .5 cm, fine = ≤¼ cm. 85% pumice 15% obsidian.
67) Poorly sorted course and fine sand. Course = 1-.5 cm, fine = ≤¼ cm. 90% pumice 10% obsidian.
68) Poorly sorted course and fine sand. Course = .5 cm, fine = ≤¼ cm. 90% pumice 10% obsidian.
69) Poorly sorted course and fine sand. Course = .5 cm, fine = ≤¼ cm. 80% pumice 20% obsidian.
70) Poorly sorted course obsidian and fine pumice sand. Course obsidian = 1 cm, fine pumice = ≤¼ cm. 90% pumice 10% obsidian.
71) Poorly sorted course and fine sand. Course = 1-.5 cm, fine = ≤¼ cm. 75% pumice 25% obsidian.
72) Poorly sorted course and fine sand. Course = .5 cm, fine = ≤¼ cm. 80% pumice 20% obsidian.
73) Poorly sorted course and fine sand. Course = .5 cm, fine = ≤¼ cm. 80% pumice 20% obsidian.
74) Fine grained ≤¼ cm sand. 90% pumice, 10% obsidian.
75) Poorly sorted course obsidian and fine pumice sand. Course obsidian = 1 cm, fine pumice = ≤¼ cm. 80% pumice 20% obsidian.
76) Poorly sorted course and fine sand. Course = .5 cm, fine = ≤¼ cm. 90% pumice 10% obsidian.
77) Poorly sorted course and fine sand. Course = .5 cm, fine = ≤¼ cm. 85% pumice 15% obsidian.
78) Poorly sorted course and fine sand. Course = .5 cm, fine = ≤¼ cm. 80% pumice 20% obsidian.

79) Poorly sorted course and fine sand. Course = 1-.5 cm, fine = ≤¼ cm. 80% pumice 20% obsidian.
80) Course grained ½ cm sand. 80% pumice 20% obsidian.
81) Course grained ½ cm sand. 80% pumice 20% obsidian.
82) Poorly sorted course and fine sand. Course = .5 cm, fine = ≤¼ cm. 70% pumice 30% obsidian.
83) Poorly sorted course and fine sand. Course = .5 cm, fine = ≤¼ cm. 75% pumice 25% obsidian.
84) Course grained ½ cm sand. 75% pumice 25% obsidian.
85) Course grained ½ cm sand. 75% pumice 25% obsidian.
86) Course grained ½ cm sand. 70% pumice 30% obsidian.
87) Poorly sorted course and fine sand. Course = .5 cm, fine = ≤¼ cm. 80% pumice 20% obsidian.

Pixel Survey (Downey)

1) Mostly light rock, 90% Light 10% dark, very few obsidian traces, chunks of pumice, semi-angular to rounded, fines are fine sand to medium sized, grain size about 1-3 cm
2) More coarse-grained clasts, 85% light /15% dark, more angular, flattened pumice, Grain Size 1-4 cm. Fines are FS to MS sized. Darks mostly dome rocks
3) Medium sand with fine sand. Mostly light, dark grains were mostly dome rocks. Here slightly less coarse than last step (#2). Grain size about 0.5-2 cm. Distribution about 85% light /15% dark.
4) Medium sand with fine sand. 20% dark /80% Light. Dark dome rocks with light pumice. Pumice here is slightly less angular. Grain Size averaging 1-2 cm
5) Coarse/medium sandy area. Medium to course sand. Grain size around 1-2 cm, irregular clasts about 3 cm. Distribution about 10% Dark / 90% Light. The dark rocks are dome rocks. Very sparse vegetation (1 small plant)
6) Fine Sand to Medium Sand. Slightly less coarse here. Pumice fragments are more angular. 15% Dark /85% Light. Grain Size is 1-3 cm and smaller (finer area)
7) Coarse area. Greater mix of light and dark. Sparse obsidian fragments. Less angular particles. 15% Dark /85% Light. Distributed about 50/50 for Course/Fine. Grain Size around 2-3 cm. Few small plants in area.
8) 60% Course 40% Fine. 3-4 traces of obsidian, but still sparse. Mostly semi-angular pumice. Grain Size around 1 - 3.5 cm. Medium Sand fines. Scattered pine needles, sparse. 15% Dark 85% Light
9) Slightly less coarse area. 20% Dark 80% Light. Grain Size about 1-2 cm. 65% fine 35% course. Pumice is more rounded mixed with darker dome rocks. Medium Sand fines
10) Small pine tree growing in area. Other small plants scattered about. 50/50 course/fine. flatter pumice. Fine Sand to Medium Sand fines. Grain Size 1.5 to 3 cm. All dark rocks are dome rocks.
11) Semi-rounded particles, no obsidian. 60/40 Light/Dark. Less coarse area. 70/30 Fine/Course. Grain Size 0.5-2 cm. More vegetation, slightly larger plants seen here.
12) 60/40 Course/Fine. Coarse area, with Grain Size about 1-3 (sometimes 4) cm. Small shrubs/pines nearby. Semi-angular grains. 90% Light 10% Dark

13) 60% Light 40% Dark. Clasts more angular. 3 small shrubs nearby. Medium Sand to Course Sand fines. Grain Size about 2-3 cm
14) 50% Light 50% dark. Clasts semi-angular, no obsidian. Fine Sand to Medium Sand fines. Coarser area. 65% course 35% Fine. Grain Size around 1 - 2.5 cm.
15) 35% Dark 65% Light. 50/50 Course/Fine. Finer sand. Small shrubs. Grain Size about 2 cm. 90% Light 10% Dark
16) Small shrubs, finer area, angular clasts. Medium Sand sized fines. 90% Light 10% Dark. Grain Size about 2 cm
17) Shrubs, pieces of wood evident. Obsidian fragments more abundant here. 40% Dark 60% Light. Grain Size about 0.5-2 cm
18) Now at bottom of small hillslope. Vegetation increasing. 30% course 70% fine. Medium Sand to Fine Sand. Grain Size is 1-2 cm. 15% Dark 85% Light.
19) Harder ground on slope. Multiple shrubs. Grain Size 1.5 cm or less. Medium Sand particles. 95% Light, 5% Dark
20) Shrubs here. Grain Size mostly equal to or less than 1cm. Rounded particles. 95% Light 5% Dark
21) Grain Size equal or less than 1cm. Almost all pumice here. Shrubs more abundant, about 1 foot apart from each other or less. About 98% pumice with few scattered dark particles
22) Mostly all fines. Grain Size less than or equal to 1cm. Close shrubs. Rounded clasts. Two small obsidian pieces seen.
23) Shrubs. Grain Size less than or equal to 1 cm. Few more dark particles here than before, still around 98% pumice.
24) Larger shrubs, some with flowers. Slightly coarser area. Grain Size of rounded clasts about 1 - 1.5cm, 2 is large. Most grains still 1cm or less.
25) Larger shrubs, same size grains as last step, slope mostly a uniform area. Rounded clasts, equal or less that 1cm or between 1-2 cm. More on larger side. Still mostly pumice
26) Slammer shrubs. Coarse area but like previous step very uniform. Fine Sand to Medium Sand fines. 97% pumice. Pumice particles larger than 2 cm sparse.
27) Small shrubs but close together. Less uniform, coarse grains. 90% Light 10% Dark. Semi-angular. 5% course 95% fine.
28) Close shrubs. Semi-angular pieces. Grain Size about 0.5 to 2 cm. Coarser area. Now, starting down slope. 10% Dark 90% Light.
29) Shrubs here. Slightly more dark, but not by much. 10% Dark 90% Light Fine Sand mantling. 95% Light 5% Dark.
30) Slightly finer here, less uniformity, coarser particles and finer ones more separated. Dark particles much smaller than light ones. Fine Sand to Medium Sand grains.
31) More uniformity. 90% Light 10% Dark. Shrubs smaller. Grain Size mostly less or equal to 1 cm. Finer area, Fine Sand mantling
32) 30% Dark 70% Light. All grains about same size. Slightly coarser area. Grain Size about 1 - 1.5 cm. Fine Sand.
33) Smaller shrubs, slightly sparser area. 15% Dark 85% Light. Semi-angular clasts. Medium sand.
34) Grains uniformly about 1 - 1.5 cm. Medium Sand. 5% Dark 95% Light.
35) Less vegetation here. Larger clasts, about 2-3 cm, although most are around 1-2 cm. Medium Sand, 95% light particles.

36) Most grains again about 1-2 cm. 95% light colored, small shrubs nearby.
37) Medium Sand, Grain Size about 0.5-1cm. 10% Dark 90% Light. Traces of obsidian.
38) Vegetation here slightly more coarse. Large grains about 2 cm, most grains are rounded. 90% Light 10% Dark
39) Semi-rounded grains, with vegetation. Grain Size about 0.5 to 1cm for average, 95% Light 5% Dark
40) Most grains again about 1-2 cm. 95% light colored, small shrubs nearby.
41) Coarser grains averaging about 3cm, finer around 0.5-2cm. Less uniform area, semi-angular particles. 90% Light 10% Dark
42) Grain Size about 0.5 to 1cm. Lots of Fine Sand, some Medium Sand. Area slightly more uniform. Semi-rounded particles.
43) 90% Dark 10% light. Uniform area. Grain Size is 0.5 to 1cm for average, Fine Sand mantling
44) Now larger vegetation. Clasts more scattered. 95% Light 10% Dark. Clasts are semi-angular
45) 90% Light 10% dark. Larger shrubs. Medium Sand. Grain Size 0.5-2cm. Less uniform area
46) More uniform with semi-angular clasts. 95% Light 10% Dark. Small vegetation. Grain Size about 0.5 - 1cm. Fine sand area
47) Shrubs present. 90% Light 10% Dark. Mix of coarse and fine, about 40% course 60% fine. Medium Sand. Grain Size 1-2cm
48) Mostly fines surrounded by shrubs. Grain Size about 0.5 to 1.5cm. Medium Sand.
49) Pinecones among vegetation in area. Mostly uniform fines. Grain Size 0.5 - 1cm and smaller. Sand is Medium to Fine.
50) Still uniform but larger number of coarse grains. Largest from 1-3cm. 95% Light 5% Dark. 80-90% fines here
51) Coarse/fines mix. Average about 1cm. 95% light grains. About 80% fine material
52) Shrubs. One large pumice grain about 4.5 cm. Medium Sand. Grain Size mostly equal or less than 1 cm. Medium Sand to Course Sand
53) Medium Sand and shrubs. 95% Light 10% Dark. Rounded clasts, uniform coarse grains around 1cm or less
54) Same as previous step (#53) however here about 85% fine 15% course
55) More vegetation is closer together, all particles around 0.5 - 1.5cm. About 80% is finer sand
56) Larger vegetation here, more uniform clasts. Clasts range between 1 - 2.5cm. About 60% course 40% fine
57) Semi-rounded clasts, mostly all less than or equal to 1cm, about 95% light rock, shrubs nearby
58) larger shrubs here with uniform grains. 90% light colored rock, Grain Size less than or equal to 1cm, fine sand mantling.
59) Fine Sand to Medium Sand here. Grain Size between 1 - 1.5cm. About 60% fine 40% course with surrounding shrubs. 90% light
60) Pinecones and shrubs. Less uniform here. Clasts are rounded, flatter, and about 1.5cm Grain Size. About 50/50 Course/Fine
61) Vegetation with uniform clasts, 90% Light 10% Dark. Grain Size 1 - 1.5cm or less

62) Vegetation with mostly fines in area. Coarse grains less than or equal to 1cm. 95% light rock
63) Pinecones mixed with vegetation. Finer sand here. Most Grain Size less than or equal to 1cm or 0.5cm. 90% light
64) Same description as above (#63)
65) Slightly coarser in spots. Grain Size about 2cm or less. 90% light. 80% fine 20% course
66) Same description as above (#65)
67) Finer still, most grains under 1cm. About 90% fines, 90% light rock
68) Same description as 64, but about 85% light here (slightly less)
69) Very uniform. About 85% light rock, most grains under 1cm. More rounded, dark dome rocks
70) Fines, all under 1cm

SE Portion of N. Coulee (still Day 2)

Boulder Measuring Walk (meters)

0.39
0.3
0.15
0.34
0.55
0.38
0.63
0.36
0.38
0.30
0.32
0.10
0.12
0.26
0.15
0.09
0.35
0.66
0.31
0.26
0.51
0.17
0.44
0.57
0.35
1.14
0.62
0.48
0.40
0.22
0.09

0.02
0.69
0.42
0.16
0.50
0.20
0.87
0.14
0.34
0.10
0.20
0.79
0.53
0.17
0.19
0.20
0.06
0.45

Second Pass (meters)

0.07
0.21
0.14
0.35
0.30
0.35
0.14
0.09
0.10
0.17
0.25
0.12
0.21
0.15
0.18
0.48
0.19
0.65
0.18
0.38
0.18
0.26
0.54
0.12
0.19

0.02
0.04
0.17
0.40
0.44
0.29
0.26
0.28
0.47
0.88
0.18
0.37
0.21
0.25
0.11
0.10
0.29
0.14
0.22
0.23
0.29
0.15
0.21
0.25
0.25
0.28
0.26
0.35
0.10

7/15/12

Giant boulder survey along base of North Coulee near 1st FLIR setup location

Key

B = breccia

O = obsidian

O/CVP = mix of obsidian and CVP

Site	Boulder #	Size	Type
A	1	6 m	B
A	2	4	B
A	3	3.5	B
B	1	4	B
B	2	5	O
B	3	3	B
C	1	5	B/O
C	2	6.5	B/O
C	3	6.5	B
D	1	10	O/B
D	2	6	B
D	3	6	O with fused obsidian breccia
E	1	4	B
E	2	3	B
E	3	2	O

F	1	3	O/CVP
F	2	3	B
F	3	3.5	O

Temp measurements from top of Western North Coulee at elevation of 2447 m

	Surface	10 cm Depth	6 cm Depth	2 cm Depth
1	31.8	30.3	33.9	35.1
2	31.5	30.5	37.3	36.8
3	29.7	29.4	32.8	32.5
4	30.2	28.6	31.8	30.3
5	34.1	28.6	29.7	30.5

2nd location in small valley filled with windblown fines

46.2	27.2	34.3	37.0

3rd location in adjacent small valley

49.5	25.4	39.2	43.7

Bottom of the Western side of N. Coulee - Pumice Dune (Monday)

- Western slope of North Coulee
- Monday, July 16
- Larger rocks 90% of slope
  - 3< cm large at least
  - Some rocks weathers some not
- Red areas higher up on the slope

- Some fine debris
- Angle of repose *very* high near top of slope (50-60 degrees)
  - Bottom of slope about at 35-45 degree angle
- Most of slope large pumice boulders, 20% obsidian.
- Plants grow in line parallel to ground 2/3 up slope
- Rocks much larger on this side of dune than on dome-ward side of dune (1-3cm avg there)

East Cliff of North Coulee

- Monday, July 16
- Poorly sorted
  - Grains range from meter-sized to sand-sized
- 30% obsidian, rest of cliff rhyolitic pumice
- Evident that landslides are common
- Obsidian outcrops near summit
- Some vegetation in sandier, mantled areas
- Pumice/obsidian mix very common in rocks at site
- About 1 mile south of 1st FLIR site.
- Rocks have very little weathering, if any
- Some reddish areas of rock near summit
- Angle of slope about 40 degrees near bottom
- Mantling in area seems high (besides rock outcrops)

Anna's Analysis: Outlining Lava Flows

- Area is about 80m high.
- Finer grains on slope mixed with scattered larger grains. Grain distribution: **60/40 Fine/Course.** Large dark lava pile-ups near top. Lava must have been very viscous.
- Two roads run across slope, interfering with grain distributions. Large rocks are piled near the bottom. Dark outcrop on top is obsidian below a thin line of breccia. The obsidian has no preferred orientation and has partially slid down the hill.
- Vegetation in the area is sparse. Scattered pines are found near the top of the outcrop. Clasts on the outcrop are angular, fragmented. They are probably not located far from their source area.
- This area has a small amount of breccia boulders, although there is less breccia here than the areas we looked at yesterday. Breccia on this side of the dome is very scattered. When walking the contact, evidence for breccia goes in and out.

FLIR Site 2 (Site H)

- Eastern Slope of North Coulee
- Tuesday, July 17
  - Recording started 8:50am
  - Humidity: 13%
  - Atmospheric Temperature: 24 C

- Observation distance: 25m

Flag 1

- 30% obsidian, 70% volcanic rhyolitic pumice
- Poorly sorted
  - Fine: ½ - 1cm
  - Course: 3 – 12cm
- Mantling: 10cm
- Large 1/3m boulders common around site
- Very angular
- Some pink tinges, but mostly brown & gray.

Flag 2

- Mostly large, gravelly grains
  - Average grain size 6-7cm
- Some small grains – 20% of site
  - Average grain size – 2cm
- Very angular grains
- No mantling, just rockfall
- Gray, black, minute pink areas
- Depth of layer over 10cm

large pumice slope on western side of Mono Domes (Celsius)

Surface	10 cm Depth	6 cm Depth	2 cm Depth
22.5	19.2	17.4	17.2

Giant boulder survey along eastern margin of North Coulee around to east side from FLIR setup location

Key

B = breccia

O = obsidian

O/CVP = mix of obsidian and CVP

Site	Boulder #	Size	Type
M	1	3.5 m	O
M	2	1.6	O/CVP

M	3	2.2	O/CVP
N	1	0.9	B
N	2	2.5	B
N	3	1.7	O/CVP
O	1	3	B
O	2	1.7	B
O	3	3	B
P	1	1.4	O/CVP
P	2	1.6	FVP
P	3	1.1	FVP
Q	1	1.2	FVP
Q	2	1.4	O
Q	3	1.4	O
R	1	1.2	FVP
R	2	0.8	FVP
R	3	1.0	FVP

Flag 3 (Area 1)

- 20% obsidian, 80% rhyolite
- Poorly sorted, 70% fine, 30% course
    - Fine ½ cm – ¼ cm
    - Course – 3cm
- Large 20cm rocks present
- Color – gray, black, some pink
- Very angular grains
- Mantling depth – 16cm, may be more
- Surface temperature: 41.8 C
- 10cm depth: 26.1 C
- 6cm depth: 26.4 C

- 2cm depth: 28.0 C

Area 2

- ½ - 1cm grain size
- Surface Temperature: 49.5 C
- 10cm depth: 20.7 C
- 6cm depth: 21.2 C
- 2cm depth: 28.0 C

Area 3

- 1/8 – ¼ cm grain size
- Not on hill, direct sun angle
- Surface Temperature: 35.7 C
- 10cm depth: 18.2 C
- 6cm depth: 24.4 C
- 2cm depth: 26.8 C

Near FLIR Site 1 (Site F)

- 30m north of FLIR site 1
- Tuesday, July 17 9:40am

Flag 1

- Surface Temperature: 40.6 C
- 10cm depth: 22.5 C
- 6cm depth: 19.6 C
- 2cm depth: 21.8 C
- 30% obsidian, 70% volcanic dense rhyolitic pumice
- Poorly sorted (60% fine and 40% course)
    - Fine sand-sized grains (medium to very fine)
    - Course: 3 – 4 cm
    - Boulders present (1/3 m)
- Mantling: 15 cm
- Angular grains
- Gray, black color

Flag 2

- Surface temperature: 41.6 C
- 10cm depth: 23.7 C
- 6cm depth 24.6 C
- 2cm depth 31.8 C
- Mostly course (75%, 2-3 cm), some fine (25%, sand-sized grains)
- Angular grains

- Gray, black, some pink color
- 15% obsidian, 85% volcanic rhyolitic pumice

FLIR Site 1 (Site G)

Flag 1

- Tuesday July 17, 10:00am
- Surface Temperature: 32.6 C
- 10cm depth: 17.6 C
- 6cm depth: 28.1 C
- 2cm depth: 27.4 C
- Angular grains
    - Very course (4cm average, as high as 12cm)
- 20% obsidian, 80% CVP (course vesicular pumice)
    - Gray, black, some pink
- 40 degree angle slope
- Depth – 10cm

SW North Coulee – Old Dome (Very Mantled)

Flag 1

- Tuesday July 17, 11:45am
- Surface Temperature: 56.6 C
- 10cm depth: 14.0 C
- 6cm depth: 17.2 C
- 2cm depth: 31.6 C
- Uniform sorting (20 < mm very fine)
    - 90% pumice, 10% obsidian
    - Mostly gray, small amount of black in color
- Depth – 40 cm mantling

Flag 2

- Surface Temperature: 59.7 C
- 10cm depth: 18.9 C
- 6cm depth: 24.1 C
- 2cm depth: 33.0 C
- Well-sorted, but bigger (1cm) grains account for 30% (rest fine sand)
    - 80% pumice 20% obsidian
- Mantling 20-25 cm
- Mostly gray, some black color

Flag 3

- Surface Temperature: 52.8 C

- 10cm depth: 16.3 C
- 6cm depth: 19.3 C
- 2cm depth: 29.5 C
- Course (50% 1-2cm) and fine (<1/2 cm)
    - A few rocks (6< cm)
    - Gray with some black color
- Mantling depth 30< cm

Flag 4

- Surface Temperature: 58.4 C
- 10cm depth: 31.2 C
- 6cm depth: 34.0 C
- 2cm depth: 41.5 C
- Mantling 30< cm
- Average grain size: ½ - 1cm
- Layer on top is courser than below layers
- Mostly uniform and well-sorted

Flag 5

- Surface Temperature: 51.1 C
- 10cm depth: 33.6 C
- 6cm depth: 33.6 C
- 2cm depth: 41.1 C
- Mantling 25cm
- Average Grain size 1cm
- Moderated well-sorted
- 90% uniform with some larger clasts (1.5 – 3.5cm) scattered about
- Mostly pumice
    - Some larger clasts are obsidian

BIBLIOGRAPHY

Abrams, M., B. Bailey, H. Tsu, and M. Hato (2010), The ASTER Global DEM, Photogram. *Eng. Rem. Sens., 76*, 344-348.

Achauer, U., L. Greene, J. R. Evans, & H. M. Iyer (1986), Nature of the Magma Chamber Underlying the Mono Craters Area, Eastern California, as Determined From Teleseismic Travel Time Residuals. *Journal of Geophysical Research 91.B14* pp. 13873-3891

Anderson, S.W., E. R. Stofan, J. J. Plaut, and D. A. Crown (1998), Block size distributions on silicic lava flow surfaces: Implications for emplacement conditions, Geol. Soc. Am. Bull. 110, 1258-1267.

Bailey, R. A. (1982), Other Potential Eruption Centers in California: Long Valley-Mono Lake, Coso, and Clear Lake Volcanic Fields. *Calif. Div. Mines Geol. Spec. Publ. 63* pp. 17-28.

Bailey, R. A. (1989), Quaternary Volcanism of Long Valley Caldera and Mono-Inyo Craters, Eastern California. *Field Trip Guidebook T313. American Geophysical Union, Washington, DC.*

Bailey, R.A. (1989), Geologic map of Long Valley caldera, Mono-Inyo Craters volcanic chain, and vicinity, eastern California. *U.S. Geol. Surv. Map* I-1933, scale 1:62,500; pamphlet.

Bailey, R. A., G. B. Dalrymple, & M. A. Lanphere (1976), Volcanism, Structure, and Geochronology of Long Valley Caldera, Mono County, California. *Journal of Geophysical Research* 81.5 pp. 725-44.

Bandfield, J. L., and W. C. Feldman (2008), Martian high latitude permafrost depth and surface cover thermal inertia distributions. *Journal of Geophysical Research: Planets (1991–2012) 113, no. E8*.

Bing Maps – Mono Craters, California. *ArcGIS 10, ESRI.* Accessed 2013.

Bleacher, J.E., R. Greeley, D.A. Williams, S.R. Cave & G. Neukum (2007), Trends in effusive style at the Tharsis Montes, Mars, and implications for the development of the Tharsis province, *J. Geophys. Res., 112,* E09005, doi:10.1029/2006JE002873.

Bursik, M., C. Renshaw, J. McCalpin, & M. Berry (2003), A volcanotectonic cascade: Activation of range front faulting and eruptions by dike intrusion, Mono Basin‐Long Valley Caldera, California. *Journal of Geophysical Research: Solid Earth (1978–2012)* 108, no. B8.

Bursik, M., & K. Sieh. "Range Front Faulting and Volcanism in the Mono Basin, Eastern California." *Journal of Geophysical Research* 94.B11 (1989): 15587-5609

Bursik, M., & K. Sieh (2012), Range front faulting and volcanism in the mono basin, eastern California.

Cai, G., Y. Xue, Y. Hu, Y. Wang, J. Guo, Y. Luo, C. Wu, S. Zhong, & S. Qi (2007), Soil moisture retrieval from MODIS data in Northern China Plain using thermal inertia model. *International Journal of Remote Sensing 28.16* pp. 3567-3581.

Carlson, T. N., J. K. Dodd, S. G. Benjamin, and J. N. Cooper (1981), Satellite estimation of the surface energy balance, moisture availability and thermal inertia. *Journal of Applied Meteorology, 20,* pp. 67-87.

Chen, Y., P. E. Smith, N. M. Evensen, D. York, & K. R. Lajoie (1996), The edge of time: dating young volcanic ash layers with the ^{40}Ar–^{39}Ar laser probe. *Science, 274* pp. 1176–1178.

Christensen, P.R. (1982), Martian dust mantling and surface composition: Interpretation of thermophysical properties. *Journal of Geophysical Research, 87,* 9985–9998.

Christensen, P. R., B. M. Jakosky, H. H. Kieffer, M. C. Malin, H. Y. McSween Jr, K. Nealson, ... & M. Ravine (2004), The thermal emission imaging system (THEMIS) for the Mars 2001 Odyssey mission. In *2001 Mars Odyssey* pp. 85-130.

Cracknell, A. P., & Y. Xue (1996a), Thermal inertia determination from space—a tutorial review. *International Journal of Remote Sensing 17.3* pp. 431-461.

Cracknell, A. P. & Y. Xue (1996b), Estimation of ground heat flux using AVHRR data and an advanced thermal inertia model (SoA-TI model). *International Journal of Remote Sensing* 17 pp. 637–642.

Cracknell, A. P., & Y. Xue (1996c), Dynamic aspects study of surface temperature from remotely-sensed data using advanced thermal inertia model. *Remote Sensing 17.13* pp. 2517-2532.

Crumpler, L.S. & J.C. Aubele (1978), Structural evolution of Arsia Mons, Pavonis Mons, and Ascraeus Mons: Tharsis region of Mars. *Icarus, 34,* pp. 496-511.

Crumpler, L. S., J. W. Head, & J. C. Aubele (1996), Calderas on Mars: Characteristics, structure and associated flank deformation, in Volcano Instability on the Earth and Other Planets.

W.J. McGuire, A.P. Jones, and J. Neuberg (eds.), *Geol. Soc. Spec. Publ., 110,* pp. 307-348.

Dalrymple, B. G., A. Cox, and R. R. Doell, & R. Richard (1965), Potassium-Argon Age and Paleomagnetism of the Bishop Tuff, California. *Geological Society of America Bulletin 76.6* pp. 665.

Dixon, T., M. Miller, F. Farina, H. Wang. & D. Johnson (2000), Present-day motion of the Sierra Nevada block and some tectonic implications for the Basin and Range province, North America. *Tectonics 19,* pp. 1–24.

Dohm, J. M., K. L. Tanaka & T. M. Hare (2001), Geologic map of the Thaumasia region, Mars, *U.S. Geol. Surv. Geol. Invest. Ser. Map* I-2650.

Dohm, J. M. & K. L. Tanaka (1999), Geology of the Thaumasia region, Mars: plateau development, valley origins, and magmatic evolution. *Planetary and Space Science, 47,* pp. 411-431.

Edgett, K. S., & N. Lancaster (1993), Volcaniclastic Aeolian Dunes: Terrestrial Examples and Application to Martian Sands. *Journal of Arid Environments 25* pp. 271-97.

Edgett, K. S., and M. C. Malin (2002), Martian sedimentary rock stratigraphy: Outcrops and interbedded craters of northwest Sinus Meridiani and southwest Arabia Terra. *Geophysical Research Letters 29, no. 24* pp. 32-1.

Fenton, L. K., & J. L. Bandfield (2003), Aeolian Processes in Proctor Crater on Mars: Sedimentary History as Analyzed from Multiple Data Sets. *Journal of Geophysical Research 108.E12*, n. pag.

Gilbert, C. M. (1938), Welded Tuff in Eastern California. *Geol. Soc. Amer. Bull. 49* pp. 1829-1862.

Gillespie, A., S. Rokugawa, T. Matsunaga, J. S. Cothern, S. Hook, and A. B. Kahle (1998), A temperature and emissivity separation algorithm for Advanced Spaceborne Thermal Emission and Reflection Radiometer (ASTER) images. *Geoscience and Remote Sensing, IEEE Transactions on 36, no. 4* pp. 1113-1126.

Google Earth, *37°53'42.34"N, 119° 0'16.07"W.* July 11, 2011.

Greeley, R. (1982), The Snake River Plain, Idaho: Representative of a new category of volcanism. *J. Geophys. Res., 87(B4),* pp. 2705–2712.

Hardgrove, C., J. Moersch, & S. Whisner (2009), Thermal Imaging of Alluvial Fans: A New Technique for Remote Classification of Sedimentary Features. *Earth and Planetary Science Letters 285* pp. 124-30.

Head, J.W., N. Siebert, S. Pratt, D. Smith, M. Zuber, S. Solomon, P.J. McGovern, J.B. Garvin, & the MOLA Science Team (1998a), Characterization of major volcanic edifices on Mars

using Mars Orbiter Laser Altimeter (MOLA) data. *Lunar Planet. Sci. Conf., XXIX, abs. 1322.*

Head, J.W., N. Siebert, S. Pratt, D. Smith, M. Zuber, J.B. Garvin, P.J. McGovern, & the MOLA Science Team (1998b), Volcanic calderas on Mars: Initial views using Mars Orbiter Laser Altimeter (MOLA) data. *Lunar Planet. Sci. Conf., XXIX, abs. 1488*.

Hellman, M. J., and M. S. Ramsey (2004), Analysis of hot springs and associated deposits in Yellowstone National Park using ASTER and AVIRIS remote sensing. *Journal of Volcanology and Geothermal Research 135.1* pp. 195-219.

Hildreth, W. (1979), The Bishop Tuff: evidence for the origin of compositional zonation in silicic magma chambers. C.E. Chapin, W.E. Elston (Eds.), Ash-Flow Tuffs, *Geol. Soc. Am. Spec. Pap., 180* pp. 43–75

Hildreth, W. & G. A. Mahood (1986), Ring-fracture eruption of the Bishop Tuff. *Geol. Soc. Am. Bull., 97* pp. 396–403

Hildreth, W. (2004), Volcanological Perspectives on Long Valley, Mammoth Mountain, and Mono Craters: Several Contiguous but Discrete Systems. *Journal of Volcanology and Geothermal Research 136.3-4* pp. 169-98.

Hill, D. P. (2002), Response plan for volcano hazards in the Long Valley caldera and Mono Craters region, California. *Vol. 2185. Geological Survey (USGS).*

Hill, D. P. (2006), Unrest in Long Valley Caldera, California, 1978–2004. *Geological Society, London, Special Publications, 269(1),* pp. 1-24.

Hughes, C. G. & M. S. Ramsey (2013), A Radiometrically-Accurate Super-Resolution Approach to Thermal Infrared Image Data. *Int'l J. Image Data Fusion, doi: 10.1080/19479832.2012.711377.*

Hunt, G. R. (1980), Electromagnetic radiation: The communication link in remote sensing. *Remote sensing in geology 2* pp. 5-45.

Johnson, J. R., P. R. Christensen, & P. G. Lucey (2002), Dust Coatings on Basaltic Rocks and Implications for Thermal Infrared Spectroscopy of Mars. *Journal of Geophysical Research 107.E6* n. pag.

Kahle, A. B. (1977). A simple thermal model of the Earth's surface for geologic mapping by remote sensing. *Journal of Geophysical Research, 82(11),* pp. 1673-1680.

Kahle, A. B. (1987), Surface emittance, temperature, and thermal inertia derived from Thermal Infrared Multispectral Scanner (TIMS) data for Death Valley, California. *Geophysics 52.7* pp. 858-874.

Kelleher, P. C., and K. L. Cameron (1990). The geochemistry of the Mono Craters-Mono Lake islands volcanic complex, eastern California. *Journal of Geophysical Research 95.B11* pp. 17643-17.

Kieffer, H. H., T. Z. Martin, A. R. Peterfreund, B. M. Jakosky, E. D. Miner, and F. D. Palluconi (1977), Thermal and albedo mapping of Mars during the Viking primary mission. *Journal of Geophysical Research, 82(28)* pp. 4249-4291.

Kent, D. V., S. R. Hemming, and B. D. Turrin (2002), Laschamp excursion at Mono Lake? *Earth Planet. Sci. Lett., 197* pp. 151–164.

Lang, N.P., L. L. Tornabene, H. Y. McSween Jr., & P. R. Christensen (2009). Tharsis-sourced relatively dust-free lavas and their possible relationship to Martian meteorites, *J. Volc. and Geotherm. Res., 185* pp. 103–115.

Lee, R.J., P. L. King, and M. S. Ramsey (2010), Spectral analysis of synthetic quartzofeldspathic glasses using laboratory thermal infrared spectroscopic methods, *J. Geophys. Res., 115, B06202, doi:10.1029/2009JB006672.*

Mackay, G., A. P. Cracknell, & R. A. Vaughan (1991). "Ground heat flux and apparent thermal inertia imagery used to study the regional heat flow pattern and geothermal activity in Iceland." *Proceedings of 5th AVHRR Data Users Meeting held in Tromso, Norway, on*. 1991.

Mars, J. C., and L. C. Rowan (2010), Spectral assessment of new ASTER SWIR surface reflectance data products for spectroscopic mapping of rocks and minerals. *Remote Sensing of Environment 114, no. 9* pp. 2011-2025.

Majumdar, T. J., & B. B. Bhattacharya (1990). Simulation of thermal inertia imagery with daytime HCMM data. *International Journal of Remote Sensing. 11.1* pp. 139-147.

Malin, M. C., and K. S. Edgett (2001), Mars Global Surveyor Mars Orbiter Camera: Interplanetary Cruise through Primary Mission. *Journal of Geophysical Research 106.E10* pp. 23429-3570.

Matsushima, D., R. Kimura, & M. Shinoda (2012), A Study on Soil Moisture Estimation using Thermal Inertia. *Journal of Japan Society of Civil Engineers, Ser. B1 (Hydraulic Engineering)* pp. *67.*

Mellon, M. T., B. M. Jakosky, H. H. Kieffer, & P. R. Christensen (2000), High-resolution thermal inertia mapping from the Mars global surveyor thermal emission spectrometer. *Icarus 148.2* pp. 437-455.

Miller, C. D. (1985), Holocene Eruptions at the Inyo Volcanic Chain, California: Implications for Possible Eruptions in Long Valley Caldera. *Geology 13.1* pp. 14-17.

Mitra, D.S., & T.J. Majumdar Corresponding (2004), Thermal inertia mapping over the Brahmaputra basin, India using NOAA-AVHRR data and its possible geological applications. *International Journal of Remote Sensing 25.16* pp. 3245-3260.

Mouginis-Mark, P.J. (2002), Prodigious ash deposits near the summit of Arsia Mons volcano, Mars, *Geophys. Res. Lett., 29,* 1768, doi:10.1029/2002GL015296.

NASA/GSFC/METI/Japan Space Systems, and U.S./Japan ASTER Science Team. ASTER: Advanced Spaceborne Thermal Emission and Reflection Radiometer.

National Climatic Data Center (NCDC). NOAA, n.d. Web. 24 Mar. 2013.

Nasipuri, P., T. J. Majumdar, and D. S. Mitra (2006), Study of high-resolution thermal inertia over western India oil fields using ASTER data, *Acta Astronaut., 58(5)* pp. 270–278

Ninomiya, Y. (1995), Quantitative estimation of SiO_2 content in igneous rocks using thermal infrared spectra with a neural network approach. *Geoscience and Remote Sensing, IEEE Transactions on 33.3* pp. 684-691.

Ninomiya, Y. (2002), Mapping quartz, carbonate minerals, and mafic-ultramafic rocks using remotely sensed multispectral thermal infrared ASTER data. *AeroSense 2002,* pp. 191-202. *International Society for Optics and Photonics*.

Ninomiya, Y. (2003), Advanced remote lithologic mapping in ophiolite zone with ASTER multispectral thermal infrared data. *Geoscience and Remote Sensing Symposium, IGARSS'03. Proceedings. 2003 IEEE International, vol. 3*, pp. 1561-1563.

Newman, S, S. Epstein, & E. Stolper (1988), Water, carbon dioxide, and hydrogen isotopes in glasses from the ca. 1340 AD eruption of the Mono Craters, California: constraints on degassing phenomena and initial volatile content. *Journal of Volcanology and Geothermal Research 35.1* pp. 75-96.

Palluconi, F. D., & H. H. Kieffer (1981), Thermal inertia mapping of Mars from 60 S to 60 N. *Icarus 45.2* pp. 415-426.

Plescia, J.B. (2004), Morphometric properties of martian volcanoes, *J. Geophys. Res., 109,* E03003, doi:10.1029/2002JE002031.

Pohn, H., T. Offield, & K. Watson (1974), Thermal inertia mapping from satellite-discrimination of geologic units in Oman. *J. Res. US Geol. Surv 2.2* pp. 147-158.

Pratt, D. A., & Ellyett, C. D. (1979). The thermal inertia approach to mapping of soil moisture and geology. *Remote sensing of environment, 8(2),* pp. 151-168.

Price, J. C. (1977) Thermal inertia mapping: A new view of the earth: *J. Geophys. Res., 82*, pp. 2582-2590.

Price, J. C. (1985). On the analysis of thermal infrared imagery: the limited utility of apparent thermal inertia. *Remote sensing of Environment, 18(1),* pp. 59-73.

Price, M. A., M. S. Ramsey, & D. A. Crown (2013), Thermophysical Characteristics of Mantled Terrestrial Volcanic Surfaces: Infrared Analogs to the Arsia Mons Flows. *Lunar Planet. Sci. Conf. #XLIV, abs. #1640.*

Putzig, N. E., M. T. Mellon, K. A. Kretke, and R. E. Arvidson (2005), Global thermal inertia and surface properties of Mars from the MGS mapping mission. *Icarus 173.2* pp. 325-341.

Putzig, N. E., & M. T. Mellon (2007), Apparent thermal inertia and the surface heterogeneity of Mars. *Icarus 191.1* pp. 68-94.

Ramsey, M.S. & D. A. Crown (2010), Thermophysical and spectral variability of Arsia Mons lava flows. *Lunar Planet. Sci. Conf. #XLI, abs. #1111.*

Ramsey, M.S., & D. A. Crown (2011), Thermophysical properties of mantled volcanic surfaces: Can terrestrial analogues be used to better understand Martian volcanism, *Abstract P42C-06, presented at 2011 Fall Meeting, AGU, San Francisco, Calif., 5-9 Dec.*

Ramsey, M. S., D. A. Crown, & M. A. Price (2012), Decoupling Lava Flow Composition and Emplacement Processes from Eolian Mantling Deposits Using Thermal Infrared Data. *Lunar Planet. Sci. Conf. #XLIII, abs. #2013.*

Ramsey, M. S. & J. H. Fink (1996), Estimating lava vesicularity: A new technique using thermal infrared remote sensing data. *Am. Geophys. Union Eos Transactions, 77:46,* pp. F803.

Ramsey, M. S., & J. Fink (1999), Estimating silicic lava vesicularity with thermal remote sensing: A new technique for volcanic mapping and monitoring. *Bulletin of volcanology 61.1* pp. 32-39.

Realmuto, V. J. (1990), Separating the effects of temperature and emissivity: Emissivity spectrum normalization. *In Proc. 2nd TIMS Workshop* pp. 90-55.

Rosema, A., and J. Fiselier (1990), Meteosat-based evapotranspiration and thermal inertia mapping for monitoring transgression in the Lake Chad region and Niger Delta. *International Journal of Remote Sensing 11.5* pp. 741-752.

Rowan, L. C., J. C. Mars, and C. J. Simpson (2005), Lithologic mapping of the Mordor, NT, Australia ultramafic complex by using the Advanced Spaceborne Thermal Emission and Reflection Radiometer (ASTER). *Remote Sensing of Environment 99, no. 1* pp. 105-126.

Rowan, L. C., R. G. Schmidt, and J. C. Mars (2006), Distribution of hydrothermally altered

rocks in the Reko Diq, Pakistan mineralized area based on spectral analysis of ASTER data. *Remote Sensing of Environment 104, no. 1 pp.* 74-87.

Russell, I. C. (1889), Quaternary history of the Mono Valley, California. *U.S. Geological Survey Eighth Annual Rep.* pp. 267-394.

Ruff, S. W., P. R. Christensen, P. W. Barbera, and D. L. Anderson (1997), Quantitative thermal emission spectroscopy of minerals: A laboratory technique for measurement and calibration. *Journal of Geophysical Research 102, no. B7* pp. 14899-14.

Ruff, S W., & P. R. Christensen (2002), Bright and Dark Regions on Mars: Particle Size and Mineralogical Characteristics Based on Thermal Emission Spectrometer Data. *Journal of Geophysical Research 107.E12* n. pag.

Sabins, F. (1987), *Remote Sensing - Principles and Interpretation* (New York: Freeman).

Sabol, D. E., A. R. Gillespie, E. McDonald, and I. Danillina (2006), Differential thermal inertia of geological surfaces. *paper presented at 2nd Annual International Symposium of Recent Advances in Quantitative Remote Sensing, Univ. of Valencia, Torrent, Spain, 25–29 Jul*.

Sampson, D., and K. Cameron (1987), The geochemistry of the Inyo volcanic chain: Multiple magma systems in the Long Valley region, eastern California. *Journal of Geophysical Research 92.B10* pp. 10403-10.

Scheidt, S., M. Ramsey, & N. Lancaster (2010), Determining soil moisture and sediment availability at White Sands Dune Field, New Mexico, from apparent thermal inertia data. *Journal of Geophysical Research: Earth Surface (2003–2012) 115.F2*.

Scheidt, S, N. Lancaster, & M. Ramsey (2011), Eolian dynamics and sediment mixing in the Gran Desierto, Mexico, determined from thermal infrared spectroscopy and remote-sensing data. *Geological Society of America Bulletin 123.7-8* pp. 1628-1644.

Scott, D. (1981), Map showing lava flows in the southeast part of the Phoenicis Lacus quadrangle of Mars. *U.S. Geol. Surv. Misc. Invest. Ser. Map* I-1274.

Scott, D., G. Schaber, & A. Dial (1981a), Map showing lava flows in the southwest part of the Phoenicis Lacus quadrangle of Mars. *U.S. Geol. Surv. Misc. Invest. Ser. Map* I-1275.

Scott, D., G. Schaber, K. Horstman, A. Dial, & K. Tanaka (1981b), Map showing lava flows in the northwest part of the Phoenicis Lacus quadrangle of Mars. *U.S. Geol. Surv. Misc. Invest. Ser. Map* I- 1272.

Scott, D., & J. Zimbelman (1995), Geologic map of Arsia Mons volcano, Mars. U*.S. Geol. Surv. Misc. Invest. Ser. Map* I-2480.

Sheridan, M. (1965), The mineralogy and petrology of the Bishop Tuff. *Ph.D. thesis, Stanford Univ., Palo Alto, Calif.* 165 pp.

Sheridan, M. (1967), Double cooling-unit nature of the Bishop Tuff in Owens River Gorge, California" (abstract): *Geological Society of America Special Paper, v. 115* pp. 351.

Sheridan, M. (1970), Fumarolic mounds and ridges of the Bishop Tuff, California. *Geological Society of America Bulletin, v. 81* pp. 851-868.

Sieh, K. & M. Bursik (1986), Most recent eruption of the Mono Craters, eastern central California. *J. geophys. Res 91.B11* pp. 12-539.

Sieh, K, & M. Bursik (1986), Most Recent Eruption Of The Mono Craters, Eastern Central California. *Journal of Geophysical Research 91.B12* pp. 12539-2571.

Sobrino, J. A., & M. H. El Kharraz (1999a), Combining afternoon and morning NOAA satellites for thermal inertia estimation: 1. Algorithm and its testing with Hydrologic Atmospheric Pilot Experiment-Sahel data. *Journal of Geophysical Research: Atmospheres (1984–2012), 104(D8),* pp. 9445-9453.

Sobrino, J. A., & M. H. El Kharraz (1999b), Combining afternoon and morning NOAA satellites for thermal inertia estimation 2. Methodology and application. *Journal of geophysical research, 104(D8),* pp. 9455-9465.

Tonooka, H., F. Sakuma, M. Kudoh, & K. Iwafune (2004), ASTER/TIR Onboard Calibration Status and User-Based Recalibration. *Remote Sensing* pp. 191-201.

Van de Griend, A., P. Camillo, and R. Gurney (1985), Discrimination of soil physical parameters, thermal inertia, and soil moisture from diurnal surface temperature fluctuations. *Water Resources Research 21.7* pp. 997-1009.

Vaughan, R. A. (1987), Surface Energy Budget, Surface Temperature, and Thermal Inertia. *Remote Sensing Applications in Meteorology and Climatology*. Dordrecht: D. Reidel Pub., pp. 404.

Vickers, R. & R. J. P. Lyon (1967) Infrared sensing from spacecraft—A geologic interpretation. *Proc. Thermophysics Special Conf., Amer. Inst. Astron.* pp. 67-284.

Wallace, P., A. Anderson Jr., A. Davis (1999) Gradients in H_2O, CO_2, and exsolved gas in a large-volume silicic magma system: interpreting the record preserved in melt inclusions from the Bishop Tuff" *J. Geophys. Res. 104 (B9)* pp. 20097–20122

Watanabe, H., and K. Matsuo (2003), Rock type classification by multi-band TIR of ASTER. *Geosciences Journal 7, no. 4* pp. 347-358.

Watson, K. (1973), Periodic Heating of a Layer over a Semi-Infinite Solid. *Journal of Geophysical research 78.26* pp. 5904-5910.

Watson, K. (1975), Geologic Applications of Thermal Infrared Images. *Proceedings of the IEEE 63.1* pp.128-137.

Weather Underground, Weather History – July 10, 2011, Mammoth, CA. Accessed 2013. http://www.wunderground.com/history/airport/KMMH/2011/7/10/DailyHistory.html?req_city=Lee+Vining&req_state=CA&req_statename=California

Wilson, C., W. Hildreth (1997), The Bishop Tuff: New Insights from Eruptive Stratigraphy. *J. Geol. 105* pp. 407–439

Wood, S. (1977), Chronology of late Pleistocene and Holocene Volcanics, Long Valley and Mono Basin Geothermal Areas, Eastern California. *US Geol. Surv. Final Tech. Rept., Geothermal Research Program*, [reprinted as *US Geol. Surv. Open-File Rept.* (1983) pp. 83-747]

Wood, S. (1989), Chronology of late Pleistocene and Holocene volcanics, Long Valley and Mono Basin geothermal areas, eastern California. *U.S. Geol. Survey Open File Report 83* pp. 747, 76

Xue, Y. & A. Cracknell (1995), Advanced Thermal Inertia Modelling. *Remote Sensing 16.3* pp. 431-446.

Yamaguchi, Y., A. Kahle, H. Tsu, T. Kawakami, and M. Pniel (1998), Overview of Advanced Spaceborne Thermal Emission and Reflectance Radiometer (ASTER). *IEEE Trans. Geosci. Remote Sens. 36,* pp. 1062-1071.